DOI:10.14753/SE.2018.2077

Distinct behavior and synaptic properties of perisomatic and dendritic-region targeting interneurons during physiological and pathological network states in the CA3 region of the mouse hippocampus *in vitro*

Ph.D. Dissertation

Zsolt Kohus

Semmelweis University

János Szentágothai Doctoral School of Neuroscience

Supervisor: Attila I Gulyás, Ph.D

Official Reviewers: Lucia Wittner, Ph.D
Zoltán Somogyvári, Ph.D

Head of the Final Examination Committee: Pál Czobor, MD, Ph.D
Members of the Final Examination Committee: Tibor Zelles, MD, Ph.D
György Karmos, MD, Ph.D

Budapest

2017

DOI:10.14753/SE.2018.2077

I. TABLE OF CONTENTS

DOI:10.14753/SE.2018.2077

DOI:10.14753/SE.2018.2077

DOI:10.14753/SE.2018.2077

II. LIST OF ABBREVIATIONS

4-AP: 4-aminopyridine

AAC: axo-axonic cell

ACSF: artificial cerebrospinal fluid

AIS: axon initial segment

AM251: N-(Piperidin-1-yl)-5-(4-iodophenyl)-1-(2,4-dichlorophenyl)-4-methyl-1H-pyrazole-3-carboxamide

AMPA: α-amino-3-hydroxy-5-methylisoxazole-4-propionic acid

AP: action potential

BC: basket cell

CA1-CA3: Cornu Ammonis fields

Ca_{local}: local calcium concentration

Ca_{res}: residual calcium

CB1R: cannabinoid receptor type I

CCK: cholecystokinin

CCK+ BC: cholecystokinin positive basket cell

CCK+ DTI: cholecystokinin positive dendritic region-targeting interneuron

CCK+: cholecystokinin positive

DG: dentate gyrus

DsRED: red fluorescent protein

DTI: dendritic region-targeting interneuron

EC: entorhinal cortex

EE: epileptiform event

EEG: electro-encephalogram

eGFP: enhanced green fluorescent protein

EPI: epilepsy protocol, 30 action potentials at 160 Hz followed by 4 action potentials at 320 Hz

EPSC: excitatory postsynaptic current

GABA: γ-aminobutyric acid

HFO: high frequency oscillation

IIE: interictal-like event

IN: interneuron

IPSC: inhibitory postsynaptic current

IS: interneuron-selective interneuron

KW: Kruskal-Wallis ANOVA

LFP: local field potential

mACSF: modified artificial cerebrospinal fluid

MS: medial septum

MW: Bonferroni-corrected Mann-Whitney U test

NBQX: 2,3-dihydroxy-6-nitro-7-sulfamoyl-benzo[f]quinoxaline-2,3-dione; an AMPA receptor antagonist

NMDA: N-methyl-D-aspartate

PC: pyramidal cell

PTI: perisomatic region-targeting interneuron

PV: parvalbumin

PV+ BC: parvalbumin positive basket cell

PV+: parvalbumin positive

PVeGFP mice: transgenic mice expressing enhanced green fluorescent protein controlled by PV promoter

RIP: ripple protocol, 4 action potentials at 160 Hz

STD: short-term depression

STF: short-term facilitation

SWR: sharp wave-ripple

uIPSC: unitary inhibitory postsynaptic current

DOI:10.14753/SE.2018.2077

III. INTRODUCTION

The hippocampal formation is one of the most studied neuronal system in the brain and appears to be crucial for many high order cognitive functions, such as encoding and retrieval of memory and spatial navigation (Buzsáki, 1986; O'Keefe and Recce, 1993). The hippocampus and related structures show rhythmic oscillatory activities in various frequency ranges in a behavior-dependent manner (Buzsáki and Draguhn, 2004; Singer, 1999), which activity patterns strongly correlate with different cognitive functions. In freely moving rodents, three types of hippocampal oscillations have been observed: theta (5-10 Hz) and embedded gamma rhythms (30-100 Hz) are observed during exploration and rapid eye movement sleep (Bragin et al., 1995; Buzsáki, 1989; Colgin, 2013; Colgin et al., 2009; Csicsvari et al., 2003; Hasselmo et al., 1996). In addition, sharp-wave associated ripples (100-300 Hz) appear during awake immobility, consummatory behavior and slow-wave sleep (Csicsvari et al., 2000; Ylinen et al., 1995).

The alternation of these behavior-associated hippocampal activity patterns is an inherent and general property of the healthy hippocampal network and plays a critical role in information processing and memory consolidation (Girardeau et al., 2009; Jadhav et al., 2012). A key requirement for the generation of network oscillations is the regular and synchronized network activity: the regular and synchronous firing of several neurons generates a rhythmic activation of output synapses providing a periodic fluctuation in the membrane potential of postsynaptic target cells, resulting in a fluctuating field potential signal. All of these network activities require a temporally precise and effective inhibition to control the discharge of pyramidal cells (Aradi et al., 2002; Buzsáki and Draguhn, 2004; Földy et al., 2004; Somogyi and Klausberger, 2005). Several lines of studies show that perisomatic region-targeting interneurons have a crucial role in generating physiological oscillatory activities in the cortical network by providing effective and precisely timed inhibition of large cell assemblies (Gulyás et al., 2010; Schlingloff et al., 2014). However, changes in the balance between excitation and inhibition towards excitation can result in a network hyperexcitability and recurrent pathological seizures – epileptiform events (Florence et al., 2009). Therefore, it is essential to understand the role of individual neurons in the generation of physiological and pathological activity patterns,

and to identify the mechanisms leading to transition from physiological to pathological network states.

One way to get closer to understand the genesis of these complex activity patterns is the measurement of relevant network, cellular and synaptic parameters. Hippocampal slices have been proven as a powerful experimental model for investigating the functional properties of hippocampal oscillations and underlying mechanisms. In an improved slice holding chamber, thick (450 μm) hippocampal slices were shown to produce *in vivo*-like activity levels and patterns including spontaneous sharp wave-ripples and pharmacologically induced gamma oscillation (Hájos and Paulsen, 2009; Hájos et al., 2009). Moreover, they allow rapid pharmacological interventions, optogenetic manipulation, local drug application, and the parallel measurement of network and cellular activity during spontaneous and triggered network oscillations, as well as the interactions among neuronal elements of the circuit (Szabó *et al.*, 2010; Gulyás *et al.*, 2010; Hájos *et al.*, 2013; Schlingloff *et al.*, 2014;).

First we address the questions how the same network can generate physiological and pathological high activity levels and what is the contribution of principal cells and different types of interneurons to the generation of interictal like-events. To answer these questions we induced transition from *in vitro* sharp wave-ripples to interictal like-events, and analyzed the network, cellular and synaptic parameters leading to the reorganization of synchrony and firing patterns.

The functional connectivity between neurons can give rise to oscillations at different frequencies (Schnitzler and Gross, 2005). To understand the connection trends and interaction among CA3 interneurons, we performed paired recordings between perisomatic and dendritic region-targeting interneurons and their interneuron and pyramidal cell targets, and physiologically and pathologically relevant action potential trains were used to stimulate presynaptic cells. We also fitted dynamic models of synaptic transmission to the data to provide formalized description of inhibitory transmission among cells. Finally, we show how inhibitory dynamics between PV+ basket cells and pyramidal cells could contribute to sharp wave-ripple generation.

Earlier *in vitro* studies investigating the transmission parameters between interneurons and their target cells were carried out in ‘classical’ artificial cerebrospinal fluid (ACSF) producing reduced neuronal activity in slices (Gulyás et al., 2010; Szabó et

al., 2010). Because the activity level in a network can tune the excitability and transmission parameters (Reig and Sanchez-Vives, 2007), in order to mimic *in vivo* environment, we used thicker hippocampal slices (350-450 μm), and during experiments the 'classical' ACSF was switched to modified '*in-vivo* like' ACSF, that resulted in high, *in vivo*-like activity patterns.

III.1. The hippocamus

The hippocampal formation, including the dentate gyrus (DG), the hippocampus proper (consisting of the Cornu Ammonis (CA) fields CA1-C3) and the subiculum, is a double C-shaped structure located in the temporal lobe of the brain (Figure 1). The hippocampus and DG are also referred as archicortex composed only of three layers (in contrast to the neocortex which is generally thought to comprise of five or six layers), and has a direct connection to the parahippocampal formation consisting of presubiculum, the parasubiculum, the medial (MEA) and lateral (LEA) entorhinal cortical areas and the perirhinal cortex.

The first layer of the hippocamus is the polymorph deep layer, called stratum oriens. Superficial to the deep layer lies the CA1-CA3 principal cell layer. The most superficial layer is the the stratum lucidum (CA3), stratum radiatum and stratum lacunosum moleculare (van Strien et al., 2009).

Although there are substantial differences in the cytoarchitecture and connectivity patterns of the hippocampus between different species, the layout of cells as well as afferent and efferent fibers are phylogenetically conserved and are similar in humans and rodents. Since experiments described in this thesis were carried out in mice, the chapters describing the hippocampus (cytoarchitecture, its connectivity, activity patterns, short-term plasticity) are limited to the rodent hippocampus.

III.1.1. The cytoarchitecture of the hippocampus

To understand how the hippocampus maintains its function, a detailed knowledge of the structure-function relationship of microcircuits and individual cell types is required. Hippocampal neurons can be divided into two main categories based on their main

neurotransmitter. The majority of the neurons (~ 85%) are glutamatergic excitatory principal cells (pyramidal cells). On the other hand, the diverse minority of hippocampal cells (~ 15%) are formed by GABAergic cells (releasing inhibitory γ-aminobutyric acid, GABA). They represent a highly heterogeneous cell population with cell bodies scattered through all layers (Freund and Buzsáki, 1996; Somogyi and Klausberger, 2005).

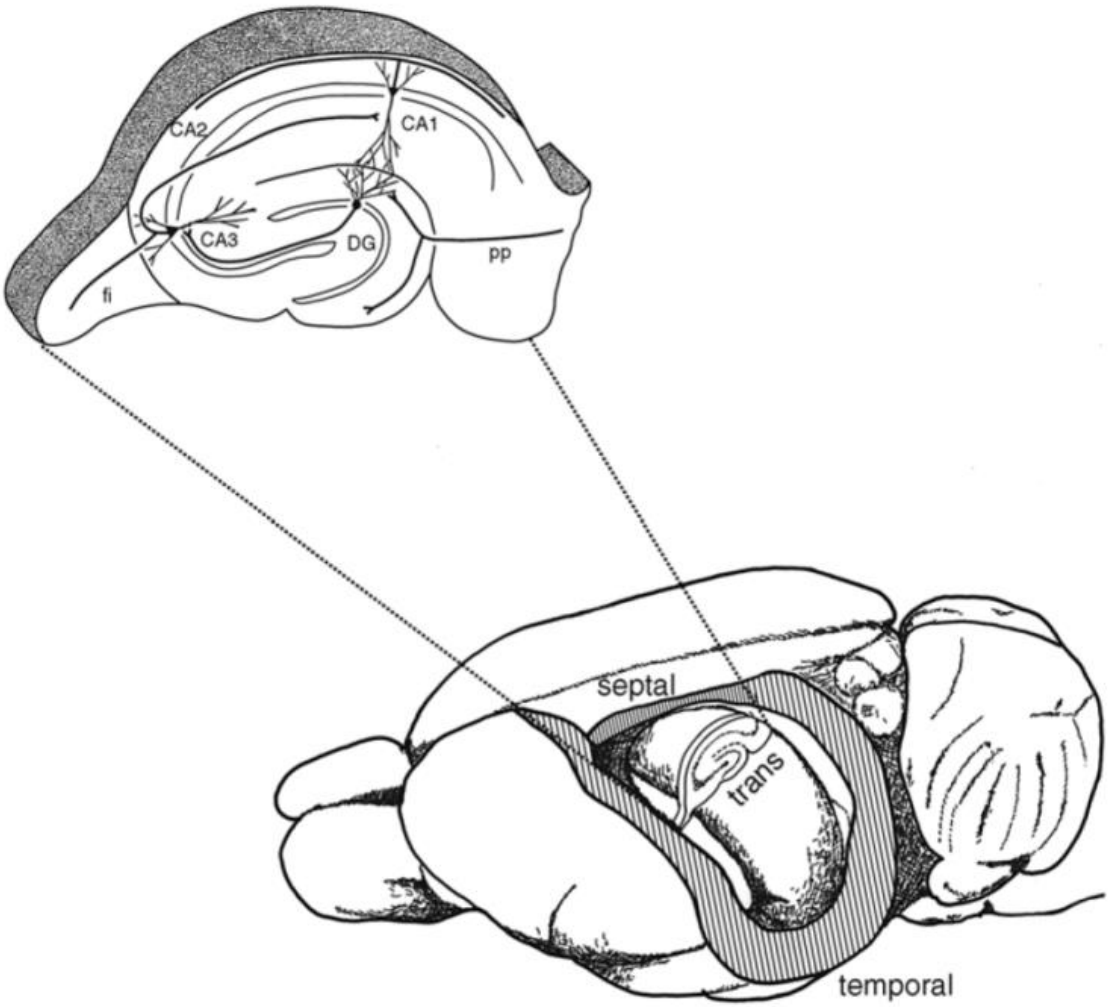

Figure 1. The anatomy of the hippocampus. *The drawing depicts a rat brain after the neocortex overlaying the hippocampus was removed, revealing the position and the shape of hippocampus.; TRANS: transverse axis, orthogonal to the septotemporal axis. The inset shows an enlarged section along the transverse axis, with the trisynaptic circuit. CA1, CA2, CA3: cornu ammonis 1, 2, 3 region of the hippocampus; DG: dentate gyrus; PP: perforant path. Adapted from Andersen et al., 2007*

DOI:10.14753/SE.2018.2077

III.I.2. Principal cells

The principal cells of the CA field are the pyramidal cells located in the stratum pyramidale (or pyramidal cell layer). However, the CA has a heterogeneous structure due to different features of pyramidal cells. Thus, the CA has been described by Lorente de Nó as having three subfields named CA1, CA2 and CA3.

The CA3 region lies proximal to the DG and is subdivided into CA3c, CA3b and CA3a (from the hilus towards the CA1). CA3 pyramidal cells have relatively large cell body (20-30 μm of soma diameter, with two to four time larger surface than CA1 pyramidal cells). The dendritic tree has two distinct domains: the basal dendrites arise from the base of the soma and extend into stratum oriens towards the alveus, whilst apical dendrites descend from the apex of the soma and traverse three strata: the stratum lucidum, the stratum radiatum and the stratum lacunosum moleculare (Spruston, 2008). The dendrites of CA3 pyramidal cells are densely covered by dendritic spines, serving as postsynaptic targets primarily for glutamatergic terminals. In addition to dendritic spines, CA3 pyramidal cells also have large complex spines called thorny excrescences, which are the synaptic target of mossy fiber boutons. The thorny excrescences are mainly concentrated on the proximal part of the apical dendrites in stratum lucidum (Gonzales et al., 2001). The CA2 and CA1 regions of CA does not receive mossy fiber inputs, therefore they lack the stratum lucidum and CA2 and CA1 pyramidal cells are devoid of thorny excrescences (Dudek et al., 2016; Ishizuka et al., 1995).

CA3 pyramidal cell axons project ispi- and contralateraly to all CA subfields and to the lateral septal nuclei (Ishizuka et al., 1990; Li et al., 1994). They give rise to the Schaffer collateral inputs to CA1 pyramidal neurons, and they form an extensive associational connection between CA3 pyramidal neurons (called recurrent collateral system). Their postsynaptic targets include both pyramidal cells and interneurons (Gulyás et al., 1993a; Li et al., 1994; Miles, 1990; Sik et al., 1993).

The CA2 subfield is a narrow zone positioned between CA3 and CA1. CA2 pyramidal cells have similar morphology to those in CA3, however, they have larger cell bodies than those in CA3, and do not receive inputs from the DG (they lack thorny excrescences). Axons of CA2 pyramidal cells, similar to CA3 pyramidal cells, project to the ipsi- ad contralateral CA1-CA3 areas and contribute to the commissural/associational

system (Li et al., 1994; Mercer et al., 2007). CA2 pyramidal cells have also been reported to project back to the medial entorhinal cortex (Hitti and Siegelbaum, 2014; Kohara et al., 2014).

CA1 pyramidal cells tend to be smaller than in CA3. The cell bodies have a diameter of ~15 μm, located in the CA1 stratum pyramidale, however, CA1 pyramidal cells have also been found in the stratum radiatum (Cajal, 1968, Gulyas, 1998) and stratum oriens (Bannister and Larkman, 1995a). CA1 pyramidal cells are not homogeneous but can be grouped by molecular (Baimbridge et al., 1991), morphological (Slomianka et al., 2011) and functional properties (Valero et al., 2015). Another source of variability of CA1 pyramidal cells is the position or depth relative to the cell layer (Bannister and Larkman, 1995a). Early studies have demonstrated segregation of calbindin immunoreactivity in the deep and superficial substrata of CA1 (Baimbridge et al., 1991). It has been also shown, that PV+ basket cells differentiate among deep and superficial CA1 pyramidal cells and provide distinct perisomatic inhibitory interactions (Lee et al., 2014), and they show different intracellular dynamics during sharp wave-ripples (Valero et al., 2015).

The basal dendrites (two to eight) of CA1 pyramidal cells emerge from the soma in the sratum oriens, and the apical dendrites extend into the stratum radiatum and form a dendritic tuft in stratum lacunosum-moleculare (Megías et al., 2001). The dendrites of CA1 pyramidal cells are densely covered with dendritic spines, however, proximal basal dendrites are sparsely spinous (Bannister and Larkman, 1995b; Megías et al., 2001).

CA1 pyramidal cells represent the main output of the hippocampal formation. The local axon collaterals of CA1 pyramidal cells provide a major excitatory input to interneurons, and form synapses onto neighboring CA1 pyramidal cells. However, the recurrent connectivity in the CA1 area is very low (Deuchars and Thomson, 1996). On the other hand, CA1 pyramidal cells heavily project to the subiculum and the deeper layers of entorhinal cortex (Amaral and Witter, 1989). They also send long projections to other brain areas including amygdala, hypothalamus, prefrontal cortex, nucleus accumbens, olfactory regions, auditory cortex, visual cortex, as well as to the lateral septal nucleus and the diagonal band of Broca (Cenquizca and Swanson, 2007).

Within the hippocampal formation, the flow of information is mostly unidirectional, and the special chain of excitatory synaptic connections is also known as the classical trisynaptic hippocampal circuitry (Figure 2). The trisynaptic circuit or trisynaptic loop is

DOI:10.14753/SE.2018.2077

a relay of synaptic transmission in the hippocampus, and was initially described by Santiago Ramon y Cajal.

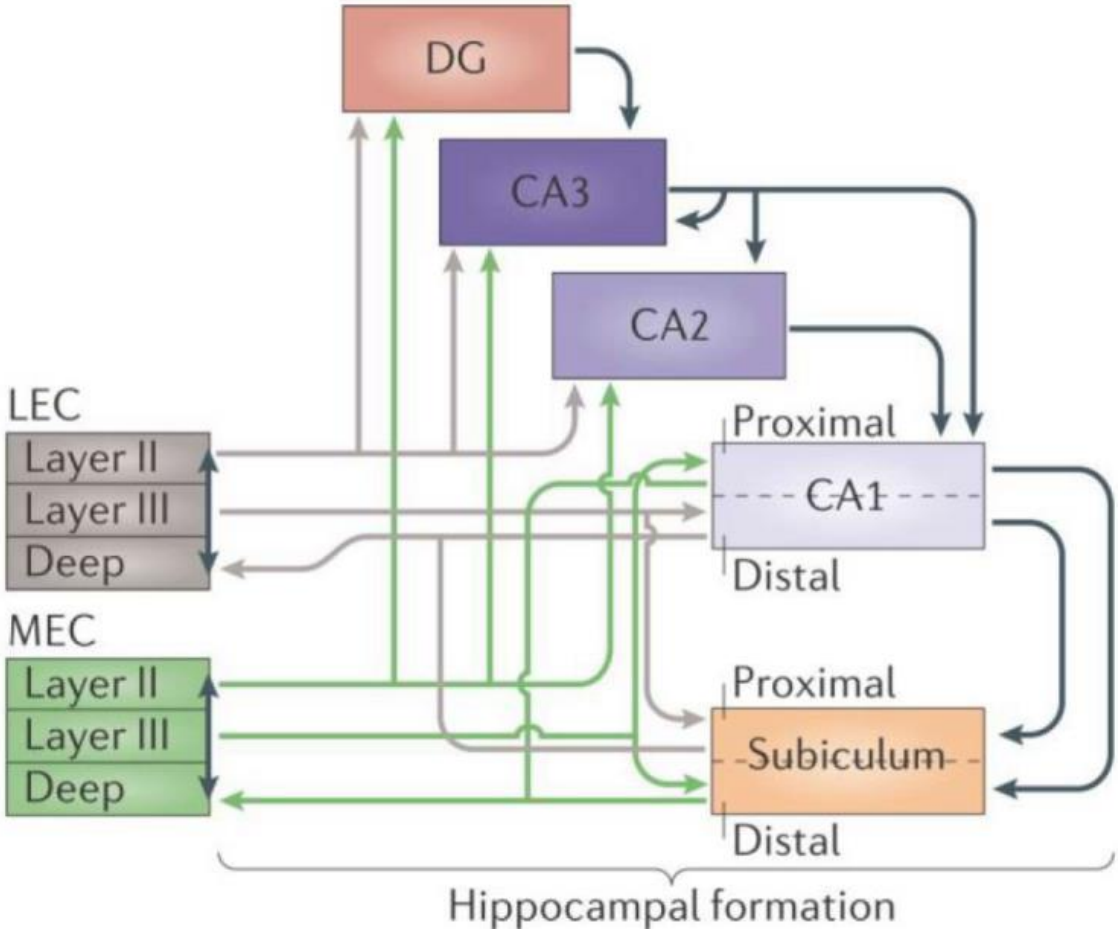

Figure 2. The information flow through the hippocampus. *The major cortical input to the hippocampus and the dentate gyrus is the entorhinal cortex (EC) through the perforant path, arising mainly from layers II and III. Medial entorhinal cortex (MEC) layer II provides input to the dentate gyrus (DG), CA3 and CA2, and layer III project to CA1 and subiculum. CA1 and subiculum give rise to output to EC layer V. This connection route (green lines) is paralleled by the route starting in the lateral entorhinal cortex (LEC, gray lines). LEC layer II projects to the outer third of molecular layer of the DG and the outer half of the stratum lacunosum moleculare of CA3, whereas layer II cells of MEC establish connections with the middle third of the molecular layer of DG and inner half of the stratum lacunosum moleculare of CA3. LEC layer III form synapses with CA1 pyramidal cells on the most distal portion of apical dendrites in stratum lacunosum moleculare. The two pathways converge onto single neurons in the DG, CA3 and CA2, but target different neurons in CA1 and subiculum. The axons of granule cells in the DG give rise to mossy fibers and form synapses with CA3 neurons. In turn, CA3 pyramidal cells project to CA1 via Schaffer collaterals and form synapses on the apical and basal dendrites of CA1 pyramidal cells. Note tha the DG and layer II of MEC and LEC also project to CA2, which in turn connects to CA1 pyramidal cells. This suggests that CA2 is also involved in the trisynaptic circuitry). Adapted from Moser et al., 2014.*

The major input is carried by axons of the perforant path (1st synapse), which convey polymodal sensory information from the neurons of the entorhinal cortex (EC) (layer II). Axons of the medial and lateral EC form excitatory synapses with the outer and middle third of dendrites of granule cells in DG (in stratum moleculare). The layer III of EC also project topographically to the CA1; the lateral EC project to the distal part of CA1, bordering subiculum, while medial EC give rise to fibers terminating in the proximal part of CA1 (bordering CA2). The axons of the granule cells in DG (also known as mossy fibers) innervate the complex spines (thorny excrescences) of proximal and apical dendrites of CA3 pyramidal cells (2nd synapse). The CA3 pyramidal cells, in turn, project to ipsilateral CA1 pyramidal cells through Schaffer collaterals (3rd synapse), and contralateral to CA3 and CA1 pyramidal cell through commissural connections. The CA3 pyramidal cells have an extensive network of recurrent collaterals forming excitatory connections with other pyramidal cells in strata oriens and radiatum. The axons of CA3 pyramidal cells (called Schaffer collaterals) are organized in a three-dimensional, topoghraphic manner. CA3 pyramidal cells located in CA3c region are more likely to innervate CA1 pyramidal cells near the subiculum, whilst CA3 pyramidal cells near the CA2 border (CA3a) are more likely to connect proximal CA1 pyramidal cells, located closer to the CA2 border (Andersen et al., 1971). However, it has recently been shown, that mossy fibers enter the CA2 region and innervate by small boutons the shaft and simple spines of CA2 pyramidal cells. Moreover, the layer II (but not layer III) medial and lateral EC also project to the CA2 region. This suggests an existence of an alternative trisynaptic circuit: DG-CA2-CA1 (Kohara et al., 2014) (Figure 2).

DOI:10.14753/SE.2018.2077

III.1.3. Interneurons of the CA3 region

Whereas the majority of principal cells of the hippocampus proper have their cell bodies organized into the pyramidal cell layer, the cell bodies of GABAergic inhibitory cells (interneurons) are scattered throughout all layers. Interneurons represent only ~15% of the total hippocampal neuronal population, but they show extreme heterogeneity with respect to their morphological and physiological characteristics, as well as with their expression of neurochemical markers and transcription factor (Somogyi and Klausberger, 2005). As the experiments in our studies were performed in the CA3, in this part I will focus on interneurons described within this region.

As the most distinct anatomical feature of interneurons is the layer-specific distribution of their axons and dendrites, the majority of classification schemes have considered mainly their dendritic and axonal arborization. The localization of dendrites provides information about the inputs, while the axonal tree determines the output of interneurons, and predicts their potential role in neuronal networks.

Based on their axonal arborization hippocampal inhibitory cells can be classified into four major groups (Klausberger and Somogyi, 2008):

1. ***perisomatic region-targeting interneurons***, innervating the perisomatic region of pyramidal cells
2. ***dendritic region-targeting interneurons***, innervating the dendritic region of pyramidal cells
3. ***interneuron-selective interneurons*** targeting predominantly, if not exclusively other interneurons
4. ***long-range projecting GABAergic cells***, sending long-range projections to other brain areas.

III.1.3.1. Perisomatic region-targeting interneurons

The perisomatic region of pyramidal cells is a defined domain of plasma membrane, including the soma, the axon initial segment, and the proximal and basal dendrites up to 100 μm (Freund and Katona, 2007; Megías et al., 2001). This region is targeted by three types of perisomatic region-targeting interneurons: the parvalbumin positive (PV+) axo-axonic cells (AACs), PV+ basket cells (PV+ BCs) and the cholecystokinin expressing

(CCK+) basket cells (CCK+ BCs) (Figure 3). All three types of interneurons often have their soma close to the pyramidal cell layer, but some CCK+ BCs can be found in st. oriens and str.radiatum . The location of output synapses of perisomatic region-targeting interneurons is well suited to influence the timing and synchronization of action potential firing in a large population of principal cells (Cobb et al., 1995; Freund and Katona, 2007).

Axo-axonic cells are known to innervate almost exclusively the axon initial segment (AIS) of pyramidal cells (Freund and Buzsáki, 1996). Their axonal tree terminates mainly in the pyramidal cell layer, and form radial rows of boutons around the str. pyramidale – str.oriens border. Their radial dendritic tree spans all hippocampal layer with a prominent tuft in str. lacunosum moleculare (Viney et al., 2013). They show fast spiking phenotype (Szabó et al., 2010), and through $GABA_A$ receptor-mediated inhibition on the AIS can effectively control the action potential generation of pyramidal cells (Buhl et al., 1994).

The basket cells are named after their axons forming a perisomatic basket around the cell bodies and proximal dendrites of pyramidal cells. They have dense axon collaterals in the principal cell layer, and based on their neurochemical content can be classified as PV+ BCs and CCK+BCs (Freund and Buzsáki, 1996).

Besides anatomical similarities the input and out properties of the two basket cell types are highly dissimilar (Glickfeld and Scanziani, 2006). PV+BCs have fast spiking character and respond reliably to repetitive excitation with short and precisely timed action potentials. Thus, PV+BCs act as rapid signaling interneurons translating precisely the rapid excitatory inputs into fast and short-latency inhibitory outputs (Jonas et al., 2004). In contrast, CCK+BCs show regular spiking phenotype, require extensive integration of excitatory inputs to generate spike trains, and respond less readily to excitatory signals (Glickfeld and Scanziani, 2006). Differences have also been shown at axon terminals of the two basket cell types: P/Q type calcium channels located presynaptically on PV+BC terminals are tightly coupled to vesicle fusion, providing quick, highly synchronized GABA release with low failure rate. In contrast, CCK+ cells express N-type calcium channels located more remotely from the release site. The GABA release from CCK+BC terminals shows strong fluctuation in latency and amplitude, as well as higher failure rate, resulting in weak inhibition with low temporal precision (Hefft

and Jonas, 2005). In addition, PV+ BCs and CCK+ BCs are sensitive to different neuromodulators. For example, PV+ BCs express μ opioid receptors that can reduce inhibitory transmission (Gulyás et al., 2010). On the other hand, cannabinoid receptor type 1 (CB_1R), are present on presynaptic terminals of CCK+ BCs but not PV+ BCs (Földy et al., 2006; Szabó et al., 2014), and can mediate suppression of GABA release from CCK+ terminals (Földy et al., 2006).

A special type of GABAergic cells in the CA3 region is the mossy-fiber associated (MFA) interneuron. MFA interneurons have extensive axonal arbors in the str. lucidum, co-alignated with the mossy fibers, and often give rise to additional axon collaterals in the hilus. Their dendrites are located in the str.radiatum and oriens. Their axons are terminated on the proximal apical dendritic shafts, and to a lesser degree on the somata of principal cells (Szabó et al., 2014; Vida and Frotscher, 2000). MFA interneurons, similar to CCK+ BCs, are sensitive to CB_1R activation (Losonczy et al., 2004; Szabó et al., 2014)

III.1.3.2. Dendritic region-targeting interneurons

The inhibition provided by perisomatic region-targeting interneurons plays a crucial role in the control of action potential discharges. However, the majority of inhibitory inputs are located in the dendritic region, where they often match the spatial distribution of the afferent excitatory pathways (Klausberger, 2009). The layer-specific distribution of dendritic region-targeting interneurons provides spatially defined inhibition and controls the local dendritic electrogenesis of principal cells (Miles et al., 1996a).

The peculiar anatomical arrangement of *oriens lacunosum-moleculare* (O-LM) cells suggests their unique functional role in the hippocampal network. The cell body and horizontal dendrites bearing elongated filopodia-like spines are found in str. oriens, while their axons project to the str. lacunosum moleculare, where they extensively branch (Hájos et al., 2013) (Figure 3). O-LM cells are positioned to provide inhibition to the excitatory input arriving at the distal dendrites of CA3 pyramidal cells via excitatory entorhinal perforant path afferents (Hájos and Mody, 1997).

The cell bodies of *perforant path-associated cells* are located in the str. radiatum or str. lacunosum moleculare, often at the border of these two layers (Figure 3). Similar to CCK+ basket cells they express CB_1R on their axon terminals (Szabó et al., 2014). Their

dendrites can reach all layers or remain in the str. lacunosum moleculare and adjacent str. radiatum. Their axons terminate in the str. lacunosum moleculare and overlap with the excitatory input from the entorhinal cortex, the perforant path (Hájos and Mody, 1997; Pawelzik et al., 2002; Vida et al., 1998), where they innervate the apical tuft of pyramidal cells (Klausberger et al., 2005). However, Szabó et al. (2014) found examples of perforant path-associated cells where axon collaterals left str. lacunosum moleculare and formed a meshwork in the str. radiatum close to the border of str. lacunosum moleculare.

Stratum radiatum (R-interneurons) (Figure 3) and *stratum lacunosum-moleculare interneurons (LM-interneurons)* in the CA3 region were first described by Gulyás et al. (1993b). The somata of R- and LM-interneurons are positioned approximately 147 and 257 μm from the boundary between str.pyramidale and lucidum, respectively, and approximately 100 μm from the medial extent of the suprapyramidal blade of the DG (Calixto et al., 2008). They are characterized by one to six typically aspiny dendritic tree stemming from the soma, and give rise to elaborated axonal arbors, which often extend beyond their layer of somatic residence: into the str. radiatum (for LM-interneurons) and str. lacunosum-moleculare (for R-interneurons) (Ascoli et al., 2009). It has been shown that R- and LM-interneurons possess voltage-dependent conductances playing role in shaping the temporal integration of converging excitation. Moreover, they can act as a coincident detector for subtreshold input from the perforant path and mossy fibers (Calixto et al., 2008)

Oriens-oriens and *oriens-radiatum cell* somas are located in str.oriens (Figure 3). Oriens-oriens cells have smooth dendrites and axons restricted to str.oriens. On the other hand, the rarely ramifying axons of CA3 oriens-radiatum cells could be observed in strata oriens and radiatum, and occasionally penetrating into the CA1 region (Hájos et al., 2013)

DOI:10.14753/SE.2018.2077

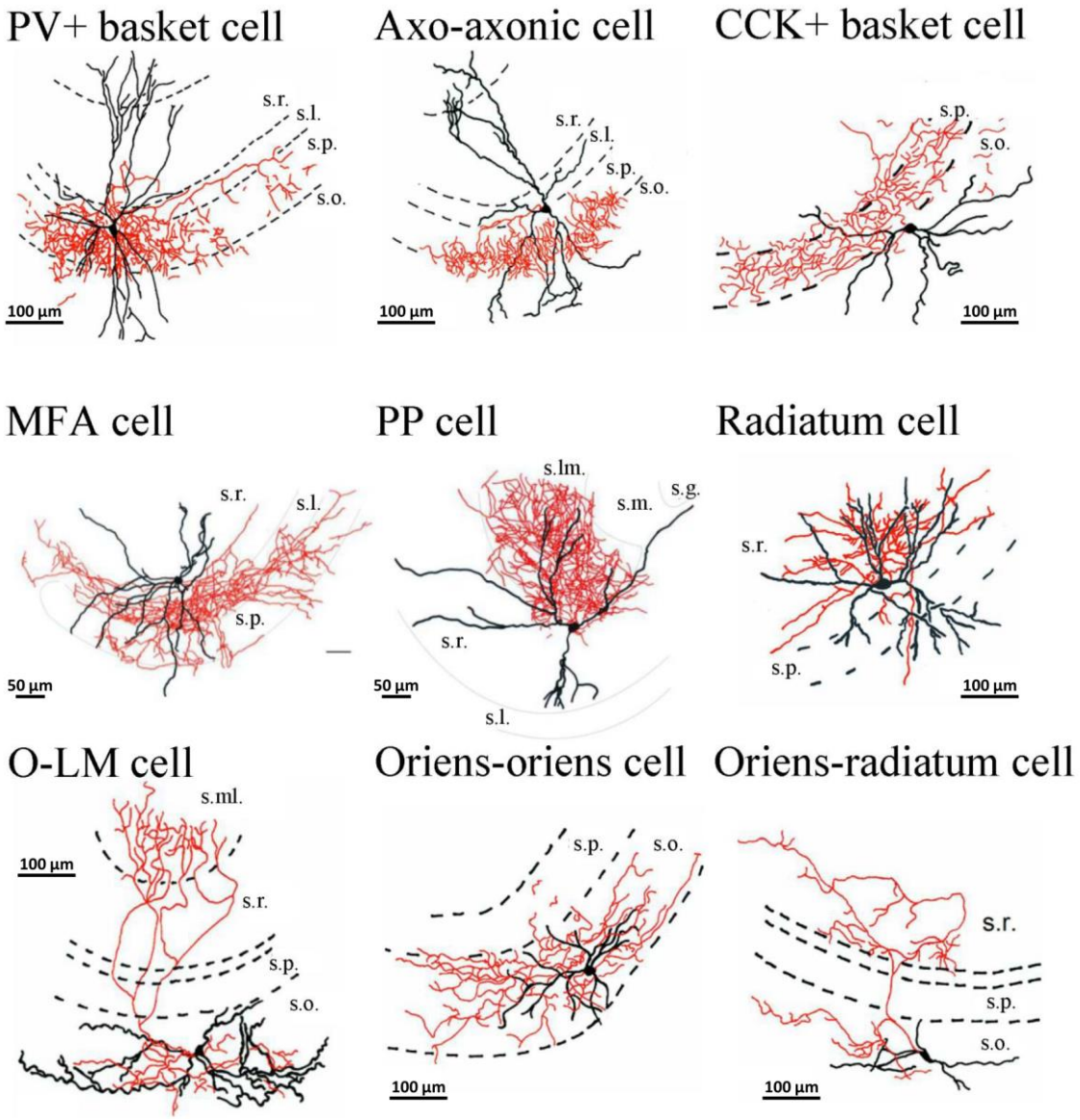

Figure 3. Camera lucida reconstruction of intracellularly labeled CA3 perisomatic and dendritic region-targeting interneurons. *In the camera lucida reconstruction, the cell bodies and dendrites are shown in black, while the axon collaterals in red. Note that the majority of axon arbor of perisomatic region-targeting interneurons (PV+ basket cell, axo-axonic cell, CCK+ basket cell) and MFA cell, PP cell, radiatum cell, oriens-oriens cell (dendritic region-targeting interneurons) can be restricted to a given layer. In case of O-LM and oriens-radiatum cells (dendritic-region targeting interneurons) axons could cover a substantially wider range, often penetrating into neighboring strata. s.r., stratum radiatum; s.l., stratum lucidum; s.p., stratum pyramidale, s.o., stratum oriens; s.ml., stratum moleculare; s.lm., stratum lacunosum moleculare, s.g., stratum granulosm; MFA cell, mossy fiber-associated cell; PP cell, perforant path-associated cell; O-LM cell, oriens-lacunosum moleculare cell. Adopted from Hájos et al., (2013) (PV+ basket cell, axo-axonic cell, CCK+ basket cell, O-LM cell, radiatum cell, oriens-oriens cell, oriens-radiatum cell) and Szabó et al. (2014) (MFA cell, PP cell), with permission.*

Neurogliaform cells are probably the most compact interneurons in the stratum lacunosum moleculare (Capogna, 2011). The soma and dendrites are located within the same layer (Price et al., 2005), with dense axonal arbor in the str. lacunosum molecular and the border of str. lacunosum moleculare and str. radiatum. As far as we know, neurogliaform cells has been described only in the CA1 and DG within the hippocampus (Armstrong et al., 2011; Capogna, 2011; Vida et al., 1998). However, it does not necessarily mean that neurogliaform cells are not present in the CA3 str.lacunosum-moleculare. *Ivy cells* are closely related to neurogliaform cells, but their soma is located in the strata pyramidale or radiatum. They have dense and fine local axonal plexus innervating predominantly the basal and oblique dendrites of pyramidal cells. Ivy cells and neurogliaform cells express neuropeptide Y and often express neuronal nitric oxide synthase (nNOS) (Fuentealba et al., 2008; Price et al., 2005). They represent the most abundant interneuron class in the hippocampus, comprising 37% of GABAergic cells (Capogna, 2011; Fuentealba et al., 2008).

III.1.3.3. Interneuron-selective interneuron

Interneurons belonging to the same class are often connected by GABAergic synapses and tend to form reciprocally connected networks (Chamberland and Topolnik, 2012). In addition, GABAergic cells receive synapses from a population of inhibitory cells, which specifically innervate other interneurons, the so-called *interneuron-selective (IS) interneurons*. Gulyás et al. (1996) distinguished two types of calretinin-expressing IS interneurons in the CA3 subfield based on the dendritic morphology and somatic distribution. The cell body and the entire dendritic tree of the first type is restricted to the hilus and str.lucidum of the CA3 subfield, with always myelinated axons, and because of the presence of often branching spines on their dendrites they are named as spiny calretinin-interneurons. The second type is referred to as spine-free calretinin-interneuron. A remarkable feature of calretinin-interneurons is the formation of dendro-dendritic and axo-dendritic contacts with other calretinin-interneurons. Moreover, they also form synaptic contacts with other calbindin, calretinin and vasoactive intestinal peptide-immunoreactive interneurons (Gulyás et al., 1996). Besides calretinin-containing IS interneurons, vasoactive intestinal peptide-positive IS interneurons have also been

described. However, these cells were identified in the CA1 region (Acsády et al., 1996; Chamberland et al., 2010; Tyan et al., 2014).

III.1.3.4. Long-range projecting GABAergic cells

In addition to the local circuit of GABAergic cells, a specific subpopulation of inhibitory neurons sends long-range inhibitory projections to subcortical and other cortical areas. These cells are called *long-range projecting GABAergic cells*.

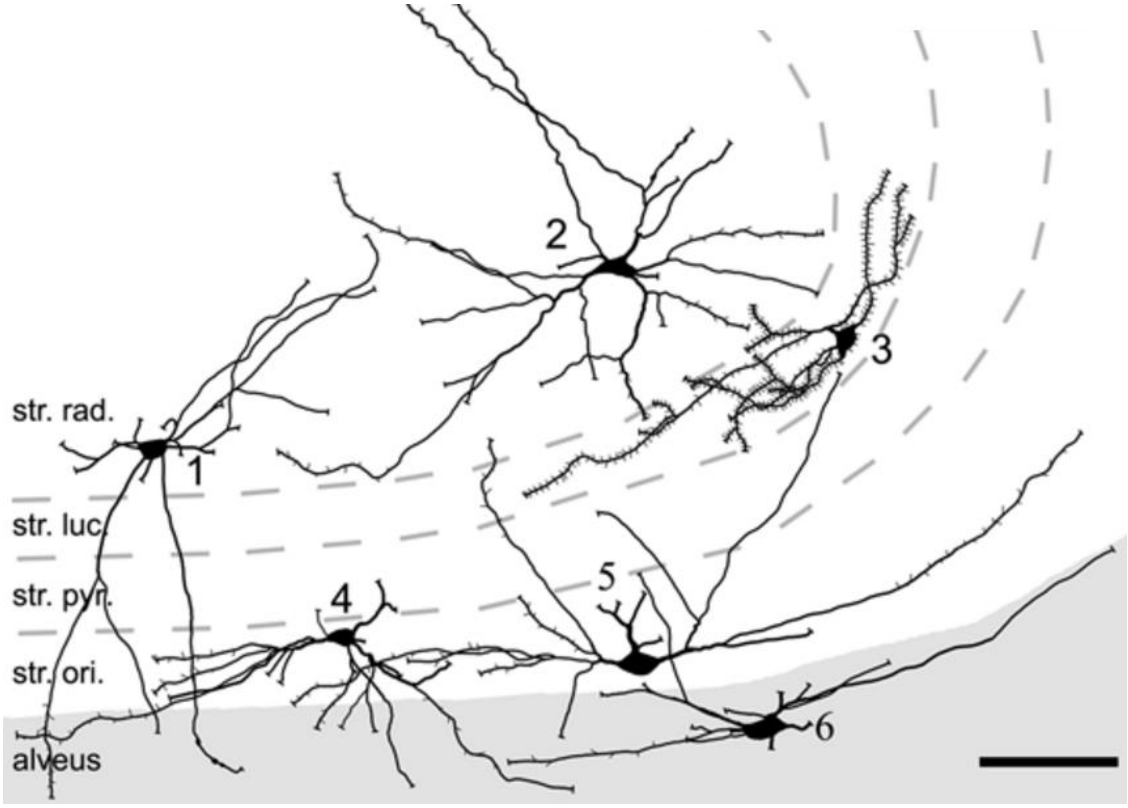

Figure 4. Camera lucida reconstruction of retrogradely labeled CA3 spine-free and spiny hippocampo-septal cells. *The soma of spine-free hippocampo-septal (HS) cells are found in strata radiatum (1,2), oriens (4, 5) and alveus (6). HS cells in str.oriens and alveus have horizontally oriented spine-free dendrites located mainly in str.oriens and alveus. The dendrites of spine-free HS cells in the str.radiatum run in all directions and penetrate all layers. Densely-spiny HS cells (3) in the CA3 area located always in the str.lucidum. str.rad., stratum radiatum; sr.luc., stratum lucidum; str.pyr., stratum pyramidale; str.ori., stratum oriens. Scale bar, 100 μm. Adopted from Takács et al., (2008), with permission.*

The *hippocampo-septal cells* innervate the most studied remote target of hippocampal GABAergic cells, the medial septum (MS). The sparsely spined hippocampo-septal cell somata are located in str. oriens and str. radiatum, where recurrent axons of pyramidal cells arborize. On the other hand, the soma of densely spined hippocampo-septal cells (characterized by profusely covered dendrites and elongated soma with spines) is observed in str. lucidum (Figure 4) (Takács et al., 2008). They give rise to myelinated axons projecting back to the medial septum-diagonal band of Broca, as well as to local collaterals, where they target local pyramidal cells and interneurons in strata oriens and radiatum (Gulyás et al., 2003; Jinno et al., 2007; Takács et al., 2008). Hippocampo-septal cells receive inhibitory inputs from the MS, thus these two regions are reciprocally connected (Raisman et al., 1966; Takács et al., 2008). The main postsynaptic targets of hippocampo-septal cells in the MS are PV-expressing GABAergic and cholinergic neurons (Tóth et al., 1993).

CA3 *Trilaminar cells* show several similarities to O-LM cells: they have cell bodies in str. oriens and their dendritic tree is restricted to this region. However, their axons are distributed to three adjacent layers: strata radiatum, pyramidale and oriens, and also send axon collaterals into neighboring areas (i.e. to CA1 and subiculum) (Gloveli et al., 2005; Hájos et al., 2004). The postsynaptic targets of trilaminar cells include both pyramidal cells and interneurons (Ferraguti et al., 2005).

III.2. Behavior related activity patterns of the hippocampus

The hippocampus plays prominent role in spatial and episodic memory formation, which processes require a precisely synchronized and coordinated activity of distributed neurons. The alternating firing and non-firing periods of cell populations (including both interneurons and principal cells) are responsible for the synchronized synaptic potentials of targeted neurons, which are manifested as oscillatory patterns on the EEG (Colgin, 2016). In rodents, hippocampal rhythms (EEG patterns) include theta rhythms (4-12 Hz) (Bullock et al., 1990), sharp wave associated ripple oscillation (SWRs, 100-250 Hz ripples superimposed on 0.5-3Hz sharp waves) (Buzsáki, 1986) and gamma rhythms (30-100 Hz) (Csicsvari et al., 2003) (Figure 5). Each rhythm is observed during particular

DOI:10.14753/SE.2018.2077

behavioral pattern, is associated with characteristic neuronal firing properties, and is thought to carry out distinct functions (Colgin, 2016).

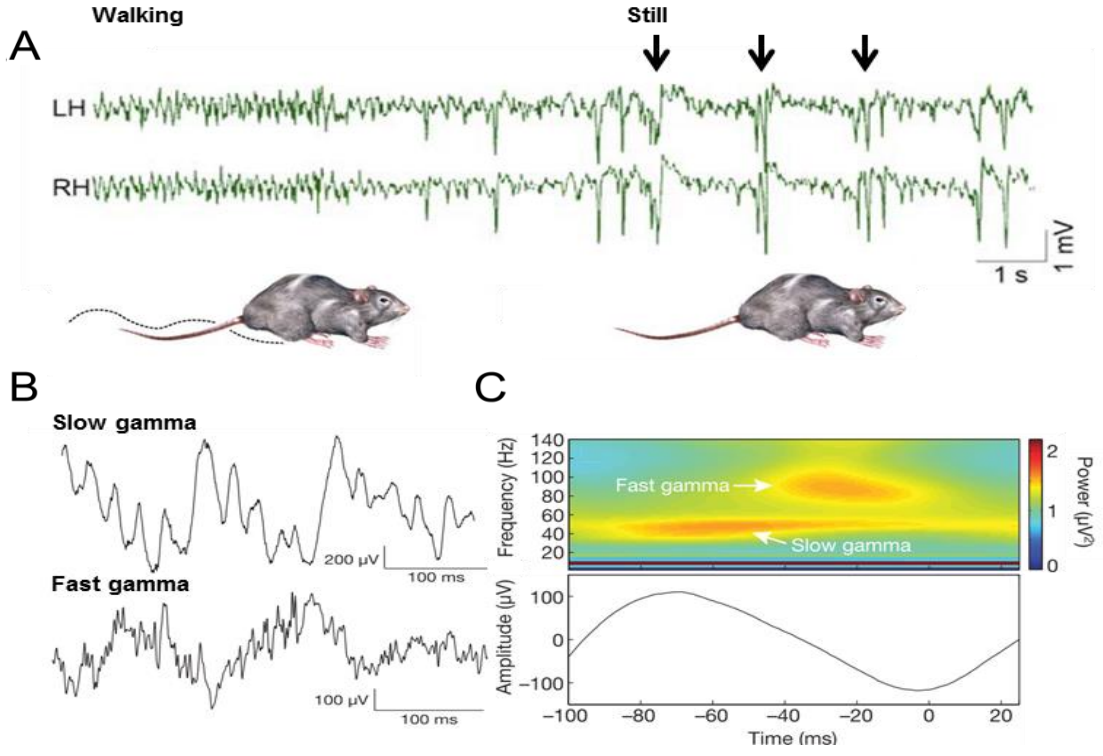

Figure 5. Network activity patterns in the hippocampus in vivo. *A: Local field potential recording from symmetrical locations of the left (LH) and right (RH) dorsal CA1 stratum radiatum during locomotion (walking) and awake immobility (still). Note the transition from theta rhythm during exploration to large irregular activity interrupted by sharp wave-ripples (black arrows). Adopted from Buzsáki, 2015. B: Example of slow gamma (25-50 Hz) and fast gamma (65-140 Hz) oscillation from CA1 stratum pyramidale. C: Time frequency representation of power for representative recording in B (top), averaged across all theta cycles (bottom). Frequency is plotted on the y axis, time point t = 0 correspond to the theta trough. Note that slow and fast gamma are associated with different portions of the underlying theta cycle. Adapted from Colgin et al., 2009.*

The EEG rhythms originate from the synchronized activity of pyramidal cells reflecting the electrical changes in the extracellular space. During oscillations, the firing of pyramidal cells is synchronized, and this synchrony is mediated by the fast synaptic inhibition originating from GABAergic interneurons (Colgin, 2016) (Figure 5). As single hippocampal interneurons can target multiple postsynaptic cells (including pyramidal cells and interneurons of the same type), the output of many GABAergic neurons could entrain the activity of large number of cells within the network (Figure 6). Thus,

DOI:10.14753/SE.2018.2077

GABAergic interneurons contribute to the alteration of firing and non-firing periods of cell populations, resulting in different oscillatory patterns on EEG (Gonzalez-Burgos and Lewis, 2008).

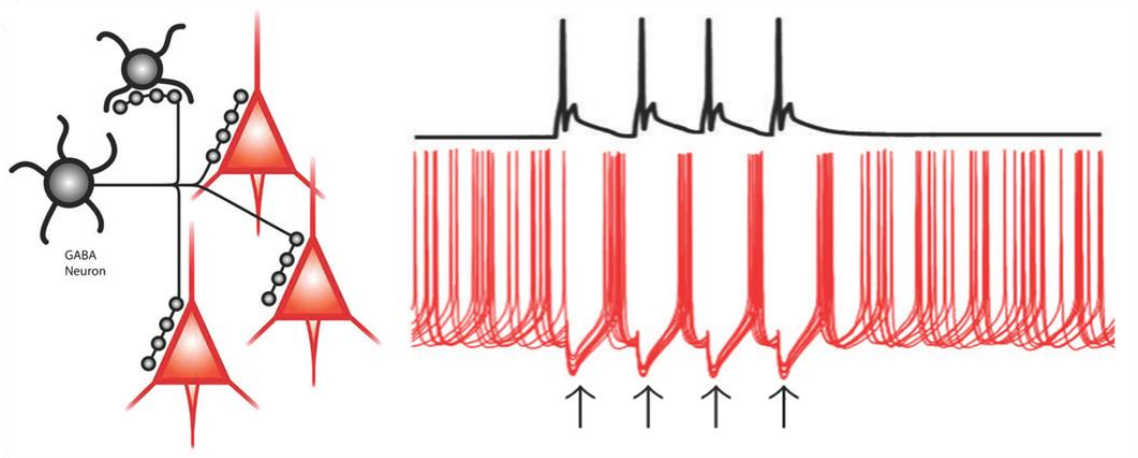

Figure 6. The GABA$_A$R-mediated inhibition provided by GABAergic interneurons is efficient in synchronizing neuronal activity. *The diagram on the left indicate that the axons of individual perisomatic region-targeting GABAergic cells (black) form multiple contacts with postsynaptic pyramidal cells (red) and other GABAergic cells. The right panel shows the membrane potential of the GABAergic cell (black trace) and superimposed traces of membrane potential of three pyramidal cells (red) illustrating how the asynchronous firing of pyramidal cells becomes transiently synchronized by the phasic inhibition provided by the GABAergic cell. Shortly after the presynaptic action potential, an inhibitory postsynaptic potential is produced (black arrows) preventing postsynaptic pyramidal cells from firing. When inhibition decays, the pyramidal cells fire nearly in synchrony. Adapted from Gonzalez-Burgos & Lewis, 2008 and Gonzalez-Burgos et al., 2011.*

III.2.1. Theta oscillation in the hippocampus

A prominent network pattern in the hippocampus is a slow oscillation in the theta frequency range (4-12 Hz). During wakefulness theta is associated with voluntary movement and exploratory behavior, during which the animal gains new information about the environment (Berry and Thompson, 1978) (Figure 5). Theta also occurs during rapid eye movement sleep (Jouvet, 1969) and occasionally during immobile attention or arousal (Buzsàki and Eidelberg, 1983).

Theta oscillation is the most regular in frequency and has a largest amplitude in the stratum lacunosum-moleculare of CA1 (Kamondi et al., 1998). Besides hippocampus

theta has been observed in other brain regions including the subiculum (Paré et al., 2002), striatum (DeCoteau et al., 2007), neocortex (Kahana et al., 2001), hypothalamus (Kocsis and Vertes, 1997) and medial septum (Vinogradova et al., 1995).

The hippocampal theta activity depends critically on the integrity of the afferent inputs from the medial septum (MS). MS contains two major types of neurons that are thought to play distinct roles in the theta rhythm generation: cholinergic cells modulate the activity of hippocampal pyramidal cells (Cole and Nicoll, 1984), whereas GABAergic cells are targeting hippocampal interneurons (Freund and Antal, 1988). It has also been reported, that MS GABAergic cells expressing parvalbumin can drive hippocampal theta activity by rhythmic disinhibition of hippocampal pyramidal cells (Hangya et al., 2009). Because the largest amplitude theta oscillations are observed in CA1 stratum lacunosum-moleculare (Kamondi et al., 1998), rhythmic excitation of the distal apical dendrites of pyramidal cells by entorhinal afferents is also assumed to play an important role in the theta oscillation generation (Buzsáki, 2002).

Combining these data proposed a model for hippocampal theta generation: the cholinergic neurons of MS provide slow depolarization of their pyramidal cell targets; meanwhile MS GABAergic neurons mediate rhythmic disinhibition of pyramidal cells. The rhythmic excitatory postsynaptic potentials provided by the input from the entorhinal cortex are responsible for the current sink in the stratum lacunosum-moleculare (Buzsáki, 2002).

Hippocampal theta oscillation has a well-established role in memory encoding (Buzsáki and Moser, 2013). The impairment in a spatial memory task caused by the lesion of the MS correlates with the reduction of hippocampal theta rhythm (Rawlins et al., 1979; Winson, 1978) and causes impairment in tasks including delayed spatial alternation (Givens and Olton, 1990), delayed non-match to position (Markowska et al., 1989) and spatial reversal (M'Harzi et al., 1987). Moreover, theta may also integrate various types of sensory information received by the hippocampus by linking neurons coding different aspects of the same experience. As theta correlate with movements to acquire sensory stimuli, they are well suited to coordinate multimodal sensory information (such as olfactory and visual inputs) (Colgin, 2016).

DOI:10.14753/SE.2018.2077

III.2.2. Gamma oscillation in the hippocampus

Hippocampal gamma rhythms (30-100 Hz) are thought to provide a temporal structure for information processing in the brain, and contribute to cognitive functions, such as memory formation and sensory processing (Bartos et al., 2007) through coordinating cell assemblies (Colgin and Moser, 2010). They are commonly seen superposed onto the theta rhythm during exploration (theta-nested gamma) (Figure 5), but can also be observed in the absence of theta activity in both awake and anesthetized rodents (Csicsvari et al., 2003; Penttonen et al., 1998).

Hippocampal gamma oscillations are thought to be generated in two independent ways (Colgin and Moser, 2010). In behaving rats, the largest estimated excitatory currents during gamma oscillation are observed in the middle third of the DG molecular layer, which is the termination zone for the medial EC projection. In the EC, gamma oscillation arises at high frequency (~ 90 Hz, "fast gamma"), and can spread to the DG and to the CA regions (Bragin et al., 1995). The activity of the lower gamma frequency range (30-50 Hz) is termed as "slow gamma" and is driven by the CA3 region itself (Csicsvari et al., 2003). The two gamma oscillators have been shown to be independent but still able to couple in time, allowing the alternating processing of information originating from the EC or CA3 region (Colgin et al., 2009).

Current source density analysis of intrinsically generated "slow gamma" oscillation revealed alternating pairs of sinks and sources in the str. pyramidale and radiatum of both the CA3 and CA1 region. The sink-source pairs of CA3 precedes those observed in CA1 suggesting, that the "slow gamma" generated in CA3 entrains CA1 circuitry (Csicsvari et al., 2003). The capability of CA3 to generate gamma oscillation is likely due to the recurrent excitatory collateral system among pyramidal cells (Hájos and Paulsen, 2009). The rhythmic discharge of perisomatic region-targeting interneurons is also pivotal for the emergence of gamma oscillation within the CA3 network, especially PV-containing inhibitory neurons (Mann *et al.*, 2005; Cardin *et al.*, 2009; Szabó *et al.*, 2010; Gulyás *et al.*, 2010).

III.2.3. Sharp wave-ripples in the hippocampus

Sharp wave-ripples (SWRs) are large amplitude, irregularly occurring hippocampal activity pattern observed in animals during waking immobility, consummatory behaviors and slow-wave sleep (Buzsáki, 1986; O'Neill et al., 2006) (Figure 5). The possible role of SWRs originates from theories suggesting their specific role in hippocampus-dependent memory consolidation during sleep (Buzsáki, 1989; Csicsvari and Dupret, 2014). As during SWRs large number of neurons fire synchronous action potentials, it has been suggested that during SWRs the previous network activity is reactivated, which represents memory traces that might undergo memory consolidation and could enable the transfer of memory traces to extra-hippocampal regions (Girardeau et al., 2009; Nádasdy et al., 1999; Wilson and McNaughton, 1994). On the other hand, awake SWRs in particular can reactivate sets of place fields encoding forward and reverse paths associated with both current and past locations. This reactivation during awake SWRs can contribute to learning, memory retrieval and consolidation, as well as trajectory planning (Carr et al., 2011; Dupret et al., 2010; Jadhav et al., 2012; O'Neill et al., 2010).

SWRs in CA1 can be reorganized based on two particular local field potential patterns. While the strong negative deflection with 50-100 ms duration in the CA1 str. radiatum reflects the synchronous discharge of CA3 pyramidal cells (giving rise to excitatory inputs to CA1 pyramidal cell dendrites), the high frequency ripple oscillation (120-200 Hz) represents the rhythmic activation of interneurons and pyramidal cells to the strong depolarization and synchronous drive (Buzsáki, 2015).

The CA3 region is known to be implicated in the generation of SWRs. CA3 pyramidal cells (especially CA3a adjacent to CA2 and distal CA3b) give rise to extensive and strongly recurrent collateral system, which enables the generation of population bursts (Traub and Wong, 1982). Interestingly, the CA2 region mirrors several aspects of CA3a (Tamamaki et al., 1988). It has been recently shown, that superficial CA2 pyramidal cells fire prior to synchronized activity of CA3 neurons, and the population activity from CA2 spreads to CA3a-b and c and finally to CA1 subregion of the hippocampus. These results suggest that CA2 region could play a leading role in the initiation of SWRs (Oliva et al., 2016). These rhythmic burst from CA2 (CA3) finally

propagate to CA1 region, where they reach both pyramidal cells and inhibitory neurons via feed-forward manner (Csicsvari et al., 1999b, 1999a).

During SWRs only a subset of pyramidal cells is active at a low firing rate, while the majority of them are silent (Ellender et al., 2010; Sullivan et al., 2011; Wu et al., 2005). However, the co-activation of these subsets of pyramidal cells (often called "ensembles") strongly excites GABAergic interneurons, especially PV+ basket cells (Buzsáki, 2015; Stark et al., 2014). The tonic excitatory envelop drives reciprocally connected PV+ basket cells, which, in turn, give rise to ripple-frequency spiking that is phase-locked through reciprocal inhibition. These results support the hypothesis that the sufficiently excited network of reciprocally connected PV+ basket cells is sufficient to generate SWRs (Schlingloff et al., 2014).

III.2.4. Pathological oscillation in the hippocampus

The hippocampus shows oscillatory activities with different frequencies ranging from 4 Hz to up to >100 Hz. The irregularly occurring, transient, high activity events carry distinct forms of superimposed high frequency oscillation (HFO). Transient HFOs are field potentials that reflect short-term synchronization of neuronal activity, and are believed to play important role in both physiological and pathological brain states (Engel et al., 2009).

The frequency spectrum covered by HFOs has been subdivided into so called ripples (80-200 Hz) (Buzsáki et al., 1992) and fast ripples (200-500 Hz) (Bragin et al., 1999a). It is assumed by several research groups that ripples reflect physiological and fast ripples reflect pathological HFO. However, the distinction cannot be based on the differences in their respective frequency range alone: fast ripples can be recorded from different areas of normal neocortex, whilst ripple frequency range can be observed in epileptic DG where normal ripples never occur (Engel et al., 2009; Menendez de la Prida et al., 2015).

Pathological HFOs are historically linked to "fast ripples" described in the hippocampus and entorhinal cortex of rats with recurrent spontaneous seizures (250-500 Hz) (Bragin et al., 1999a). These oscillations were termed fast ripples as they were "faster" than normal, sharp wave-associated ripple oscillation (100-200 Hz) (Buzsáki et

al., 1992). In animal models of chronic limbic epilepsy, HFO with frequency range of 250-500 Hz occur in the DG, CA1, CA3, subiculum and entorhinal cortex, but only in rats exhibiting spontaneous seizures (Bragin et al., 1999b, 1999a). This interictal HFOs, or fast ripples, are considered to be pathological, as they are associated with sites of seizure onset (Bragin et al., 1999b, 2000). Moreover, they sometimes precede seizure onset, (Jirsch et al., 2006; Khosravani et al., 2009), but exclusively in epileptogenic regions (Bragin et al., 2000) and do not appear in animals subjected to epileptogenic insult without exhibiting epileptic seizure (Bragin et al., 1999a).

The neuronal mechanism underlying physiological and pathological HFOs are thought to involve different degrees of interneuron-mediated inhibition. During physiological ripples, neuronal firing occurs around the ripple, and reflects the synchronous firing of approximately 20% of pyramidal cells, coordinated by the synchronous interneuron-mediated inhibitory postsynaptic potentials (Jefferys et al., 2012; Menendez de la Prida et al., 2015; Schomburg et al., 2012; Ylinen et al., 1995). In contrast, pathological HFOs reflect brief bursts of population spikes arising from groups of abnormally synchronized principal cells within local areas (Bragin et al., 2000). However, the exact mechanism of pathological HFOs is not clear, and one of the main goals of this thesis is to reveal possible underlying mechanisms of pathological HFO generation.

III.3. Forms and mechanisms of short-term synaptic plasticity

During physiological activity patterns, the dynamic modification of synaptic connectivity enables the brain to adequately respond to environmental changes. Although synapses throughout the brain share many features, they also have distinct properties. In the majority of cases, the same general sequence of events leads to neurotransmitter release: an action potential generated in the presynaptic neuron is propagated down the axon, where Ca^{2+} ions entering the presynaptic terminal through voltage-gated calcium channels trigger vesicle fusion. The liberated neurotransmitter binds to the receptors on the postsynaptic cell and triggers postsynaptic response (reviewed in Blitz *et al.*, 2004). The synaptic transmission is highly dependent on recent neuronal activity, and the synaptic efficacy can increase (synaptic facilitation) or decrease (synaptic depression) on

timescales from a few milliseconds to several tens of seconds after the onset of specific temporal activity pattern. This temporal increase or decrease of synaptic strength in response to use is called short-term plasticity, and can directly affect the timing and integration of presynaptic inputs to postsynaptic neurons (Fortune and Rose, 2001). The short-term variations of synaptic efficacy (short-term facilitation – STF, short-term depression - STD) may serve critical roles in the processing of complex and natural streams of activity (Kandaswamy et al., 2010; Klyachko and Stevens, 2006), and can directly affect the synaptic and circuit function during computation (Abbott and Regehr, 2004).

The strength of connection is fundamentally dependent on three main factors: the number of synaptic contacts, the probability of neurotransmitter release at each synapse and the amplitude of the postsynaptic response elicited by the release of neurotransmitters from a single vesicle (quantal size). Short-term plasticity is a synapse-specific phenomenon that depends on the identity of both pre- and postsynaptic neurons (Losonczy et al., 2002; Markram et al., 1998; Reyes et al., 1998; Zucker and Regehr, 2002). It is generally agreed that factors contributing to short-term plasticity are located presynaptically, however, the properties of postsynaptic receptors can also contribute to short-term plasticity (Blitz et al., 2004; Hennig, 2013).

The extent of short-term plasticity depends on the initial probability of release. Synapses with a high initial probability of neurotransmitter release tend to depress, whilst synapses with low release probability usually facilitate (Regehr, 2012).

For most synapses with low initial release probability, the repeated stimulation at short intervals leads to short-term facilitation. According to the hypothesis introduced by Katz & Miledi (1968), the initial presynaptic action potential evokes local increase of calcium concentration (Ca_{local}), which triggers neurotransmitter release. After the action potential and neurotransmitter release, the calcium persists at a lower level (called residual calcium, Ca_{res}) in the presynaptic bouton. This means that the consequent action potential would result in facilitation if the Ca_{res} concentration becomes a significant fraction of the local calcium signal. However, Ca_{res} represents only 1% of Ca_{local} suggesting that this mechanism results only in a moderate increase of Ca_{res} and a very little facilitation (Regehr, 2012). It has also been hypothesized that Ca_{res} increases release probability by acting on a calcium sensor distinct from synaptogamin (Atluri and Regehr,

1996). Synaptogamin binds Ca^{2+} rapidly, but with low affinity, and can respond quickly to a brief Ca^{2+} signal and can evoke rapid vesicle fusion. A calcium sensor with high-affinity calcium-binding site with slow kinetics might respond slowly to calcium and Ca_{res}. As a consequence of repeated presynaptic action potentials the increased Ca_{res} fraction of Ca_{local} can be responsible for facilitation (Fioravante and Regehr, 2011). Such a good candidate for calcium sensor located presynaptically, binding Ca^{2+} with high affinity and slow kinetics is synaptotagmin7. It has been shown by Jackman et al. (2016) that the deletion of synaptotagmin 7 eliminates short-term facilitation without altering the initial release probability at facilitating Schaffer collateral synapses between hippocampal CA3 and CA1 pyramidal cells, thalamocortical synapses between layer VI cortical pyramidal cells and thalamic relay cells, mossy fiber synapses between DG granule cells and CA3 cells, and perforant path synapses between layer II and II cells of the entorhinal cortex and granule cells. These results show that synaptotagmin 7 plays a crucial role in mediating short-term facilitation, as it may act as the proposed specialized Ca^{2+} sensor to increase release probability during facilitation (Jackman et al., 2016).

Short-term depression, which is represented by a transient decrease of synaptic strength during trains of presynaptic stimulation have predominantly presynaptic origin. Many aspects of STD are explained by the depletion of the readily releasable pool (Fioravante and Regehr, 2011). According to this model, the number of vesicles released by an action potential depends on the size of the readily releasable pool (RRP), as well as on the release probability of vesicles. If an action potential releases a large fraction of the RRP, the subsequent stimulation (action potential) will release fewer vesicles, as the released vesicles are not immediately replenished (Zucker and Regehr, 2002). The sustained high-frequency stimulation of presynaptic neurons results in profound depression, however, the recovery from this depression in the order of several second and can be significantly accelerated by elevating of presynaptic calcium (Dittman and Regehr, 1998; Dittman et al., 2000). Thus the extent of depression crucially depends on the number of vesicles in the RRP at each active zone, the number of vesicles released by an action potential and the replenishment of vesicles in the RRP (recovery from depression) (Hennig, 2013; Zucker and Regehr, 2002).

Short-term plasticity can also be mediated by postsynaptic mechanisms. Desensitization of postsynaptic receptors can reduce synaptic responses during repeated

DOI:10.14753/SE.2018.2077

activation of presynaptic neurons (Jones and Westbrook, 1996; Sun et al., 2002). In addition, this repetitive activity can also lead to receptor saturation and subsequent decrease of synaptic response. However, there is a marked difference between receptors with slow (NMDA receptors) and fast (AMPA receptors) kinetics. It has been shown by Chen et al. (2002), that the presynaptic bursts pronounced AMPA receptor desensitization and reduced the efficacy of AMPA component, whereas the NMDA component was accentuated during the same burst.

DOI:10.14753/SE.2018.2077

IV. AIMS OF THE THESIS

The main goal of this thesis is to understand how the same network (CA3 region of hippocampus) can produce different forms of activity patterns, i.e. physiological sharp wave-ripples and pathological interictal-like events; and how pyramidal cells and interneurons contribute to the dynamics of these transient high activity states. Therefore, two main objectives were determined:

The first objective was to uncover the differences between physiological sharp wave-ripples and interictal-like events, and reveal the underlying mechanisms resulting in the transition from the physiological to the pathological network state. For this purpose, we asked the following questions:

- What is the phenomenological difference between physiological sharp wave-ripples and pathological interictal-like events?
- How the same identified principal cells and interneurons behave during sharp wave-ripples and interictal-like events?
- What network and cellular mechanisms underlie the transition from sharp wave-ripples to interictal-like events?

The transition from sharp wave-ripples to interictal-like events, the activity of identified CA3 neurons as well as the membrane potential changes of principal cells and interneurons were recorded together with Dr. Rita Karlócai (RESULTS part VI.1.1.-VI.1.7.). Dr. Rita Karlócai conducted electrical stimulation experiments (RESULTS part VI.1.8.). The paired recordings between monosynaptically coupled interneurons and pyramidal cells were performed by me (RESULTS part I.9)

The second objective was to quantitatively and qualitatively describe the connectivity of perisomatic and dendritic region-targeting interneurons in the hippocampal CA3 area, with attention on the following points:

- Can different classes of CA3 interneurons be distinguished based on their passive and active membrane properties? (The electrophysiological characterization and clustering analysis of CA3 interneurons was performed by Dr. Szabolcs Káli)

DOI:10.14753/SE.2018.2077

- What is the connection trend between different classes of CA3 interneurons?
- Are there differences in the properties of unitary transmission and short-term dynamics between interneurons and their pyramidal cell and interneuron targets?
- Can mathematical models of short-term plasticity effectively capture the transmission properties of different types of hippocampal interneurons? (Mathematical models were designed and fitted to the data by Dr.Szabolcs Káli)
- What is the possible physiological relevance of short-term plasticity in the sharp wave-ripple generating state? (Optogenetic experiments were performed by Dániel Schlingloff)

DOI:10.14753/SE.2018.2077

V. MATERIALS AND METHODS

V.1. Animals

Animals were kept and used according to the regulations of the European Community's Council Directive of November 24, 1986 (86/609/EEC), and experimental procedures were reviewed and approved by the Animal Welfare Committee of the Institute of Experimental Medicine, Hungarian Academy of Sciences, Budapest. We used several mouse strains. CD1 and C57BL/6J mice of both sexes (postnatal day 19-40) were used to investigate the network parameters of transition from sharp wave-ripples to interictal-like events. Transgenic mice expressing enhanced green fluorescent protein (eGFP) controlled by PV promoter (BAC-PV-eGFP) (Meyer et al., 2002) or red fluorescent protein (DsRED) under the control of the cholecystokinin promoter (BAC-CCK-DsRED) (Máté *et al.*, 2013) were used to facilitate cell type selection (postnatal days 19-40). For optogenetic stimulation of PV+ cells, the B6;129S-*Gt(ROSA)26Sor*$^{tm32(CAG-COP4*H134R/EYFP)Hze}$/J (The Jackson Laboratory; RRID:IMSR_JAX:012569) strain was crossed with B6;129P2-Pvalbtm1(cre)Arbr/J (The Jackson Laboratory; RRID:IMSR_JAX:008069) animals to generate mice that selectively express channelrhodopsin-2 under the PV promoter.

V.2. Slice perparation

Mice of both sexes were decapitated under deep isoflurane anesthesia. The brain was quickly removed and placed into an ice-cold cutting solution containing the following (in mM): 205 sucrose, 2.5 KCl, 26 $NaHCO_3$, 0.5 $CaCl_2$, 5 $MgCl_2$, 1.25 NaH_2PO_4, 10 glucose, saturated with 95% O_2-5% CO_2. Horizontal hippocampal slices (250-350 μm thick slices for paired recording, 450 μm thick slices for transition from sharp wave-ripples to interictal-like events and optogenetic experiments) were prepared using a Leica VT1000S or a VT1200S microtome (Leica, Nussloch, Germany), and slices were placed into an interface-type holding chamber at room temperature for at least 60 min. for recovery in standard ACSF with the following composition (in mM): 126 NaCl, 2.5 KCl, 26 $NaHCO_3$, 2 $CaCl_2$, 2 $MgCl_2$, 1.25 NaH_2PO_4, 10 glucose, saturated with 95% O_2-5% CO_2. The composition of modified ACSF (mACSF) used in all experiments was as

follows (in mM): 126 NaCl, 3.5 KCl, 26 $NaHCO_3$, 1.6 $CaCl_2$, 1.2 $MgCl_2$, 1.25 NaH_2PO_4, 10 glucose, saturated with 95% O_2-5% CO_2.

V.3. Electrophysiological recordings

After incubation slices were transferred individually into a submerged type recording chamber. The flow rate of mACSF was 4-5 ml/min at 30-32˚C (Supertech Instruments; www.super-tech.eu). Slices were visualized with an upright microscope (Olympus; BX61WI) with infrared-differential interference contrast optics. Fluorescence of eGFP-containing PV+ and DsRED-containing CCK+ cells was induced with standard epifluorescence using a UV lamp. Whole-cell patch-clamp recordings were made using a Multiclamp 700B amplifier (Molecular Devices), low-pass filtered at 3 kHz, digitized at 10 kHz with a PCI-6024E board (National Instruments, Austin, TX, USA), recorded with an in-house analysis software (Stimulog, courtesy of Professor Zoltán Nusser, Institute of Experimental Medicine, Hungarian Academy of Sciences), and analyzed off-line using EVAN software (courtesy of Professor István Mody, UCLA, CA) or custom-made programs written in MATLAB 7.0.4. and Delphi 6.0 by A.I.G.

Standard patch electrodes (pulled from borosilicate glass capillaries with inner filaments, 1.5 mm O.D.; 1.12 mm I.D., Hilgenberg GmbH, Malsfeld, Germany) were used in all recording configurations. Pipette resistances were 3-6 MΩ when filled with intrapipette solution.

V.3.1. Local field potential recording

Local field potential (LFP) recordings were performed with ACSF-filled standard patch pipettes (3-6 MΩ). LFP recordings were made using a Multiclamp 700B amplifier (Molecular Devices), low-pass filtered at 3 kHz, digitized at 10 kHz with a PCI-6024E board (National Instruments, Austin, TX, USA). Data were recorded with EVAN 1.3 software (courtesy of Prof. I. Mody, University of California Los Angeles, Los Angeles, CA). All data were analyzed off-line using custom-made programs written in MATLAB 7.0.4. and Delphi 6.0 by A. I. G.

V.3.2. Multichannel local field potential recording

The local field potential was recorded with a laminar multi-electrode array placed on the surface of the hippocampal slice, parallel to the orientation of pyramidal cell dendrites spanning all hippocampal layers (24 channels, 50 µm inter-contact distance, Neuroneelektród Kft.). We used a custom-made referential amplifier system (band-pass 0.1 Hz to 7 kHz) (Ulbert et al., 2001, 2004). Signals were digitized with a 16 bit resolution analogue-to-digital converter (National Instruments) and recorded at 20 kHz sampling rate on each channel using a custom-made virtual instrument in LabView (National Instruments). Current Source density calculations were made using a three-point formula smoothed by Hamming window (Ulbert et al., 2001). Results are depicted by heat map using custom-made software (written by A.I.G.).

V.3.3. Optical stimulation

For optical stimulation a Blue Laser Diode module at 447 nm (Roithner LaserTechnik Gmbh) was used to illuminate the whole slice. In contrast to other experiments, we used older animals (postnatal day 60-300) because of low expression of channelrhodopsin-2-EYFP before this age. Sharp wave-ripples were evoked by 10 ms long light illumination every 1000 ms.

V.3.4. Paired recordings

For paired recordings, three types of intrapipette solution were used: (1) ***high KCl intrapipette solution*** (composition in mM: 54 D-gluconic acid potassium salt, 4 NaCl, 56 KCl, 20 HEPES, 0.1 EGTA, 10 phosphocreatine di(tris) salt, 2 ATP magnesium salt, 0.3 GTP sodium salt; with 0.2 % biocytin; adjusted to pH 7.3 using KOH and with osmolarity of 294 mOsm/L), (2) ***low KCl intrapipette solution*** (composition in mM: 110 D-gluconic acid potassium salt, 4 KCl, 20 HEPES, 0.1 EGTA, 10 phosphocreatine di(tris) salt, 2 ATP magnesium salt, 0.3 GTP sodium salt; with 0.2 % biocytin; adjusted to pH 7.3 using KOH with osmolarity of 290 mOsm/L) and (3) ***high CsCl intrapipette solution*** (composition in mM: 80 CsCl, 60 Cs-gluconate, 1 $MgCl_2$, 2 ATP magnesium salt, 10 HEPES, 3 NaCl, 5 QX-314 Cl [2(triethyloamino)- N-(2,6-dimethylphenyl) acetamine], with 0.2 % biocytin; adjusted to pH 7.3 using CsOH with osmolarity of 295 mOsm/L). Inhibitory transmission between IN-PC and IN-IN pairs as well as connection probability between

INs was recorded with high KCl intrapipette solution for both pre- and postsynaptic cells. In some experiments, the inhibitory transmission between INs and PCs was performed with low KCl intrapipette solution for presynaptic IN and high CsCl intrapipette solution for postsynaptic PC. In all experiments, presynaptic INs were held at -65 mV in current clamp configuration, postsynaptic cells were held at -60 mV in voltage clamp configuration. Series resistance was not compensated, but frequently monitored, and cells where the values changed more than 25% during recording were discarded from further analysis.

V.3.5. Investigation of short-term plasticity and unitary synaptic properties

To investigate the properties of evoked IPSCs from PTIs, excitatory currents were blocked by 20 μM NBQX and 50 μM AP-5. When studying the transmission of CCK+ cells, AM251 in a concentration of 1 μM was added to the superfusate to block CB_1 cannabinoid receptor function.

To analyze the short-term plasticity of synaptic transmission between INs and their PC or IN targets, presynaptic INs were stimulated with brief current injections (1500 pA for 1 ms) to evoke a train of APs in one of the following patterns. To systematically map the response of synaptic connections to the range of frequencies characterizing ongoing hippocampal activity (Buzsáki, 2002; Colgin *et al.*, 2009; Gulyás *et al.*, 2010; Hájos *et al.*, 2013; Lasztóczi & Klausberger, 2014; Schlingloff *et al.*, 2014), we used regular trains of 10 stimuli at frequencies 1 Hz, 5 Hz, 10 Hz, 20 Hz, 40 Hz, 80 Hz, 160 Hz and 320 Hz, followed by a single stimulus at recovery time of 1000 ms. Each of these input patterns was repeated 10 times, with 1 s intervals between the two trains. We also tested the response of connections to inputs reflecting the behavior of perisomatic-region targeting interneuron (PTIs) during sharp wave-ripples (RIP protocol - 4 APs at 160 Hz, Hájos et al., 2013) and pathological interictal-like events (EPI protocol - 30 APs at 160 Hz followed by 4 APs at 320 Hz. These patterns were preceded by a single pulse at an interval of 1000 ms, and were repeated 10 or 20 times, with 1600 ms intervals between the last pulse of the trains and the subsequent single pulses. The time constant of recovery from inhibition was calculated using stimuli, which consisted of two consecutive RIP protocols where the time between the two RIP patterns was systematically varied. The intervals used were 50 ms, 100 ms, 200 ms, 300 ms, 500 ms, 800 ms, and 1200 ms (each

repeated 10 times), representing the inter-event interval distribution of *in vitro* sharp wave-ripples (Schlingloff et al., 2014). The recovery from inhibition between PTI-PC pairs was then estimated as the proportion of the amplitude of the first IPSC in the second part of the stimulation train (second RIP protocol) to the amplitude of the first IPSC in the first part of the train (first RIP protocol).

The kinetic properties (10-90% rise times, decay time constant, latency), synaptic potency and transmission probability of uIPSCs were calculated on averaged events excluding failures; the amplitude of uIPSCs was calculated on averaged events including failures. The latency of synaptic transmission was calculated by subtracting the time of the action potential peaks from the start point of evoked uIPSCs (estimated from the intersection of the baseline with the linear fit to the 10-90% rising phase of uIPSCs). Fitting of a single exponential function to the decaying phase of averaged uIPSCs and statistical analysis were performed in Origin 9.0 software (OriginLab Corporation, Northampton, MA, USA). To analyze short-term plasticity, the relative amplitude of evoked IPSCs was calculated by normalizing to the amplitude of the first IPSC.

V.3.6. Stimulation-evoked postsynaptic currents

To record stimulation-evoked currents, 200 μm thick slices were used to minimize spontaneous network activity. Evoked inhibitory- and excitatory postsynaptic currents were recorded in PCs at a holding potential of -70 mV. A stimulating electrode made of theta glass was placed into stratum radiatum to activate Schaffer collaterals or inhibitory fibers, or into the border of strata pyramidale and lucidum to evoke inhibition with a perisomatic origin. When recording inhibitory postsynaptic currents, the artificial CSF contained 20 μM NBQX and 50 μM AP-5 to block fast excitatory transmission; when excitatory postsynaptic currents were recorded, the borders of CA3a-b and CA3b-c were cut to decrease the network size and minimize network activity. Data were digitized at 6 kHz with a PCI-6042E board (National Instruments) using Stimulog software (courtesy of Prof. Zoltan Nusser, IEM, Budapest), and were analyzed off-line using the Evan software.

V.4. Electrophysiological characterization and clustering of cell types

Before recording synaptic currents, we tested the voltage response of recorded cells in current-clamp configuration at holding potential of -65 mV to a series of hyperpolarizing and depolarizing square current pulses of 800 ms duration and amplitudes between -100 and + 100 pA at 10 pA step intervals, then up to 300 pA at 50 pA step intervals and finally up to 600 pA at 100 pA step intervals [injected currents, in pA: 10, -10, 20, -20, 30, -30, 40, -40, 50, -50, 60, -60, 70, -70, 80, -80, 90, -90, 100, -100, 150, 200, 250, 300, 400, 500, 600].

Recorded traces from each neuron were then subjected to analysis in MATLAB using a script written by Márton Rózsa (Research Group for Cortical Microcircuits of the Hungarian Academy of Sciences, Szeged, Hungary) and modified by Szabolcs Káli. The script extracted a collection of 40 features, which characterized the subthreshold and suprathreshold dynamics of the membrane potential during hyperpolarizing and depolarizing current injections, and included features such as input resistance, membrane time constant, the amplitude of the sag response to hyper- polarizing inputs, the properties of single action potentials (amplitude, width, after-hyperpolarization) and spike trains (maximal frequency, accommodation, etc.). To reveal potential clustering among the recorded cells in terms of their physiological characteristics, we first performed principal component analysis on the extracted features, and kept only those principal components that contributed substantially to the variance (solutions involving different numbers of principal components were tested in several cases). We then carried out hierarchical clustering on the lower dimensional data formed by the selected principal components of the data, using the Euclidian distance measure and Ward's linkage method.

V.5. Post hoc anatomical identification of interneurons

The recorded cells were filled with 0.2% biocytin. After the recording, slices were fixed in 4% paraformaldehyde in 0.1 M phosphate buffer (pH 7.4) for at least 3 h. The fixation was followed by washout with phosphate buffer several times. The sections were blocked with normal goat serum (10%, Vector Laboratories, Burlingame, CA, USA) diluted in Tris-buffered saline (TBS) (pH 7.4). Biocytin was visualized by Alexa Fluor 488-conjugated streptavidin (dilution 1:3000; Molecular Probes, Vienna, Austria). Sections were mounted on slides in Vectashield (Vector Laboratories). To separate PV +

BCs from AACs, slices were re-sectioned to 40 μ m thickness and processed for immunofluorescence double-labeling. Ankyrin G-immunostaining was applied together with biocytin visualization: slices were treated with 0.2 mg/ml pepsin (Cat. No.: S3002; Dako) in 0.2 M HCl at 37°C for 5 min and were washed in 0.1 M PB. Sections were blocked in normal goat serum (NGS, 10%) made up in Tris-buffered saline (TBS, pH=7.4) followed by incubations in mouse anti-Ankyrin G (1:100, Santa Cruz Biotechnology) diluted in TBS containing 2% NGS and 0.3% Triton X-100. Following several washes in TBS, Cy3 conjugated goat anti-mouse(1:500, Jackson) was used to visualize the immunoreactions, and Alexa488 conjugated strepavidin (1:500; Molecular Probes) to visualize the biocytin. Sections were then mounted on slides in Vectashield (Vector Laboratories) (Gulyás et al. 2010). To investigate the probability of physiological connections between PV + and CCK + cells, transgenic mice expressing eGFP controlled by PV promoter (Meyer et al. 2002) were used. To identify CCK + cells, biocytin was visualized by Alexa Fluor 488-conjugated streptavidin (as described above), and then slices were blocked in normal donkey serum (10%; Vector Laboratories) diluted in TBS (pH 7.4), followed by incubation in rabbit anti-CB 1 (Cayman Chemical Company, Ann Arbor, MI, USA) diluted 1:1000 in TBS containing 1% normal donkey serum and 0.05 % Triton X-100. After several washes in TBS, CB_1 expression was visualized using Alexa Fluor 594 (donkey anti-rabbit, dilution 1:500; Invitrogen, Carlsbad, CA, USA) and then the incubation was followed by several washes in TBS. Sections were mounted on slides with Vectashield (Vector Laboratories). Images were acquired using an FV1000 confocal microscope (Olympus) with either a 20 × or a 60 × oil-immersion objective. Only presynaptic cells with preserved axonal arborization were included in the study. CB_1-expressing, non-fast-spiking interneurons were identified as CCK+ cells (Katona et al. 1999).

V.6. Modeling the short-term plasticity of inhibitory synapses

To characterize effectively the temporal properties of transmission measured at different frequencies and patterns we attempted to fit our experimental data on the short-term depression and recovery of inhibitory synaptic transmission using several different models. The first model was proposed by Tsodyks et al. (1998):

DOI:10.14753/SE.2018.2077

$$\frac{dn(t)}{dt} = \frac{1 - n(t)}{\tau_r} - \sum_j \delta(t - t_j) \cdot p \cdot n(t) \quad (1)$$

where *n(t)* is the proportion of available resources at the synapse at time *t*, τ_r is the rate at which these resources are replenished in the absence of a presynaptic action potential, *p* is the fraction of available resources used by an action potential, t_j denotes the time of the j'th presynaptic spike, and $\delta(t)$ is Dirac's delta function. It is also possible to describe synaptic facilitation using this model by making *p* itself depend on presynaptic activity:

$$\frac{dp(t)}{dt} = \frac{p_0 - p(t)}{\tau_f} - \sum_j \delta(t - t_j) \cdot p_0 \cdot (1 - p(t)) \quad (2)$$

where p_0 is the baseline value of *p*, and τ_f is the time constant of facilitation.

While this first model assumes that the rate at which synaptic resources are replenished is constant, a later modification of the model (Hennig, 2013; Wang and Kaczmarek, 1998) assumes (based on experimental data) that the rate of replenishment itself depends on presynaptic activity, and is described by the following set of equations:

$$\frac{dn(t)}{dt} = \left(k_r + \tilde{k}_e k_e(t)\right)\left(1 - n(t)\right) - \sum_j \delta(t - t_j) \cdot p \cdot n(t) \quad (3)$$

where k_r is the baseline rate of replenishment, and $\tilde{k}_e$ is the relative maximum weight of activity-dependent replenishment. $k_e(t)$ describes the time dependence of this term, and evolves as

$$\frac{dk_e(t)}{dt} = -\frac{k_e(t)}{\tau_e} + a_e \cdot \sum_j \delta(t - t_j) \cdot (1 - k_e(t)) \quad (4)$$

where a_e is the fraction by which the rate of activity-dependent replenishment increases following each spike, and τ_e is the time constant with which this rate returns to its baseline value.

In all of these cases, the mean amplitude of the postsynaptic current following the j'th presynaptic action potential can be calculated as

$$PSC_j = A \cdot n(t_j) \cdot p(t_j) \quad (5)$$

where A is the nominal maximum value of the current, and all variables are evaluated directly before the spike. We assume $n = 1$ and $p = p_0$ before the first spike.

The above equations actually define four different variants of the resource depletion model of short-term synaptic plasticity (with or without facilitation, and with a constant or a use-dependent rate of replenishment). Since these models contain different numbers of free parameters (between 2 and 6), comparing them purely based on the goodness of fit can be misleading. We therefore also calculated for both models the measure known as the Bayesian Information Criterion, which penalizes fits with more free parameters, and used the Bayesian Information Criterion scores for model comparison.

V.7. Asynchronous charge calculation

For CCK+ cells the later phase of longer spike trains often evoked asynchronous IPSCs. To characterize the contribution of asynchronous release to synaptic transmission, the total asynchronous charge was calculated using a program written by Daniel Gemes (Faculty of Information Technology, Pázmány Péter Catholic University, Budapest, Hungary), as the difference between the area under the mean curve during the stimulation including an additional 500 ms long time interval after the end of the 10th action potential, and the area under the mean curve during an interval of the same length at least 500 ms after the stimulation. To calculate immediate and delayed asynchronous release, an artificial reconstructed trace was created. This involved first fitting to the average of all 11th (single) IPSCs a waveform defined as the difference of two exponentials, described by the following equation:

$$I(t) = A \cdot e^{-\frac{t}{\tau_r}} - A \cdot e^{-\frac{t}{\tau_d}} + B \quad (6)$$

where A is the amplitude, τ_r and τ_d are the time constants for the rising and decaying phases of IPSC, respectively, and B is the baseline value of the current. The synaptic delay was also determined from these data as the difference between the start of the rising phase of the IPSC and the time of the presynaptic stimulation. Subsequently, current traces during stimulation trains were fit by sequentially adding IPSC templates whose timing was determined by the times of the presynaptic spikes (plus the measured

delay), and whose amplitudes were scaled to the amplitude of the corresponding averaged IPSCs.

Asynchronous charge was calculated as the difference of the low-pass filtered (100 Hz) original and reconstructed trace. The time window for immediate asynchronous charge calculation at each action potential was set as the time between 2 stimulations (200 ms at 5 Hz, 100 ms at 10 Hz, 50 ms at 20 Hz, 25 ms at 40 Hz, 12.5 ms at 80 Hz, 6.25 ms at 160 Hz, 3.125 ms at 320 Hz). Delayed asynchronous charge was calculated as the difference of low-pass filtered (100 Hz) original and artificial reconstructed trace in a 500 ms long time window after the end of stimulation.

V.8. Statistical analysis

In Part I of the results session data sets were not normally distributed according to Shapiro-Wilk W test. Mann-Whitney U-test was used to compare the amplitude, duration and underlying multiunit activity of sharp wave-ripples and interictal-like events, as well as to compare the time interval separating them. The spiking probability and changes in firing rate between different phases of interictal-like events were compared by Wilcoxon paired test. The baseline membrane potential of cell groups between interictal-like events was compared by Kruskal-Wallis ANOVA. The depolarization of cells reached during interictal-like events was compared by Mann-Whitney U-test. The amplitude of stimulation-evoked excitatory and inhibitory postsynaptic currents and the amplitude of inhibitory postsynaptic currents at cells pairs in control condition and in the presence of high K^+ was compared by Wilcoxon paired test.

In Part II of the results session data sets were not normally distributed according to Shapiro-Wilk W test. Consequently, data from multiple groups were compared via the non-parametric Kruskal–Wallis ANOVA test, and post hoc paired comparisons were carried out using the Bonferroni-corrected Mann–Whitney U test. The data reported in table form are given as the median (with the first and third quartiles in parenthesis), whereas data shown in figures represent the median values. The dependence of connection probabilities on pre- and/or postsynaptic cell type was determined using Pearson's chi-squared test.

DOI:10.14753/SE.2018.2077

VI. RESULTS

VI.1. Physiological sharp wave-ripples and pathological interictal-like events are different forms of transient high activity events in the CA3 region of hippocampus

In the first part of this thesis we addressed the question what are the differences between physiological and pathological activities generated intrinsically in the CA3 region of mouse hippocampus. To this end, we induced transition from sharp wave-ripples to interictal-like events, and investigated the changes of network dynamics between the different activity states. On the cellular level, we examined the output properties of identified pyramidal cells and different types of interneurons, and determined the changes of excitatory and inhibitory transmission by electrical stimulation and by performing paired recording between monosynaptically connected interneurons and their pyramidal cell targets. To mimic the ongoing hippocampal activity presynaptic cells were stimulated by a train of action potentials similar to output properties of interneurons during interictal-like events.

VI.1.1. Induction of transition from sharp wave-ripple to epileptiform events generating state

Increase in the extracellular potassium concentration is a well-established and widely distributed model of epilepsy (Frohlich et al., 2007). Thus, we could evoke transitions from sharp wave-ripple (SWR) to epileptiform activity generating state by increasing the concentration of extracellular potassium from 3.5 mM to 8.5 mM in aCSF (n = 86). The elevation of extracellular potassium gradually eliminated spontaneous SWRs and evoked a transitory phase characterized by asynchronous EEG activity, and was followed by a state generating recurring epileptiform events (Figure 7A). We defined epileptiform events as high amplitude interictal-like events (IIE) accompanied by high multiunit activity. We also observed epileptiform events in other models: by blocking voltage-gated K^+ channels by 30 μM 4-aminopyridine (n = 8), by blocking $GABA_A$ receptors by 2 μM GABAzine (n = 23) and by enhancing NMDA type glutamate receptor function by 0 Mg^{2+} ACSF (n = 19) (Figure 7B). In all four models SWRs were separated

DOI:10.14753/SE.2018.2077

from epileptiform events by transitory phase, during which the multi-unit activity broke down and reorganized into epileptiform events.

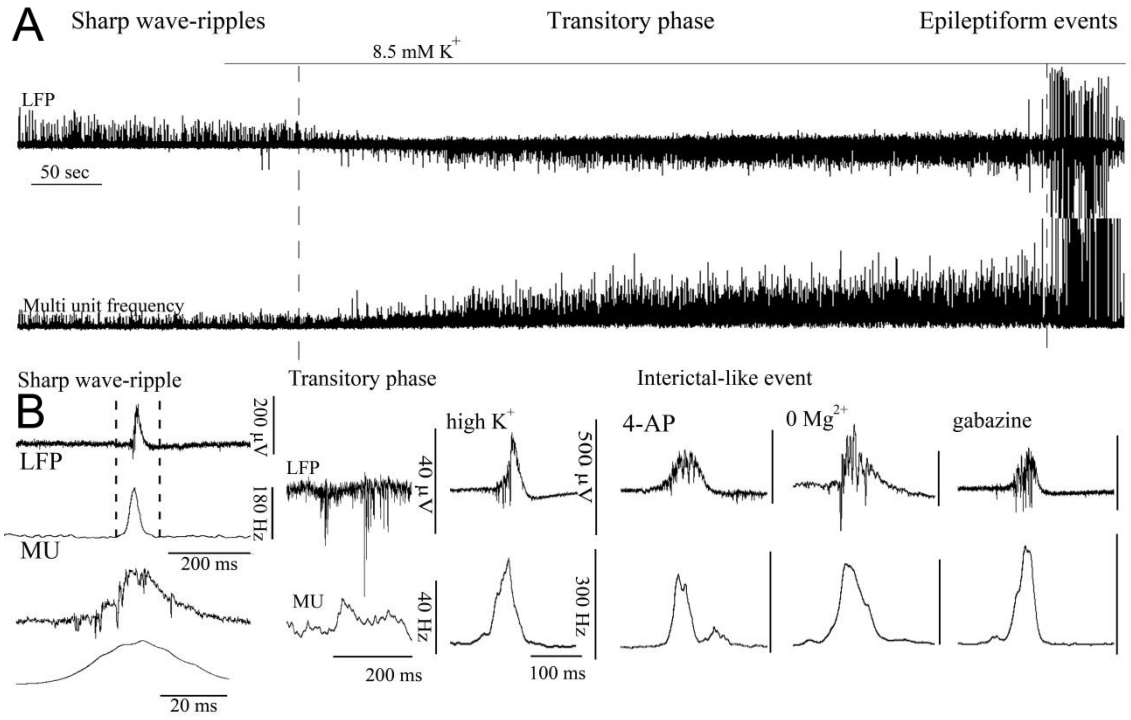

Figure 7. Transition from sharp wave-ripples to epileptiform events in vitro. *A: Epileptiform events were induced by elevating the concentration of extracellular K^+ from 3.5 mM to 8.5 mM. Sharp wave-ripples and epileptiform events are separated by transitory phase characterized by highly active, but featureless asynchronous multiunit activity. Note that an increase of multi-unit frequency precedes epileptiform events. Upper trace: local field potential (LFP) recorded in the CA3c region of 450 µm thick hippocampal slices. Lower trace: plot of multi-unit frequency demonstrating network activity during transition from sharp wave-ripple generating state to epileptiform event generating state. B: Enlarged image of sharp wave-ripple and accompanying multi-unit activity at 200 ms (top) and 20 ms (bottom) time scale, as well as transitory phase and interictal-like events and underlying multi-unit activity (MUA) triggered by 8.5 mM K^+, 30 µM 4-aminopyridine, 0 Mg^{2+} containing ACSF or 2 µM GABAzine.*

IIEs were observed in all four models, and evolved into more persistent, late preictal-like and ictal-like events (Figure 8). The appearance of preictal-like events was preceded by a negative peak in LFP (with a robust increase of multi-unit activity), followed by 1-5 smaller events with negative deflection and a consequent large positive peak. They were less frequent compared than IIEs (8.5 mM K^+, n=48; 30 µM 4-aminopyridine, n=8; 0 Mg^{2+}; n= 9, 2 µM GABAzine, n=14), and were characterized by

large amplitude of 3300 μV (1187, 4000), duration of 465 ms (335, 793) and recurrence of 1400 ms (637, 7750). Ictal-like events were seen in a moderate number of slices (mostly in the 0 Mg^{2+} model, n=10; in the presence of 2 μM GABAzine, n=5; and once in the presence of 8.5 mM K^{+}). They manifested as successive large amplitude positive and negative deflections (amplitude: 3500 μV (2200, 4000); duration: 6500 ms (1537, 8000); recurrence: 19000 ms (8200, 25475)), with peaks separated by less than 150 ms. The entire ictal-like event never lasted more than 1500 ms, and were always accompanied by an increase in multi-unit activity (2.5-fold larger than during SWRs).

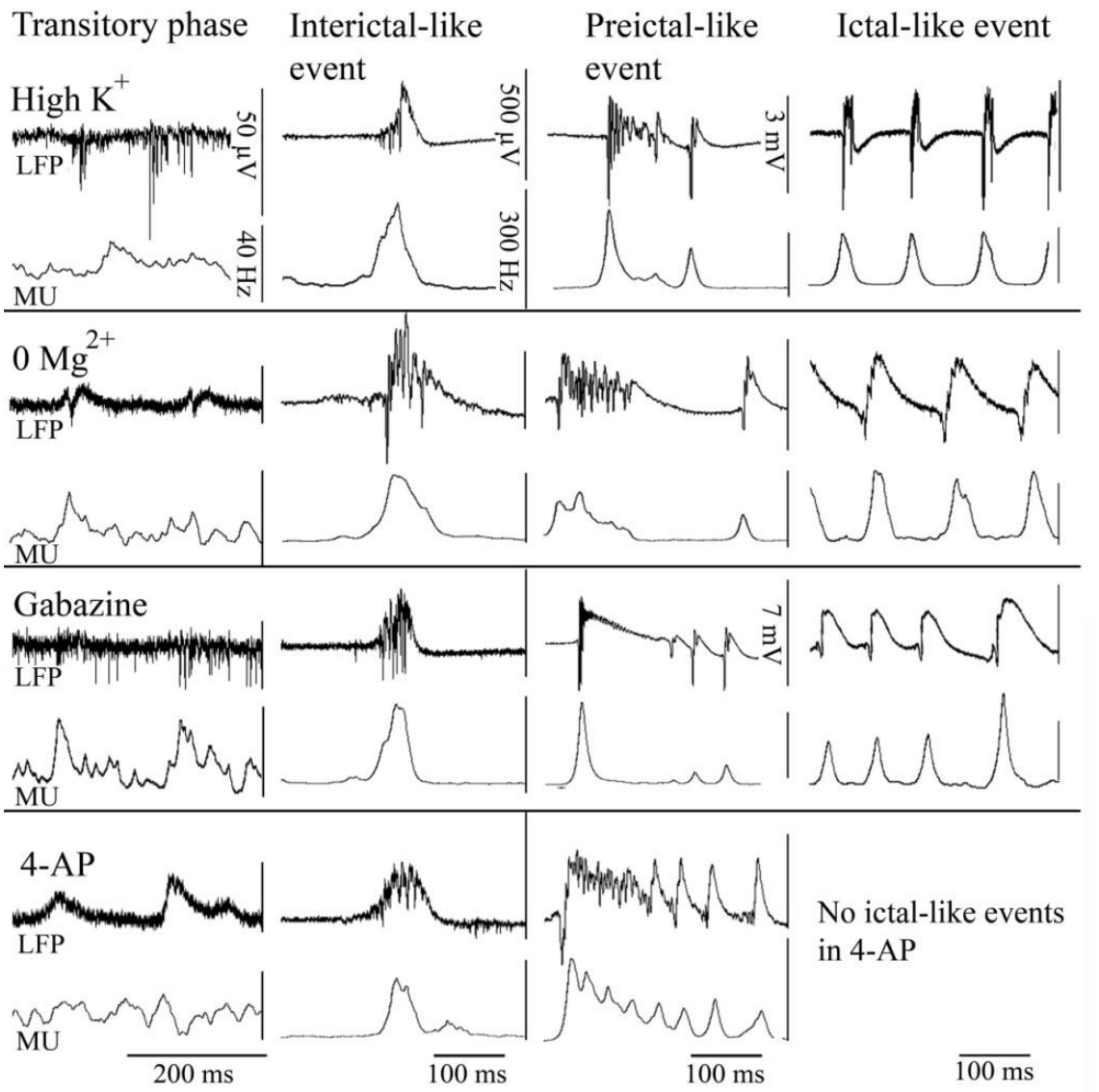

Figure 8. Early interictal-like events evolve into late preictal-like and ictal-like events. *Epileptiform events induced by elevating extracellular K^{+} concentration, omitting Mg^{2+} from ACSF, blocking $GABA_A$ receptors by 2 μM GABAzine, or adding the K^{+} channel blocker 4-aminopyridine (30 μM) to the*

extracellular solution. In all cases, after a transitory period, characterized by low synchrony and high activity (first column), highly synchronous epileptiform events appeared (3 subsequent columns on the right). The amplitude and complexity of epileptiform events vary among different models, however, phenomenologically similar events occurred with the four pharmacological interventions: interictal-like events evolved into late preictal- and ictal-like events.

After demonstrating that we can successfully induce transition from SWR to epileptiform event generating state, we asked which network and cellular mechanisms are responsible for this transition in the high potassium model of epilepsy..

VI.1.2. Sharp wave-ripples and high K+ induced interictal-like events are different transient high activities

First, we analyzed the occurrence of SWRs and IIEs in a large set of slices. We found that slices generating frequent and large amplitude SWRs produced either small amplitude or no IIEs in the presence of high K^+. On the other hand, slices with infrequent, small amplitude or no SWRs were more likely to generated large amplitude IIEs. The regression analysis showed negative correlation between the amplitude/presence of these events (Figure 9A) indicating, that the capability of hippocampal slices to generate either SWRs or IIEs is likely to be inversely related. Moreover, SWRs and IIEs never appeared interleaved, they were separated by the transitory phase (median duration in s: 315 (179-459)) (Figure 9B) supporting the notion, that they are different network phenomena.

Although we could not find difference in the current-source density picture of SWRs (Figure 9C) and IIEs (Figure 9D), a significant difference was found in the amplitude of the two event types: 135 uV (124.9, 141.1) for SWRs and 640 uV (612, 692) for IIEs (Mann-Whitney U-test, $P = 0.014$). They also could be separated based on their duration: SWRs lasted 46 ms (42.2, 57.4), whilst the duration of IIEs was 129 ms (104, 157) (Mann-Whitney U-test, $P = 0.008$). We also found significant difference in the time interval separating SWRs (637 ms (338, 813)) and IIEs (1112 ms (862, 1976)) (Mann-Whintey U-test, $P = 0.02$). Finally, a significant difference was found in the underlying multiunit activity: 170 Hz (150, 190) for SWRs and 305 Hz (233, 466) for IIEs, respectively (Mann-Whitney U-test, $P < 0.001$).

DOI:10.14753/SE.2018.2077

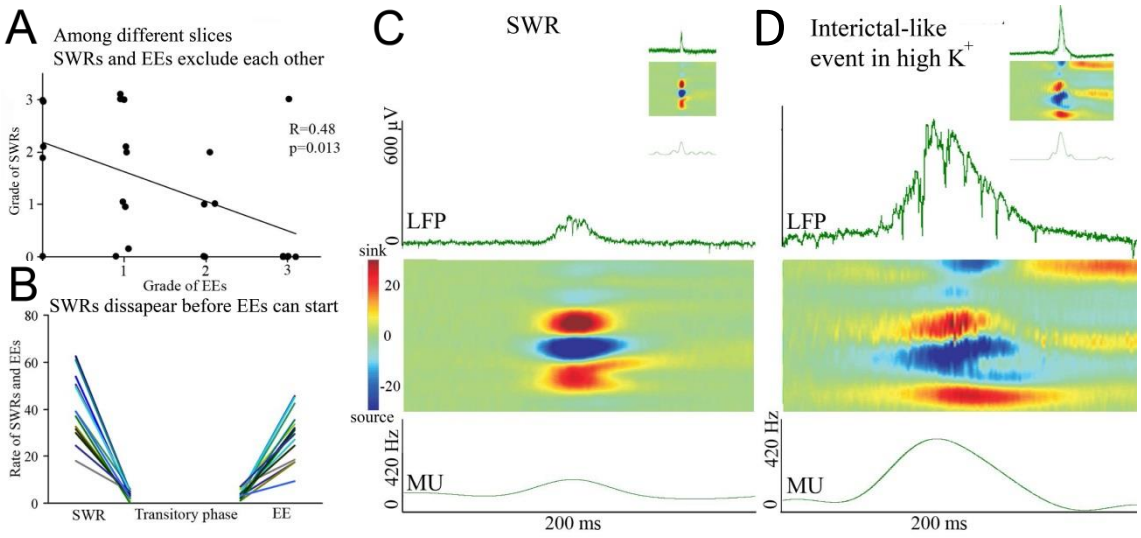

Figure 9. Sharp wave-ripples and interictal-like events are different high activity events and exclude each other. *A: Sharp wave-ripples (SWRs) and epileptiform events (EEs) are plotted to compare their correlation. There is a negative correlation in the rate of amplitude of the two events types (n=26). B: The rate of SWRs and EEs at SWR-generating, transitory and EE-generating state. During control conditions (ACSF containing 3.5 mM K^+) the rate of SWRs is high (the rate of EEs is zero), but it disappears during the transitory phase (the rate of SWRs and EEs is zero). In the EE-generating state the rate of IIEs is increasing, whilst SWRs remain zero. Analysis of current-source densities of SWRs (C) and IIEs (D) showed only a minor shift in the organization of sinks (red) and sources (blue), however, IIEs have a larger amplitude, longer duration and are accompanied by several-fold higher multi-unit activity compared to SWRs.*

VI.1.3. Rearrangement of synchrony during the transitory phase separates sharp wave-ripples from interictal-like events

After describing the basic differences between spontaneous SWRs and high K^+ induced IIEs we asked, how the network becomes desynchronized and transforms into IIE generating state. As it is shown on Figure 10A-B, multi-unit activity was characterized by highly synchronous transient burst during both events. However, during the transitory phase, multi-unit activity became asynchronous characterized by featureless EEG activity, and reorganized into a new, highly active synchronous phase (IIEs) after a certain time (538 s (313, 560)).

DOI:10.14753/SE.2018.2077

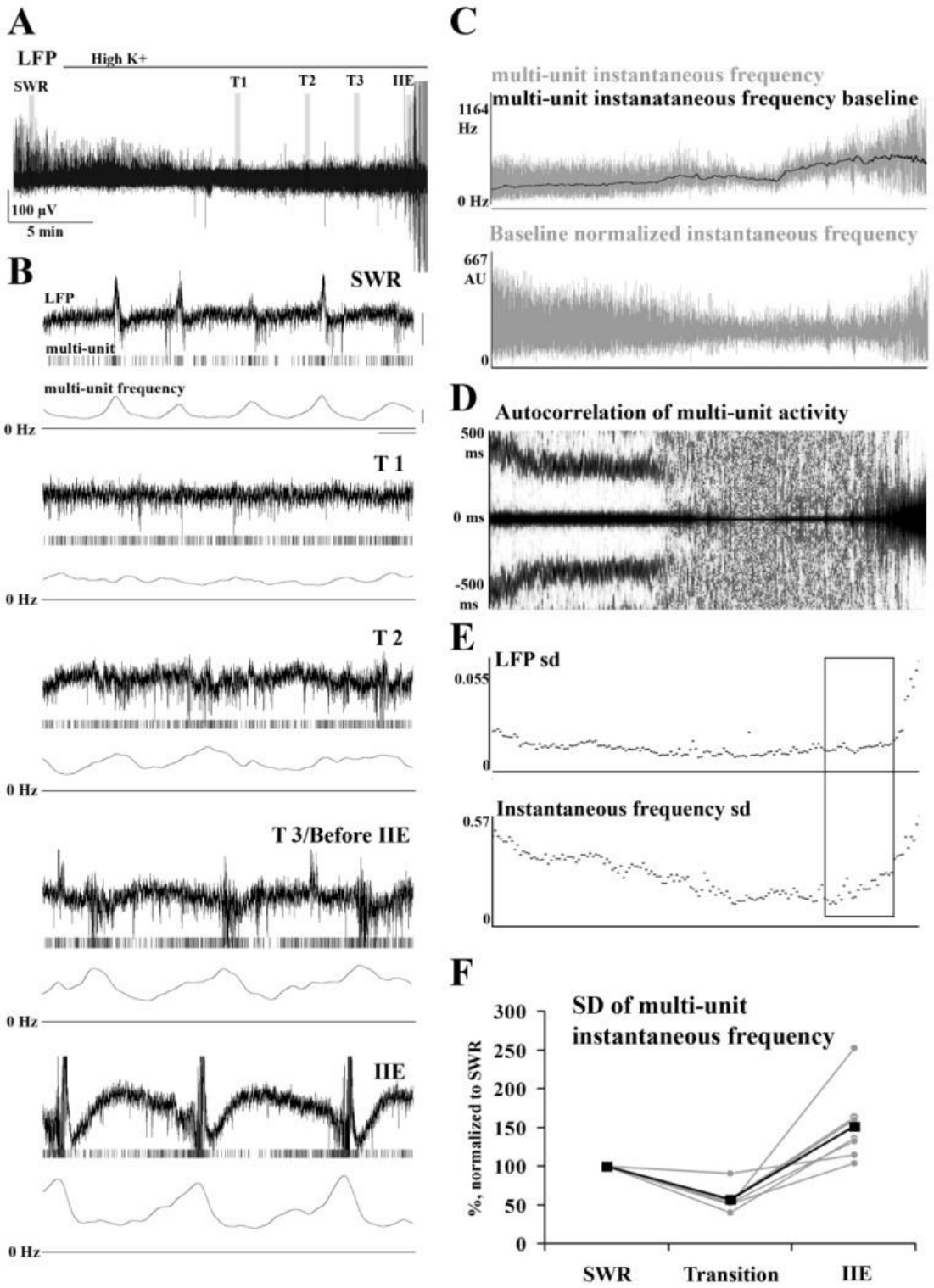

Figure 10. Reorganization of synchrony higk K^+ model od epilepsy. *A: Local field potential (LFP) during the transitory phase in the presence of 8.5 mM K^+. Gray areas (SWR – sharp wave ripple; T1, T2, T3 – different phases of transition, IIE – interictal-like events) indicate different phases of transition, and are magnified in B. Note, that during transition the synchrony of multi-unit activity drops, but builds up during*

IIE generating state. The raster plots of multi-unit activity and multi-unit frequency are shown below the local field potential. Scale bars: upper = 100 μV, lower = 60 Hz, time scale = 500 ms. C: Multi-unit frequency (upper trace, gray) and its low-pass filtered baseline (black) increased during the transition between the two states. Lower panel: baseline-normalized instantaneous frequency fluctuation of multi-unit activity. D: Time-binned autocorrelogram of multi-unit activity. The synchrony of multi-unit firing during SWRs reorganizes into a different synchrony during IIEs. E: A decrease and gradual recovery can be seen in the standard deviation (SD) of the local field potential and instantaneous multi-unit frequency. The elevation of SD of local field potential is preceded by the elevation of SD of multi-unit frequency in the IIEs generating state (framed area). F: Changes of SD during SWRs, transition and IIEs (n=6).

To visualize multi-unit frequency fluctuation without the systematic increase in the baseline frequency, we calculated the instantaneous frequency of multi-unit firing and normalized to its low-pass filtered average (Figure 10C). This measure shows how the firing exceeds baseline activity during the synchronous bursts. We found, that the local minima and maxima of the multi-unit firing frequency showed large differences during SWRs and IIEs, but approached each other during the transitory period suggesting a steady, elevated, but less structured activity. The time-binned autocorrelogram of multi-unit activity also supported the finding: the synchrony during SWRs was eliminated during transitory period and reorganized into a different synchrony during IIEs (Figure 4D). We also plotted the standard deviation of the local field potential and multi-unit instantaneous frequency (Figure 10E). During SWRs, the values of standard deviation were relatively high and stable, but dropped during the transitory phase and build up again during IIEs with higher values than during SWRs. However, in the epileptiform activity generating state the standard deviation of multi-unit frequency started to increase several minutes earlier compared to the standard deviation of local field potential (Figure 10F).

VI.1.4. Identification of different classes of CA3 neurons

To uncover the spiking behavior and the synaptic inputs of distinct types of neurons in CA3 during SWRs and high K^+ induced IIEs, we recorded the firing properties of individual cell types together with local field potential (LFP). Subsequently, excitatory and inhibitory postsynaptic currents (EPSCs and IPSCs) were measured in whole-cell mode. During recording, cells were filled with biocytin and visualized *post hoc* using Alexa Fluor 488 conjugated streptavidin. Based on the dendritic and axonal arborization,

DOI:10.14753/SE.2018.2077

recorded neurons were grouped into five anatomical types. The somata of PV+ basket cells (PV+ BCs) and axo-axonic cells (AACs) were located in strata pyramidale, oriens and lucidum, with dendrites seen in all layers. The axon arbor of PV+ BCs was predominantly in stratum pyramidale (Figure 11A). By contrast, the axon arbor of AACs was shifted towards the border of strata pyramidale and oriens, where the axon initial segment (AIS) of most pyramidal cell (PC) is located (Figure 11B).

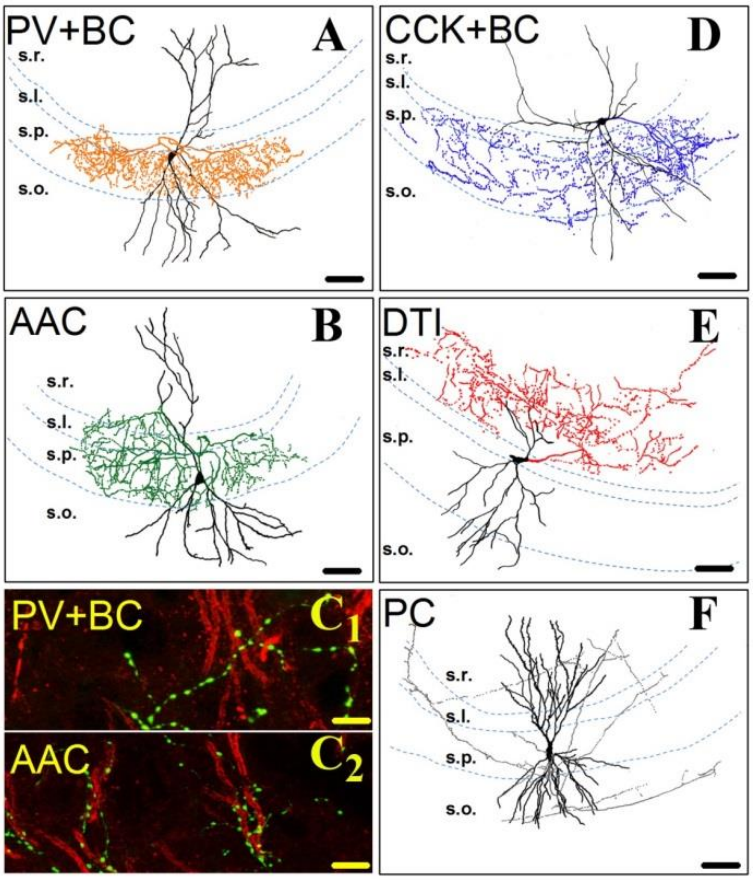

Figure 11. Morphological andimmuncytochemical identification of hippocampal neurons. *A-B, D-F: Camera lucida reconstruction of representative, biocytin-filled INs and PCs. Cell bodies and dendrites are shown in black, the axonal tree in orange (A, PV+ BC), green (B, AAC), blue (D, CCK+ BC), red (E, DTI) and grey (F, PC). C_{1-2}: To separate PV+ BCs from AACs, we selectively labeled the axon initial segment of PCs by ankyrin G. There is no association between the boutons of PV+ BCs (green) and the AIS of PCs (red) (C_1), whereas the bouton rows of AACs outline the AISs of PCs (C_2). Scale bar in A-B, D-F: 90 µm, scale bar in C_{1-2}: 10 µm.*

To separate PV+ BCs from AACs, we performed double-immunostaining for biocytin and ankyrin G (Gulyás *et al.*, 2010). Presynaptic interneurons were identified as PV+ BCs (n = 10) if there was no association between the axons of biocytin labeled boutons and ankyrin G stained AISs (Figure 11C_1). We classified cells as AACs (n = 6) when their boutons outlined the AISs (Figure 11C_2). The somata of CCK+ basket cells (CCK+ BCs, n = 5) and dendritic region-targeting interneurons (DTIs, n = 15) were located in strata lucidum, oriens, lucidum/radiatum border and upper stratum radiatum

with dendrites spanning all layers. Axon collaterals of CCK+ BCs ramified mostly in stratum pyramidale, although some axon collaterals could also be found in strata oriens and lucidum (Figure 11D). On the other hand, axon collaterals of DTIs ramified mainly in strata oriens, lucidum and radiatum (Figure 11E). The somata of pyramidal cells (PCs, n = 12) were located in stratum pyramidale. Their spiny dendrites and rarely branching axons occupied all CA3 layers (Figure 11F).

VI.1.5. Activity of identified CA3 neurons during sharp wave-ripples and interictal-like events

First, we examined the firing properties of identified CA3 neurons during SWRs and IIEs. Figure 12A-C shows that almost all recorded neuron types increased their firing rate during IIEs compared to SWRs. As the duration of IIEs was ~100 ms and the firing pattern of different neurons varied systematically during individual phases of IIEs, we defined three 100 ms phases where firing properties were analyzed: 100 ms before, 100 ms during and 100 ms after the IIEs.

The firing probability of PCs (n = 12) during SWRs was low, usually no spikes were detected. However, their firing probability significantly increased during IIEs, and we also observed spontaneous bursts of action potentials between IIEs. The firing rate of PCs varied significantly between different phases of IIEs (before, during, after), characterized by rise in the during phase and an immediate drop in the after phase (Figure 12B, Figure 13A, Table 1).

PV+ BCs (n = 10) and AACs (n = 6) were the most active cell types during SWRs, and increased their firing rate during the “before” phase of IIEs. However, when IIEs reached their peak (“during” phase), the majority of PV+ BCs and AACs dropped their firing, and the spike amplitude decreased gradually and continued until spiking was not detectable. In the “after” phase the spiking of PV+ BCs and AACs progressively recovered, and the spike number increased (Figure 12 and 13, Table 1).

DOI:10.14753/SE.2018.2077

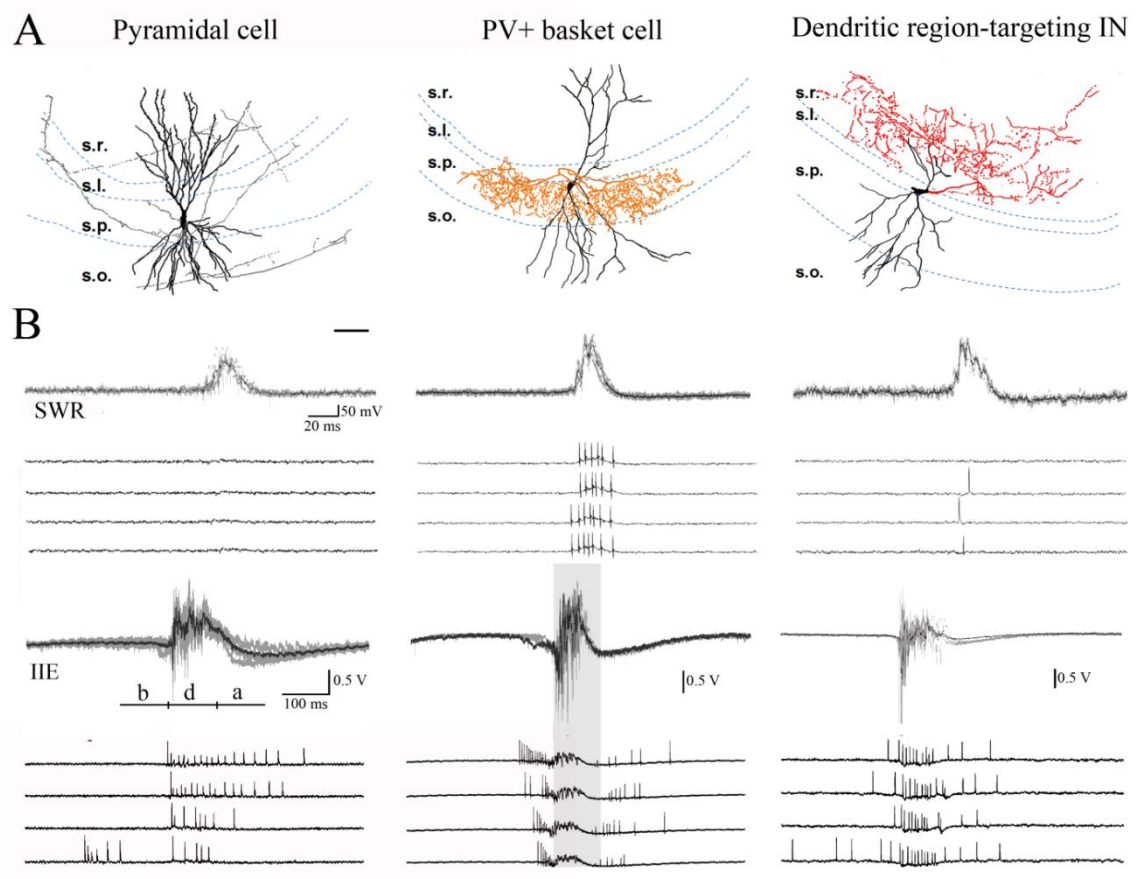

Figure 12. Hippocampal neurons increase their firing rate during interictal-like events, however, PV+ basket cells stop firing. *A: Firing of anatomically identified CA3 pyramidal cells, PV+ basket cells and dendritic region-targeting interneurons during sharp wave-ripples, recorded in loose-patch configuration. Scale bar: 90 μm. B: Firing of pyramidal cells, PV+ basket cells and dendritic region-targeting interneurons during high K^+ induced interictal-like events. All interneurons increased their firing rate, but some PV+ basket cells stopped firing at the peak of interictal-like events. The firing of CA3 neurons was separated into 3 phases: 100 ms before (a), 100 ms during (d) and 100 ms after the interictal-like events (a). Gray area shows the peak of interictal-like events, where PV+ basket cells stopped firing.*

The spiking probability of CCK+ BCs (n = 5) and DTIs (n = 15) was moderate during SWRs, but increased during IIEs. During “before phase”, CCK+ BCs and DTIs started to fire, continued to do so during the entire event (“during” phase), and decreased their firing in the “after” phase (Figure 12 and 13, Table 1).

DOI:10.14753/SE.2018.2077

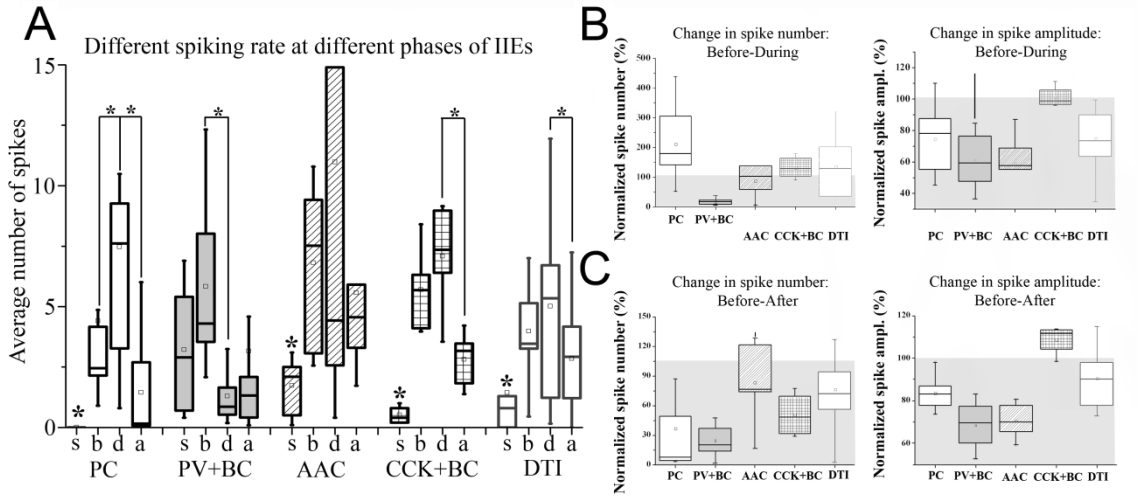

Figure 13. Firing rate varies among different phases of interictal-like events induced by high K^+. *A: Statistical comparison of the average number of spikes fired by pyramidal cells (PC), PV+ BCs, AACs, CCK+ BCs and DTIs during sharp wave-ripples (s), and in the "before" (b), "during"(d) and "after" (a) phase of interictal-like events. In all cases, the firing probability significantly increased from sharp wave-ripples to interictal-like events. The firing significantly varied among individual phases of interictal-like events. The significant differences are marked with asterisks. B: Changes in normalized firing probability and amplitude for different hippocampal CA3 neuron types. Values were normalized to the "before" phase (100 %) of interictal-like events. Upper graphs compare the changes between the "before" and "during" phase, whereas lower traces compare changes among the "before" and "after" phases. Gray area indicates a drop (less than 100%), asterisks indicate significance at $P < 0.05$. PC, pyramidal cell; PV+ BC, parvalbumin positive basket cell; AAC, axo-axonic cell; CCK+ BC, cholecystokinin positive basket cell; DTI, dendritic region-targeting interneuron.*

After analyzing the output properties of different cell types we also compared the normalized changes in firing rate between the individual phases of IIEs among neuron groups, where the 100% was the number of spikes fired in the "before" phase. First, we analyzed the changes between the "before" and "during" phase. We found, that in the "during" phase PV+ BC values were significantly smaller compared to PCs, CCK+ BCs and DTIs, and AAC values were significantly smaller then PC values. No other groups showed significant changes. The comparison of firing rate changes between "before" and "after" phases showed that PC and PV+ BC values were significantly smaller than AAC and DTI cell values (Figure 13B-C, Table 1).

Table 1: Spiking characteristics of different hippocampal CA3 neurons during sharp wave-ripples and different forms of interictal-like events. *Data are given as median and interquartile range in parenthesis. Numbers in bold are significant P-values (<0.05).*

	PC	**PV+ BC**	**AAC**	**CCK+ BC**	**DTI**
spike/SWR	0	2.9 (0.9;5.1)	2.1 (0.9; 2.5)	0.6 (0.2; 0.8)	0.8 (0.4; 1.8)
spike/IIE (entire)	11.8 (4.7; 11.6)	6.7 (7.7; 11.5)	12.8 (7.1; 18.6)	15.1 (11.5; 14.7)	11.7 (8.9; 15.9)
Wilcoxon test p values	**<0.001**	**0.038**	**0.008**	**0.03**	**<0.001**
Median number of APs across events in different phases					
APs "before" phase	2.5 (2.4; 4.9)	4.5 (3.5; 8.1)	7 (3.9; 8)	4.89 (4.1; 5.8)	3.69 (3.3; 5.3)
APs "during" phase	8.5 (4; 9.3)	0.76 (0.5; 1)	4.18 (2.6; 4.7)	6.88 (1.6; 5.7)	5.13 (0.6; 1.6)
APs "after" phase	0.17 (0.1; 4.2)	1.1 (0.4; 1.5)	3.74 (3.3; 5.4)	2.5 (1.7; 3.2)	3.1 (1.5; 4.2)
Change in firing rate					
"before" (100%) "to during"	211 (148.5; 325%)	12.5 (7.6; 23.9%)	100.4 (58.2; 36.2%)	129 (107; 154%)	129 (33.1; 200.1%)
"before" (100%) to "after"	6.7 (3.5; 8.9%)	36.81 (14.1; 37%)	76.6 (73.7; 121.8%)	47.9 (33.3; 65.1%)	69.1 (55.5; 93%)
"during" (100%) to "after"	4.3 (2.1; 7.7%)	223.4 (58; 421%)	89.5 (34.2; 126.6%)	41 (38.9; 46.9%)	62.9 (32.6; 99.7%)
Wilcoxon test p values					
"before" to "during"	**0.026**	**0.024**	0.68	0.29	0.4
"before" to "after"	**0.016**	**0.02**	0.5	0.13	**0.03**
"during" to "after"	**0.014**	**0.024**	0.92	**0.043**	0.42
Change in spike amplitude					
"before" (100%) to "during"	54.4% (66.7; 87.6)	65.3% (49.5; 75)	54.89% (54.9; 68.4)	98.5%(96.4; 103.1)	73.14% (63.9; 86.7)
"before" (100%) to "after"	78.4% (61.2; 86.3)	71.2%(61.2; 76.5)	66.94% (66; 76.4%)	111.6%(107;113.3%)	89.87% (77.4; 98%)
"during" (100^%) to "after"	109.8% (76.5; 112)	109.1% (102; 129)	125.9 %(109; 138.6)	106% (102; 117.4)	116.1% (103; 128.5)
Wilcoxon test p values					
"before" to "during"	**0.009**	**0.005**	**0.043**	1	**0.004**
"before" to "after"	**0.018**	**0.005**	**0.028**	0.144	**0.012**
"during" to "after"	0.57	**0.05**	**0.075**	**0.043**	**0.004**

Next, we analyzed the evolution of extracellular spike amplitude. Although only PV+ BCs and one AAC decreased their firing amplitude to zero, all neuron types showed decreased spike amplitude in the "during" phase of IIEs. When we normalized the amplitude of detected extracellular spikes (100% was the spike amplitude in the "before" phase) for all five neuron groups, we found significant decrease of spike amplitude for PCs, PV+ BCs, AACs and DTIs in the "during" phase compared to "before" phase. However, CCK+ BCs showed significant difference only when comparing the "during" phase to the "after" phase. The changes in normalized spike amplitudes were also compared among neuron groups. The spike amplitude values of PV+ BCs and AACs were

significantly smaller compared to CCK+ BCs and DTIs. Moreover, we found significant difference between the values of CCK+ BCs and DTIs (Figure 13B-C, Table 1).

VI.1.6. Membrane potential changes of hippocampal CA3 neurons during interictal-like events

We have shown that the amplitude of extracellular spikes decreased during IIEs, moreover, PV+ BCs (and one AAC) stopped firing. These results suggest that hippocampal neurons may receive a strong depolarization and some interneurons (PV+ BCs) would enter into depolarization block. To test this hypothesis, we recorded hippocampal neurons in whole-cell current clamp configuration simultaneously with LFP recordings. First, we compared the firing pattern observed with loose-patch and whole-cell current clamp configuration at different membrane potentials. The best matched firing between loose-patch and whole-cell current clamp recording was when neurons were held at membrane potential between -30 and -45 mV (similar to resting membrane potential of neurons in 8.5 mM K^+, Figure 14, Table 2). We also calculated the approximate depolarization caused by elevated potassium concentration (from 3.5 mM to 8.5 mM), which resulted in a depolarization of ~23 mV.

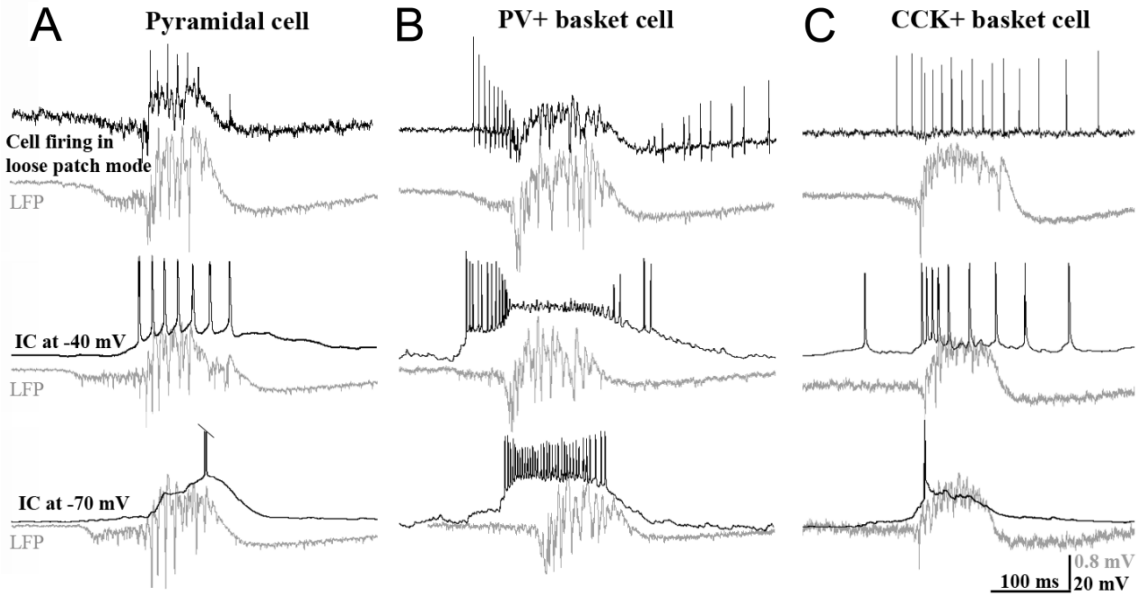

Figure 14. The firing of PV+ BCs stopped during interictal-like events as a result of strong depolarization. *A-C: The loose-patch recorded spiking of neurons matches the firing pattern recorded in whole-cell current clamp configuration at -40 mV (similar to resting membrane potential) during IIEs in 8.5 mM K^+. At this membrane potential, PV+ BCs stopped firing (upper trace: loose-patch configuration,*

middle trace: whole-cell current clamp configuration at -40 mV) (B). However, when the membrane potential was hyperpolrazied to -70 mV (lower trace), the firing probability of PV+ BCs increased, whilst the firing probability of other cell types (A and C) decreased.

Although we did not find significant difference in the baseline membrane potential of cell groups between IIEs (P = 0.46, Kruskal-Wallis ANOVA), during IIEs the membrane potential of all recorded cells depolarized and the amplitude of this deflection varied among neurons groups (Table 2).

Table 2: Membrane potential characteristics of CA3 neurons during the high K+ induced epileptiform event generating state.

	PC	PV+ BC	AAC	CCK+ BC	DTI
Membrane potential at I=0 between interictal-like events (mV)					
	-30.8 (-32; -30.3)	-39.7 (-40.2; -39.6)	-45.1 (-45.3; -43)	-41.8 (-42.5; -40.9)	-29.7 (-30.4;-29.1)
Membrane potential at IIE peak (mV)					
	-13.1 (-15.4; -11.9)	-17.6 (-19.9; 0)	-19.9 (-20.2; -15.2)	-29.9 (-33.8; -29.1)	-28 (-29.1; -27.8)
Membrane potential at the highest firing probability (mV)					
	-35.1 (-36.4; -33.8)	-40.4 (-45.1; -29.8)	-40.4 (-45.2; -40.2)	-44.8 (-45.1; -42.3)	-30.4 (-32.8; -30.1)

To calculate the level of this depolarization, we compared the maximum of the low-pass-filtered (30 Hz) membrane potential that cells reached during IIE peaks. We found that PCs and PV+ BCs received the largest depolarization. However, only PV+ BC depolarization differed significantly from the depolarization of CCK+ BCs (P = 0.037, Mann-Whitney U-test) and DTIs (0.036, Mann-Whitney U-test) (Figure 15A). These results indicate that the strong depolarization received by PV+ BCs can be a factor determining the depolarization block of PV+ BCs.

DOI:10.14753/SE.2018.2077

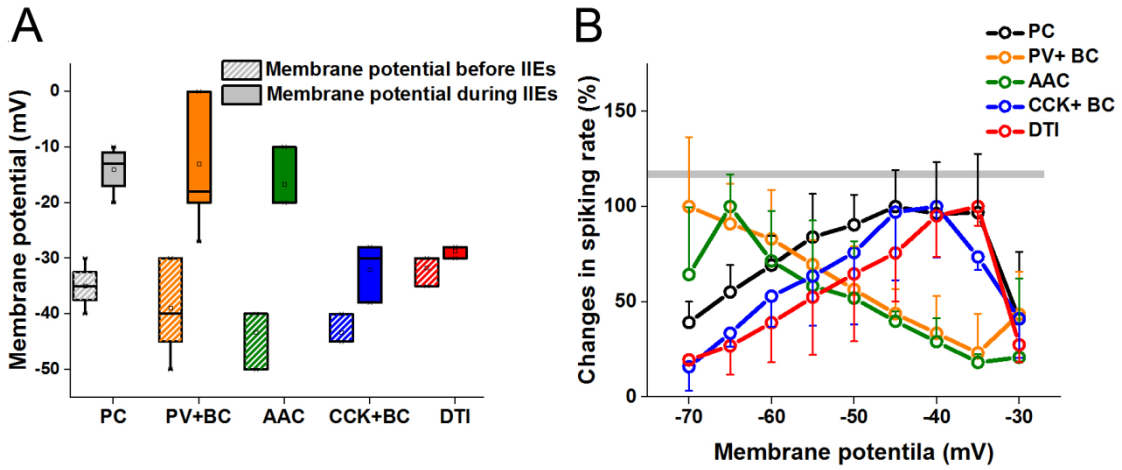

Figure 15. PV+ BCs enter into depolarization block during interictal-like events. *A: The membrane potential of different neuron groups before (stripped box) and during (filled box) IIEs (recorded in current-clamp configuration). Note, that the depolarization of neurons during IIEs was higher compared to former time points. B: Changes of firing probability of different neurons as a function of membrane potential (depolarization). Membrane potential-dependent changes were normalized to the peak firing rate of individual neurons. Grey line indicates 100 % (maximal) firing. The highest firing rate of PV+ BCs and AACs was close to the control membrane potential (from -70 to -60 mV). Other neurons increased their firing rate with increasing depolarization.*

We also determined the firing characteristics of all neuron types at different depolarization levels. Therefore, neurons were recorded in whole-cell current clamp configuration at membrane potentials from -70 to -30 mV (in 5 mV steps, Figure 15B) and the number of action potentials was compared between different neuron types and different membrane potentials. We found, that PCs, CCK+ BCs and DTIs fired with the lowest firing probability at – 70 mV compared to the firing observed in loose-patch configuration (when the membrane potential was around -40 to -45 mV). However, when we gradually depolarized cells in 5 mV steps, their firing frequency increased during IIEs. On the other hand, the maximal firing probability of PV+ BCs and AACs was observed at -70 mV and decreased with the increasing membrane potential. Moreover, when the depolarization of PV+ BCs reached -45 mV, they entered into depolarization block during IIEs (similar to results observed in loose-patch recording).

DOI:10.14753/SE.2018.2077

VI.1.7. Stages of interictal-like events correlate with intracellular potentials of hippocampal neurons

As the firing of neuron groups recorded in loose-patch configuration correlated closely with different phases of IIEs, we analyzed in detail the correlation between the local field potential and the relative timing of the firing of different cell types in current-clamp configuration without current injection (I = 0). We found four characteristic phases of IIE evolution (Figure 16):

(I) The first phase of IIEs was associated with a mild negative deflection of the local field potential, small depolarization of pyramidal cells and increased firing of PV+ BCs. The multi-unit activity started to increase.

(II) During the second phase, the steep negative shift of local field potential was associated with pronounced increase of PC depolarization and a steep depolarization of PV+ BCs characterized by accelerated firing and decreased action potential amplitude. The multi-unit activity increased further.

(III) In the third phase, PV+ BCs stopped firing, whilst PCs started to fire multiple action potentials. After an initial increase, the multi-unit activity and PC firing started to drop.

(IV) The fourth phase was characterized by the slow recovery of local field potential to the baseline value, accompanied by gradual recovery of PV+ BC firing and repolarization of PCs to a baseline membrane potential. The multi-unit activity also returned to baseline.

We have shown that the firing pattern of neurons become altered during different phases of interictal-like events. This can be the result of either changes in cellular parameters responsible for signal integration, or alterations in the excitatory or/and inhibitory transmission.

DOI:10.14753/SE.2018.2077

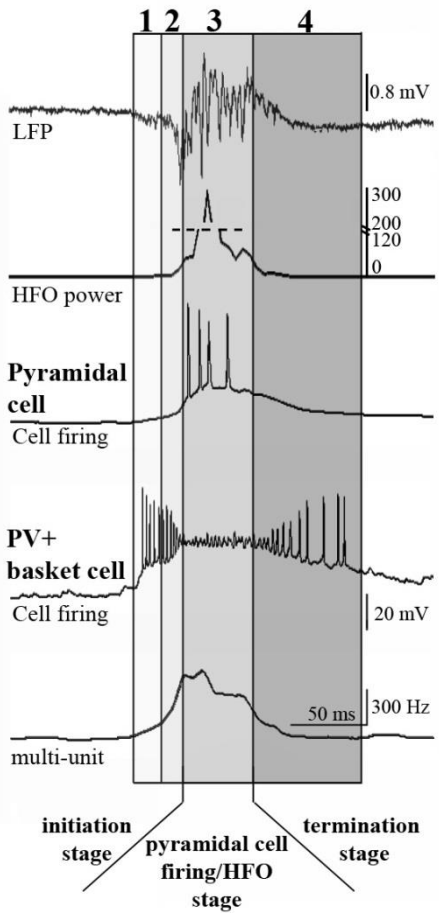

Figure 16. The firing of pyramidal cells and PV+ basket cells is complementary during different stages of interictal-like events. *The figure illustrate the behavior of pyramidal cells and PV+ basket cells during IIEs, recorded in current-clamp configuration (I = 0). During IIEs four stages can be distinguished: (1) Primary depolarization; mild negative deflection of local field potential (LFP), pyramidal cells start to depolarize, PV+ basket cells depolarize and start to fire, multi-unit activity increases. (2) Secondary depolarization; steep negative drop in the LFP, pyramidal cells depolarize further but do not fire, the firing rate of PV+ basket cells increases but the amplitude of action potentials decreases, multi-unit activity increases heavily. (3) IIEs build up, the high frequency oscillation power (HFO) increased in the 150-400 Hz band, as a result of strong depolarization pyramidal cells start to fire and PV+ basket cells cease to fire (depolarization block), multi-unit activity starts to drop. (4) LFP normalizes, pyramidal cells stop firing, PV+ basket cells exit the depolarization block and the firing gradually recovers, multi-unit activity drops.*

VI.1.8. High K^+ application alters cellular and network parameters

We also wanted to reveal the possible mechanisms responsible for the observed alterations in the firing properties of hippocampal cells. Therefore, we measured the basic parameters of PCs (n = 9) in control conditions and in the presence of 8.5 mM K^+. We found, that the membrane potential of cells depolarized from -59.2 mV (-62.1, -56.4) to -35.5 mV (-42.1, -27.1), the input resistance decreased from 68.2 MΩ (42.1, 114.8) to 29.1 MΩ (28.8, 44.2), and the threshold of the current injection required to induce at least one action potential decreased from 177 pA (153, 213) to 37 pA (156, 124). (Figure 17A).

We also measured the effect of high K^+ on the excitatory and inhibitory transmission (Figure 17B-D). Inhibitory postsynaptic currents were evoked by electrical stimulation (eIPSCs) on the border of strata pyramidale/lucidum (perisomatic inhibition) or in stratum radiatum (dendritic inhibition), in the presence of 20 μM NBQX and 50 μM AP5 to block fast excitatory transmission (Figure 17B, C). In both cases, the amplitude of triggered IPSCs significantly decreased in high K^+ compared to control conditions (to

45% for perisomatic inhibition (29.4, 54.9) and 58.5% (36.2, 78.9) for dendritic inhibition) (p = 0.002, paired Wilcoxon test). On the other hand, the amplitude of evoked excitatory postsynaptic currents (EPSCs) evoked in stratum radiatum significantly increased in high K^+ compared to control condition (136 %; 92.3, 216.1) (p = 0.002, paired Wilcoxon test) (Figure 17D).

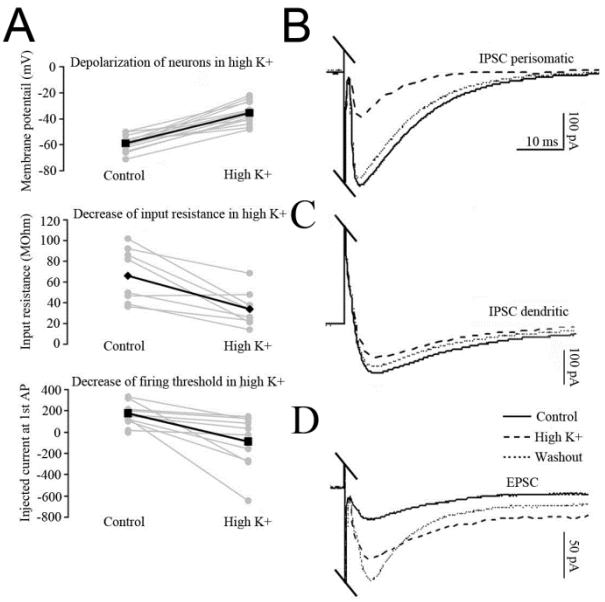

Figure 17. High K^+ increases excitability, decreases inhibitory and increases excitatory transmission. *A: In the presence of 8.5 mM K^+, pyramidal cells become more depolarized (top), and the input resistance (middle) and firing threshold (bottom) decreases. B: The amplitude of evoked perisomatic IPSCs dropped after high K^+ application. C: Similarly, the amplitude of evoked dendritic IPSCs also decreased. D: However, EPSCs evoked in high K^+ increased. Black line – control condition, dashed line – high K+, grey line – washout.*

These results indicate that the inhibitory function of interneurons is reduced, whereas excitatory synaptic transmission is increased in the presence of high K^+. Moreover, we found the strongest depression of perisomatic inhibition, which is considered to be the most important in the control of pyramidal cell firing (Miles et al., 1996a).

VI.1.9. The strength and short-term depression of PV+ basket cell – pyramidal cell synapses is modulated by high K^+ application

To uncover the exact changes of perisomatic inhibition in the presence of high K^+, we carried out paired recordings between monosynaptically coupled perisomatic region-targeting interneurons (PV+ BCs, AACs, CCK+ BCs) and PCs. Presynaptic PV+ BCs and AACs were targeted in slices prepared from transgenic mice expressing eGFP under

the control of PV promoter (Meyer et al., 2002), whereas CCK+ basket cells were targeted in mice where the CCK promoter regulated the expression of DsRed (Máté *et al.*, 2013).

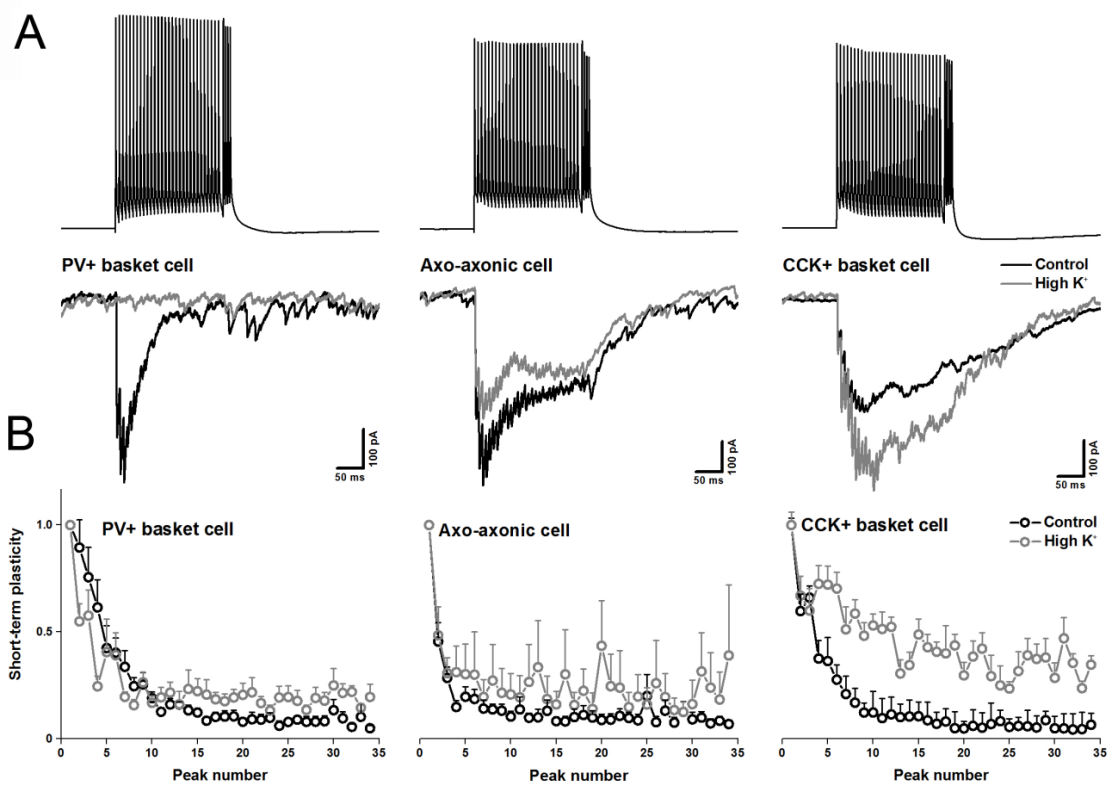

Figure 18. High K^+ alters inhibitory transmission between perisomatic region-targeting interneurons and their pyramidal cell targets. *A: Representative steady-state averaged IPSCs (from 10 sweeps) of PV+ BC-PC, AAC-PC and CCK+ BC-PC pairs. IPSCs were evoked by a trains of 30 APs at 160 Hz followed by 4 APs at 320 Hz, mimicking the behavior of interneurons during IIEs. At PV+ BC-PC and AAC-PC pairs the amplitude of IPSCs decreased in high K^+ (grey) compared to control condition (black), whereas at CCK+ BC-PC pairs increased. B: Short-term plasticity of IPSCs (median of averaged values normalized by the amplitude of 1st IPSC) in control condition (black) and in the presence of high K^+ (grey).*

Inhibitory postsynaptic currents (IPSCs) were evoked by a train of action potentials triggered in the presynaptic interneuron, similar to the firing of perisomatic region-targeting interneurons during IIEs (30 action potentials at 160 Hz followed by 4 action potentials at 320 Hz). We repeated the stimulation protocol in control condition and in the presence of high (8.5 mM) K^+, and compared the peak amplitude and short-term plasticity of triggered responses. IPSCs in pyramidal cells evoked by PV+ BCs (n = 7) and AACs (n = 7) were significantly decreased in high K^+ compared to control condition (P = 0.03 for PV+ BCs, P = 0.03 for AACs, paired Wilcoxon test). However, IPSCs

evoked by CCK+ BCs (n = 5) were nearly intact (P = 0.44, paired Wilcoxon test). We also found that both during control condition and in the presence of high K^+ IPSCs often disappeared before the stimulation train ended from PV+ BCs and AACs. In contrast, in case of CCK+ BC-PC pairs asynchronous release appeared even in the presence of high K^+ (Figure 18A).

We also analyzed whether the short-term plasticity becomes altered in high K^+. Therefore, the amplitude of evoked IPSCs was normalized to the amplitude of 1st IPSC, and plotted against stimulation number. As it is shown on Figure 18B, the short-term depression among PV+ BC-PC pairs became more prominent in the presence of high K^+, whereas no such change appeared in the case of AAC-PC pairs. On the other hand, the short-term depression at CCK+ BC-PC pairs was less pronounced, and the short-term depression could transiently switch to short-term facilitation. These results indicate, that inhibitory transmission provided by PV+ BCs during IIEs becomes largely ineffective compared to AACs and CCK+ BCs.

DOI:10.14753/SE.2018.2077

VI.2. Properties and dynamics of inhibitory transmission between pyramidal cells and interneurons expressing parvalbumin of cholecystokinin

In the previous chapter we could see that sharp wave-ripples and interictal-like events are different network phenomena with distinct properties. After pharmacological intervention the network activity reorganizes into a new form of synchrony. The balance of excitation and inhibition is shifted: inhibitory transmission is compromised, excitation is enhanced, which results in higher excitability of hippocampal neurons. PV+ basket cells enter into depolarization block, and inhibitory transmission provided by PV+ basket cells is greatly decreased. Moreover, the short-term depression of inhibitory postsynaptic currents originating from PV+ basket cells is increased.

The hippocampal activity patterns are primarily determined by the interaction among different types of interneurons and pyramidal cells. To understand the mechanisms underlying the generation of different network dynamics, in the next set of experiments we described quantitatively and qualitatively the connectivity between CA3 parvalbumin-positive and cholecystokinin-positive interneurons ant their target cells. We also described how interaction among these inhibitory cells and their local excitatory target neurons evolve over the course of physiological and pathological patterns. We also introduced a precise neuronal network model in order to understand how network dynamics is generated and how it can underlie information processing. Furthermore, we show how inhibitory dynamics between PV+ basket cells and pyramidal cells could contribute to sharp wave-ripple generation. All experiments were carried out in thick (350-450 μm) hippocampal slices and in modified '*in vivo*-like' ACSF with intention to mimic *in vivo* condition.

VI.2.1. Identification of interneuron-pyramidal cell and interneuron-interneuron cell pairs in the CA3 region of hippocampus

To study the properties of inhibitory synaptic transmission between different classes interneurons and their pyramidal cell targets, we used two transgenic fluorescent reporter mouse lines: PV+ BCs and AACs were targeted in mice where the PV promoter regulated the expression of eGFP (Meyer et al., 2002), whereas CCK+ cells were

DOI:10.14753/SE.2018.2077

identified in a transgenic line expressing DsRed under the control of CCK promoter (Máté et al., 2013). During paired recordings, all neurons were filled with biocytin and visualized *post hoc* using Alexa Fluor 488 conjugated streptavidin. Only interneurons with preserved axonal tree were included when calculating realized *vs.* possible connection. The identification of individual interneurons at interneuron to PC pairs is described in chapter I.4 and is presented on Figure 5. From a total number of 33 PV+ interneuron–PC pairs, we found 15 presynaptic PV+ BCs and 18 AACs. From a total number of 22 CCK+ cells 14 were identified as CCK+ BCs and 8 cells as CCK+ DTIs.

Interneuron to interneuron connections were also investigated in transgenic mouse lines. PV+ to PV+ pairs were targeted in PVeGFP mice (Meyer et al., 2002) and double immunostainig was performed against biocytin and ankyrin G

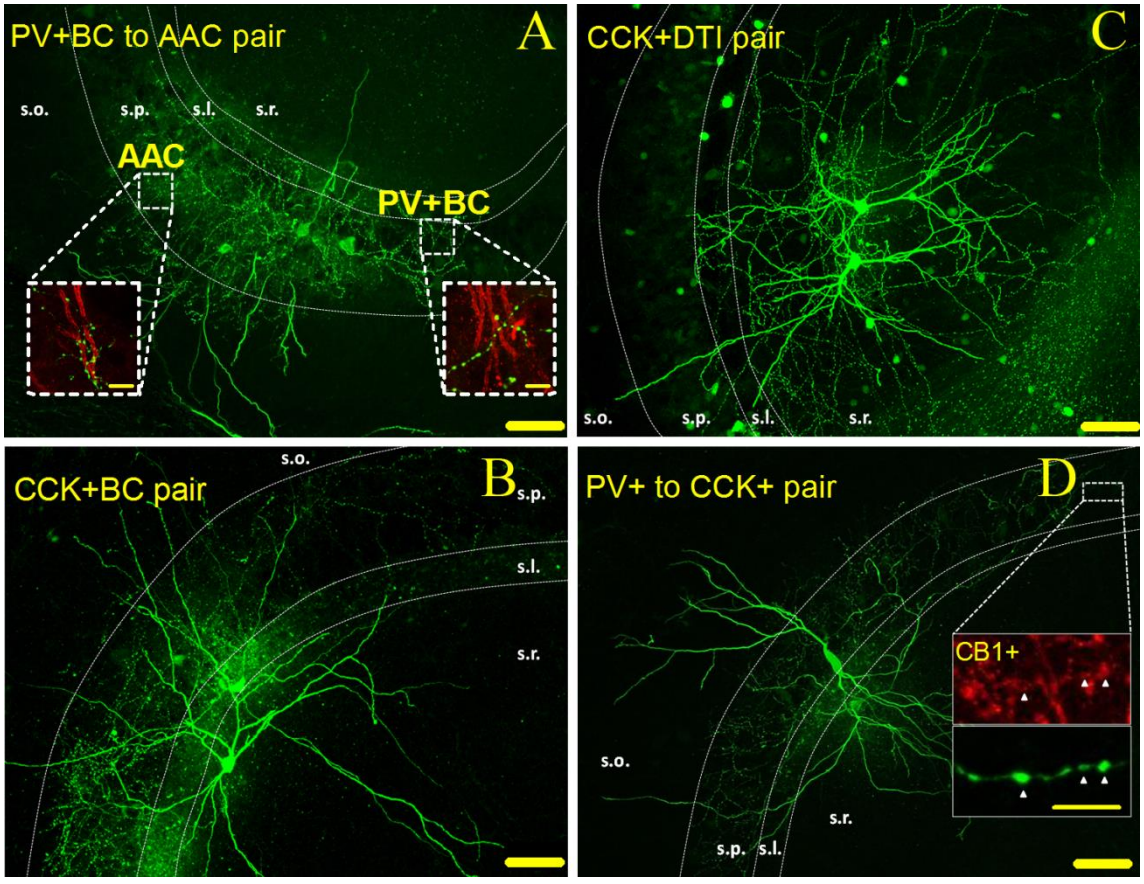

Figure 19. Identification of interneuron to interneuron cell pairs. *A: Confocal image of biocytin-filled PV+ BC to AAC pair from PVeGFP mice. To separate PV+ BCs from AACs, we selectively labeled the axon initial segment of PCs by ankyrin G (insets). There is no association between the boutons of PV+ BCs and AISs of PCs (right inset). The bouton rows of AACs outline the AISs of PCs (left inset). (green, PV+ BC and AAC bouton; red, AIS). B and C: Confocal images of biocytin-filled CCK+ BC (B) and CCK+ DTI (C) pairs from CCK DsRED mice. D: Confocal image of a PV+ to CCK+ cell pair from PVeGFP mice.*

Inset: CCK+ cells were identified by double-fluorescence staining against CB_1 cannabinoid receptor (red) and biocytin (green, visualizing the axons of filled interneurons). Axon terminals of CCK+ cells were CB_1-positive (white arrows), whereas axon terminals of PC+ cells were CB_1-negative (data not shown). Scale bar in A-D: 90 µm, scale bar in A insets: 10 µm, scale bar in D inset: 5 µm.

Because of the close proximity of cell bodies and axons of the two biocytin-filled PV+ interneurons, images of ankyrin G-labeled AIS and biocytin-labeled boutons were taken with confocal microscope (60x magnification) at specified areas of interest (Figure 139). Using these images and following the main myelinated axons of the cells, we could establish and identified both cells in a double interneuron recording, resulting in 34 PV+ BCs and 10 AACs.

CCK+ BC and CCK+DTI pairs were targeted from CCK DsRED mice (Máté et al., 2013). Altogether, 50 cells were filled with biocytin and analyzed *post hoc* with Alexa Fluor 488-conjugated streptavidin. Thirty cells were identified as CCK+ BCs (Figure 19B) and 20 cells were identified as CCK+ DTIs (Figure 18C).

To study physiological connections between PV+ and CCK+ cells, first, a PV+ interneuron was identified in a PVeGFP mice slice. Then a second, parvalbumin-negative (PV-) soma was patched in stratum lucidum, at the stratum lucidum/radiatum border or upper stratum radiatum. The identity of the second cell was confirmed using *post hoc* double-immunofluorescence labeling for biocytin and CB_1 cannabinoid receptor (Figure 19D) (Katona et al., 1999; Szabó et al., 2014). From a total of 28 PV negative cells, 14 were CB_1 cannabinoid receptor positive and were identified as CCK+ interneurons (Figure 19D).

VI.2.2. Hierarchical clustering based on electrophysiological properties identifies interneuron types

We also examined the feasibility of distinguishing different classes of interneurons based on their passive and active membrane properties. We injected a series of depolarizing and hyperpolarizing current steps into the soma of neurons recorded in the whole-cell current-clamp configuration, and extracted subthreshold and suprathreshold (spiking) response parameters (Figure 20A). A total of 40 different features were extracted from the voltage traces of 67 INs recorded in the CA3 region.

DOI:10.14753/SE.2018.2077

Following principal component analysis, we performed hierarchical clustering to reveal potential groupings in the physiological data. We found that the cells clearly formed two separate clusters based on their physiological features (Figure 20B, Table 3). *Post hoc* anatomical identification of the neuronal types revealed that the two main clusters corresponded almost perfectly to PV+ and CCK+ cells, respectively, with only a single PV+ cell misplaced into the group of CCK+ cells. This resulted in a more than 98% overlap between the anatomical and physiological classification.

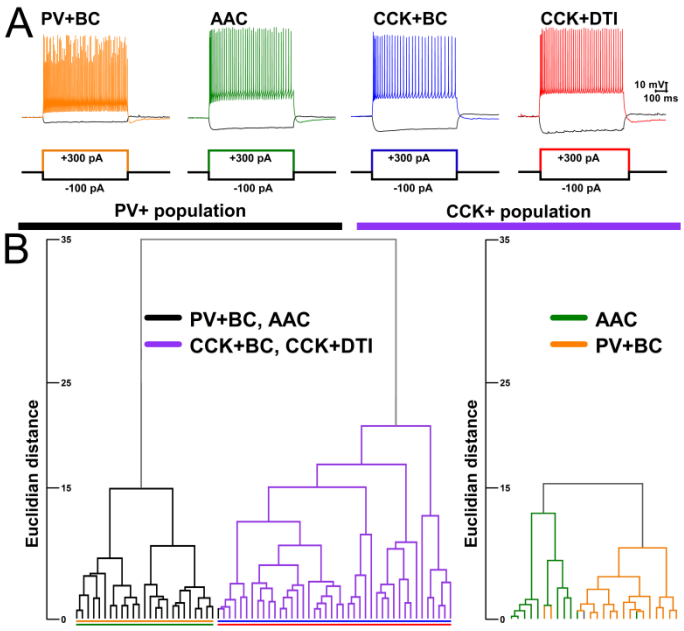

Figure 20. Identification of interneuron to interneuron cell pairs. *A: Representative examples of the voltage responses of PV+BCs, PV+ AACs, CCK+BCs and CCK+DTIs to increasing depolarizing and hyperpolarizing current steps. B: Hierarchical clustering based on 40 different electrophysiological features revealed two separate clusters, corresponding almost perfectly to PV+ (black) and CCK+ (purple) cells. Reclustering only PV+ cells can reasonably, but not perfectly separate PV+BCs from AACs (see text).*

PV+ and CCK+ neurons were significantly different from each other at the population level according to several features, including input resistance, membrane time constant, the maximal rate of firing for any input level, the accommodation of firing frequency, the amplitude and width of action potentials, and the amplitude and time course of the spike after-hyperpolarization (all $p<0.01$, Mann-Whitney U-test). The separation of the two classes was essentially complete for some of these features (see Table 3).

We also performed principal component analysis and clustering on the subgroup of 26 PV+ cells. We found that these cells could be assigned to two putative subgroups (Figure 20B), corresponding predominantly to PV+BCs (13 of 16) and AACs (8 of 10), with an overall match of approximately 83%. Morphologically identified PV+BCs and AACs differed significantly in terms of input resistance, rheobase current, maximal AP

number, AP width, duration and amplitude of after hyperpolarization (Table 4, all $p<0.01$, Mann-Whitney U-test). These results suggest that it might be possible to effectively separate PV+BCs and AACs based purely on their physiological features, especially if more sophisticated (supervised) learning methods were used instead of the simple exploratory techniques shown here.

Table 3: Comparison of physiological properties of PV+ and CCK+ interneurons. *Median values and interquartile ranges for PV+ and CCK+ cells are listed for each physiological feature. The last column shows the P values for comparisons between the medians according to a Mann–Whitney U test where P < 0.05 (NS, non-significant); it also marks the level of significance with stars (∗ P < 0.05; ∗∗ P < 0.01; ∗∗∗ P < 0.001).*

Parameters	PV+	CCK+	P value (MW)
Input resistance (Mohm)	55.64 (40.04, 67.32)	107.89 (51.80, 151.44)	0.001 (**)
Membrane time constant (ms)	8.80 (6.0, 11.0)	11.40 (9.05, 15.85)	0.002 (**)
Relative amplitude of hyperpolarizing sag	1.28 (1.16, 1.48)	1.24 (1.14, 1.50)	NS
Relative amplitude of rebound response following hyperpolarization	1.43 (1.28, 1.58)	1.28 (1.17, 1.70)	NS
Relative amplitude of early overshoot for depolarizing steps	1.15 (1.09, 1.29)	1.19 (1.09, 1.39)	NS
Rheobase current (pA)	125.0 (60.0, 162.0)	150.0 (90.0, 200.0)	NS
Maximal action potential number for any input current	145.50 (105.0, 162.0)	58.0 (47.75, 74.25)	$1.5x10^{-7}$ (***)
Voltage threshold (mV)	-43.11 (-48.68, -39.48)	-42.81 (-45.17, -41.45)	NS
Action potential amplitude (mV)	62.92 (48.58, 71.48)	74.27 (67.64, 79.80)	$0.1x10^{-3}$ (***)
Action potential rise time (ms)	0.0005 (0.0004, 0.0005)	0.0005 (0.0005, 0.0006)	0.003 (**)
Action potential half-width (ms)	0.32 (0.26, 0.37)	0.50 (0.38, 0.60)	$1.4x10^{-6}$ (***)
Action potential width (ms)	1.32 (1.16, 1.39)	1.73 (1.44, 2.09)	$3.9x10^{-6}$ (***)
Voltage difference between start and end of action potential (mV)	12.46 (9.54, 14.80)	11.16 (8.57, 13.56)	NS
Maximal steepness of rising phase of action potential (mV/ms)	246.2 (181.1, 330.0)	278.8 (230.0, 312.5)	NS
Voltage for maximal (positive) steepness of action potentials (mV)	-11.54 (-18.29, -3.12)	-3.66 (-12.61, 3.40)	0.007 (**)
Maximal (negative) steepness of falling phase of APs (mV/ms)	-203.2 (-231.4, -178.9)	-135.5 (-188.9, -118.7)	0.1x10-3 (***)
Voltage for maximal negative steepness of APs (mV)	-7.61 (-18.01, 0.72)	5.53 (-7.52, 16.29)	$0.9x10^{-3}$ (***)
Amplitude of after-hyperpolarization (mV) (old method)	-0.05 (-0.54, 0.21)	0.45 (-0.02, 1.24)	0.01 (*)
Duration of after-hyperpolarization (ms) (old method)	0.30 (0.22, 0.39)	0.41 (0.27, 4.83)	NS
Amplitude of after-hyperpolarization (mV) (new method)	12.46 (9.93, 15.01)	12.68 (9.64, 14.55)	NS
Duration of after-hyperpolarization (ms) (new method)	1.59 (1.33, 1.80)	2.38 (1.77, 6.94)	0.003 (**)
Latency of first action potential (ms)	118.80 (36.40, 429.60)	56.80 (33.10, 95.20)	0.03 (*)
Action potential number in “steady” trace (*)	23.0 (12.0, 34,0)	15.0 (11.0, 21.0)	0.01 (*)
Average inter-spike interval (ms) in “steady” trace (*)	33.25 (22.48, 51.76)	51.94 (38.20, 70.12)	0.002 (**)
Action potential half-width (ms) in “steady” trace (*)	0.34 (0.29, 0.37)	0.57 (0.46, 0.71)	$3.86x10^{-7}$ (***)
Action potential amplitude (mV) in “steady” trace (*)	57.92 (52.51, 68.47)	71.20 (66.31, 75.39)	$5.77x10^{-5}$ (***)
Voltage threshold (mV) in “steady” trace (*)	-42.04 (-44.05, -39.58)	-40.99 (-43.76, -39.65)	NS

Parameters	PV+	CCK+	P value (MW)

Difference in threshold (mV) in "steady" trace (*)	24.81 (18.86, 26.54)	27.03 (24.51, 32.25)	$0.2x10^{-4}$ (***)
Action potential width (ms) in "steady" trace (*)	1.32 (1.19, 1.40)	1.99 (1.66, 2.36)	$9.66x10^{-7}$ (***)
Voltage difference between start and end of AP (mV) in "steady" trace (*)	13.74 (10.19, 15.90)	10.22 (8.22, 13.48)	0.006 (**)
Amplitude of after-hyperpolarization (mV) (old method, "steady" trace (*))	-0.08 (-0.28, 0.16)	1.53 (-0.01, 2.88)	$6.59x10^{-5}$ (***)
Duration of after-hyperpolarization (ms) (old method, "steady" trace (*))	0.26 (0.23, 0.33)	5.64 (0.33, 9.02)	0.1x10-3 (***)
Spike frequency accommodation	1.50 (0.60, 2.75)	2.92 (1.76, 7.39)	$9.75x10^{-5}$ (***)
Change in inter-spike intervals between start and end of step (ms)	16.39 (3.31, 34.38)	54.44 (29.66, 107.49)	$3.37x10^{-5}$ (***)
Steepness of ISI change vs. AP number relation (ms)	0.36 (-0.05, 1.26)	2.61 (1.06, 7.34)	$9.47x10^{-6}$ (***)
Change in action potential half-width during step (ms)	0.01 (-0.003, 0.3)	0.13 (0.06, 0.18)	$5.81x10^{-6}$ (***)
Steepness of AP half-width change vs. AP number relation (ms)	0.0004 (-0.0002, 0.001)	0.006 (0.002, 0.012)	$4.55x10^{-7}$ (***)
Change in action potential amplitude during step (mV)	1.56 (-4.79, 3.48)	-2.68 (-6.38, 4.24)	NS
Steepness of AP amplitude change vs. AP number relation (mV)	0.04 (-0.10, 0.14)	-0.15 (-0.37, 0.19)	NS
Measure of cell excitability	0.52 (0.23, 0.70)	0.29 (0.19, 0.57)	NS

Finally, we also attempted to identify subgroups within the cluster of CCK+ neurons. However, the branching structure of hierarchical clustering did not reveal any well-separated clusters, and the clusters that could be defined did not show any correspondence to the two major anatomical subclasses of CCK+ neurons (BCs vs. DTIs; data not shown). This suggests, in agreement with recent findings (Szabó et al., 2014), that CCK+BCs and CCK+DTIs form a physiological continuum.

Table 4: Comparison of physiological properties of PV+ BCs cells and AACs. *Median values and interquartile ranges for PV+ and CCK+ cells are listed for each physiological feature. The last column shows the P values for comparisons between the medians according to a Mann–Whitney U test where $P < 0.05$ (NS, non-significant); it also marks the level of significance with stars ($* P < 0.05$; $** P < 0.01$; $*** P < 0.001$).*

Parameters	**PV+**	**CCK+**	**P value (MW)**
Input resistance (Mohm)	42.12 (33.22, 51.80)	79.47 (70.18, 100.47)	$0.1x10^{-3}$ (***)
Membrane time constant (ms)	7.20 (5.75, 10.20)	11.0 (9.05, 11,75)	0.04 (*)
Relative amplitude of hyperpolarizing sag	1.28 (1.16, 1.41)	1.21 (1.14, 1,30)	NS
Relative amplitude of rebound response following hyperpolarization	1.35 (1.28, 1.57)	1.22 (1.18, 1.37)	NS
Relative amplitude of early overshoot for depolarizing steps	1.13 (1.08, 1.27)	1.17 (1.11, 1.27)	NS
Rheobase current (pA)	250 (200, 400)	100.0 (85.0, 150.0)	$0.6x10^{-3}$ (***)
Maximal action potential number for any input current	109.0 (80.75, 136.50)	162.0 (154.4, 169.5)	0.001 (**)
Voltage threshold (mV)	-41.78 (-43.43, -39.17)	-41.61 (-44.64, -40.05)	NS
Action potential amplitude (mV)	51.32 (45.48, 67.24)	67.19 (62.30, 71.63)	NS
Action potential rise time (ms)	0.0005 (0.0004, 0.0005)	0.0005 (0.0004, 0.0005)	NS
Action potential half-width (ms)	0.26 (0.25, 0.33)	0.37 (0.34, 0.40)	0.004 (**)

DOI:10.14753/SE.2018.2077

Parameters	PV+	CCK+	P value (MW)
Action potential width (ms)	1.25 (1.12, 1.31)	1.38 (1.31, 1.45)	0.007 (**)
Voltage difference between start and end of action potential (mV)	14.75 (13.27, 16.78)	11.57 (9.72, 13.03)	0.001 (**)
Maximal steepness of rising phase of action potential (mV/ms)	220.70 (179.32, 300.35)	250.0 (187.87, 293.46)	NS
Voltage for maximal (positive) steepness of action potentials (mV)	-7.55 (-17.94, -2.40)	-13.44 (-19.56, -1.80)	NS
Maximal (negative) steepness of falling phase of APs (mV/ms)	-233.4 (-242.2, -186.5)	-206.5 (-230.1, -175.6)	NS
Voltage for maximal negative steepness of APs (mV)	-9.43 (-22.09, -3.04)	1.65 (-13.60, 7.41)	NS
Amplitude of after-hyperpolarization (mV) (old method)	-0.11 (-0.61, 0.03)	0.02 (-0.26, 1.09)	NS
Duration of after-hyperpolarization (ms) (old method)	0.22 (0.21, 0.28)	0.39 (0.32, 7.13)	0.01 (*)
Amplitude of after-hyperpolarization (mV) (new method)	14.93 (12.63, 16.74)	11.96 (9.73, 13.51)	0.02 (*)
Duration of after-hyperpolarization (ms) (new method)	1.39 (1.31, 1.57)	1.80 (1.62, 8.53)	0.008 (**)
Latency of first action potential (ms)	39.20 (24.90, 172.15)	162.60 (32.15, 432.25)	NS
Action potential number in “steady” trace (*)	24 (14.25, 39.00)	25.0 (15.75, 30.25)	NS
Average inter-spike interval (ms) in “steady” trace (*)	33.37 (20.12, 54.30)	31.83 (25.77, 46.0)	NS
Action potential half-width (ms) in “steady” trace (*)	0.31 (0.26, 0.33)	0.36 (0.35, 0.39)	0.001 (**)
Action potential amplitude (mV) in “steady” trace (*)	53.81 (45.23, 64.03)	66.09 (64.11, 70.67)	0.02 (*)
Voltage threshold (mV) in “steady” trace (*)	-41.04 (-42.65, -38.86)	-42.60 (-42.89, -39.46)	NS
Difference in threshold (mV) in “steady” trace (*)	26.06 (23.14, 28.65)	24.41 (20.59, 25.50)	NS
Action potential width (ms) in “steady” trace (*)	1.27 (1.12, 1.32)	1.39 (1.35, 1.44)	0.004 (**)
Voltage difference between start and end of AP (mV) in “steady” trace (*)	15.72 (14.22, 17.20)	10.52 (9.90, 12.11)	$0.1x10^{-3}$ (***)
Amplitude of after-hyperpolarization (mV) (old method, “steady” trace (*))	-0.21 (-0.38, -0.06)	0.16 (-0.10, 0.76)	0.01 (*)
Duration of after-hyperpolarization (ms) (old method, “steady” trace (*))	0.23 (0.21, 0.25)	0.33 (0.27, 4.67)	0.01 (*)
Spike frequency accommodation	2.76 (1.38, 3.47)	2.04 (1.11, 3.0)	NS
Change in inter-spike intervals between start and end of step (ms)	26.15 (11.96, 65.00)	16.47 (10.63, 30.74)	NS
Steepness of ISI change vs. AP number relation (ms)	0.67 (0.21, 2.81)	0.55 (0.37, 1.19)	NS
Change in action potential half-width during step (ms)	0.01 (0, 0.03)	0.02 (-0.06, 0.05)	NS
Steepness of AP half-width change vs. AP number relation (ms)	0.0004 (-0.0002, 0.0013)	0.0007 (-0.002, 0.001)	NS
Change in action potential amplitude during step (mV)	2.06 (-2.82, 3.24)	3.20 (-5.19, 9.65)	NS
Steepness of AP amplitude change vs. AP number relation (mV)	0.04 (-0.07, 0.16)	0.08 (-0.13, 0.40)	NS
Measure of cell excitability	0.60 (0.44, 1.13)	0.53 (0.33, 0.81)	NS

VI.2.3. Frequency of interactions among homogeneous and heterogeneous types of inhibitory neurons

After identification of interneurons we calculated the probability of connections among different inhibitory cell types. During the experiments we filled and visualized all cells regardless the presence of a physiological connection. Connection probability among different classes of INs was calculated as the proportion of physiologically

connected IN pairs from all possible unidirectional pairs where the axonal arbor of the presynaptic neuron was present (not cut or unfilled).

We calculated all possible connection probabilities between the two main populations (PV+ to PV+, CCK+ to CCK+, PV+ to CCK+ and CCK+ to PV+) and between subpopulations within the two major cell classes (PV+ population: PV+BC to PV+BC, PV+BC to AAC, AAC to PV+BC and AAC to AAC; CCK+ population: CCK+BC to CCK+BC, CCK+DTI to CCK+DTI, CCK+BC to CCD+DTI and CCK+DTI to CCK+BC).

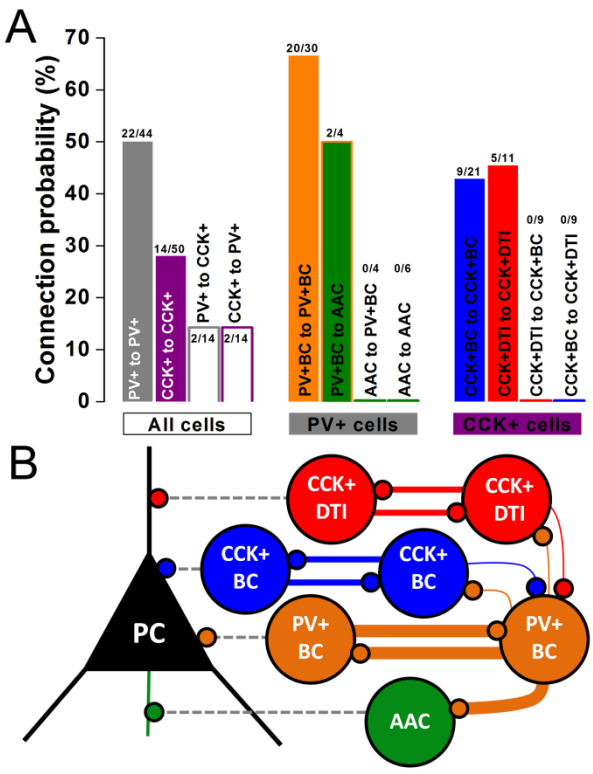

Figure 21: Homogeneous PTI pairs have frequent reciprocal connections. A: Connection probability among PV+ and CCK+ cell populations, within the PV+ population and within the CCK+ population. Only cells with preserved axonal tree were included in the counting. Note the higher connection probability between homogeneous cell pairs. B: Representative scheme of the connection rules of PTI and DTI neurons. The thickness of colored lines represents the observed connection probability between interneuron pairs.

Table 5: Observed connection frequency of identified interneurons with preserved axonal tree in the CA3 region of mouse hippocampus. *CB1R+, cannabinoid type 1 receptor-positive interneuron; CB1R-, cannabinoid type 1 receptor-negative interneuron; Gap J., gap junction; No, no pair; Uni., unidirectional connection; Bi., bidirectional connection.*

Connection type	No	Uni.	Bi.	Gap J.	Connection type	No	Uni.	Bi.	Connection type	No	Uni.
PV+BC to PV+BC	10	6	7	4	CCK+BC to CCK+BC	12	3	3	PV+ to CCK+ (CCB1R+)	10	2
PV+BC to AAC	2	2		1	CCK+DTI to CK+DTI	6	1	2	CCK+ to PV+ (CB1R-)	9	2
AAC to AAC	6			1	CCK+BC to CCK+DTI	9					
AAC to PV+BC	4			1	CCK+DTI to CCK+BC	9					

DOI:10.14753/SE.2018.2077

Connection probability was remarkably high between PV+ cells (Figure 21, Table 5). From a total of 44 putative cell pairs (including PV+BCs and AACs) we found 22 pairs (connection probability=50%). The connection probability among PV+BCs was 66.6% (6 unidirectional and 7 bidirectional pairs, from which 3 cell pairs were also gap junction connected, data not shown). We found 2 PV+BC to AAC pairs (connection probability=50%). On the other hand, no AAC to PV+BC or AAC to AAC connections were found. The difference in the likelihood with which PV+BCs and AACs contacted other PV+ INs was highly significant ($p=6.21\times10^{-4}$; chi-square test). However, even in the absence of synaptic connections, we found an electrically coupled AAC to AAC pair (1 out of 6 AAC-AAC dual recordings).

The connection probability between CCK+ cells was relatively high (28%), with frequent bidirectional connections, however, we observed synaptic coupling only between homogeneous CCK+BC (connection probability=42.85%) and CCK+DTI (connection probability=45.45%) pairs. The preference of CCK+ INs for homologous postsynaptic partners was highly significant ($p=9.42\times10^{-4}$).

We also found physiological evidence of rare PV+ to CCK+ and CCK+ to PV+ connections. From a total of 28 trials among PV+ and CCK+ cells only 2 PV+ to CCK+ and 2 CCK+ to PV+ pairs were found. Overall, PV+ and CCK+ INs were more likely to target INs within the same main class (p=0.0175), and PV+ cells in particular preferentially targeted other PV+ INs rather than CCK+ cells (p=0.0181). The findings are summarized in Figure 21 and Table 5.

Our results support the idea that INs of the same class tend to form reciprocally connected networks (Chamberland and Topolnik, 2012). As far as we know, we report here for the first time physiological evidence of PV+BC to AAC and PV+ to CCK+ IN synapses within the CA3 region of mouse hippocampus. It is also important to note that while PV+BCs form a massively (often reciprocally) interconnected network and occasionally innervate AACs, these latter cells do not innervate each other or PV+BCs.

DOI:10.14753/SE.2018.2077

VI.2.4. The type of IN determines the properties of unitary IPSCs onto PCs

First we characterized the basic properties of inhibitory synaptic transmission between INs and their PC targets. Interneurons were recorded with a high KCl-based intrapipette solution. CB_1 receptor antagonist AM251 was added to the perfusate to eliminate the potential tonic activation of CB_1 receptors at the output synapses of CCK+ cells, which might significantly alter the synaptic properties (Lenkey et al., 2015). We calculated the basic properties of uIPSCs (10-90% rise time, decay time constant, latency, peak amplitude, synaptic potency and transmission probability) by averaging events evoked by single presynaptic spikes. The transmission variables of PV+BCs, AACs and CCK+BCs are shown in Figure 22.

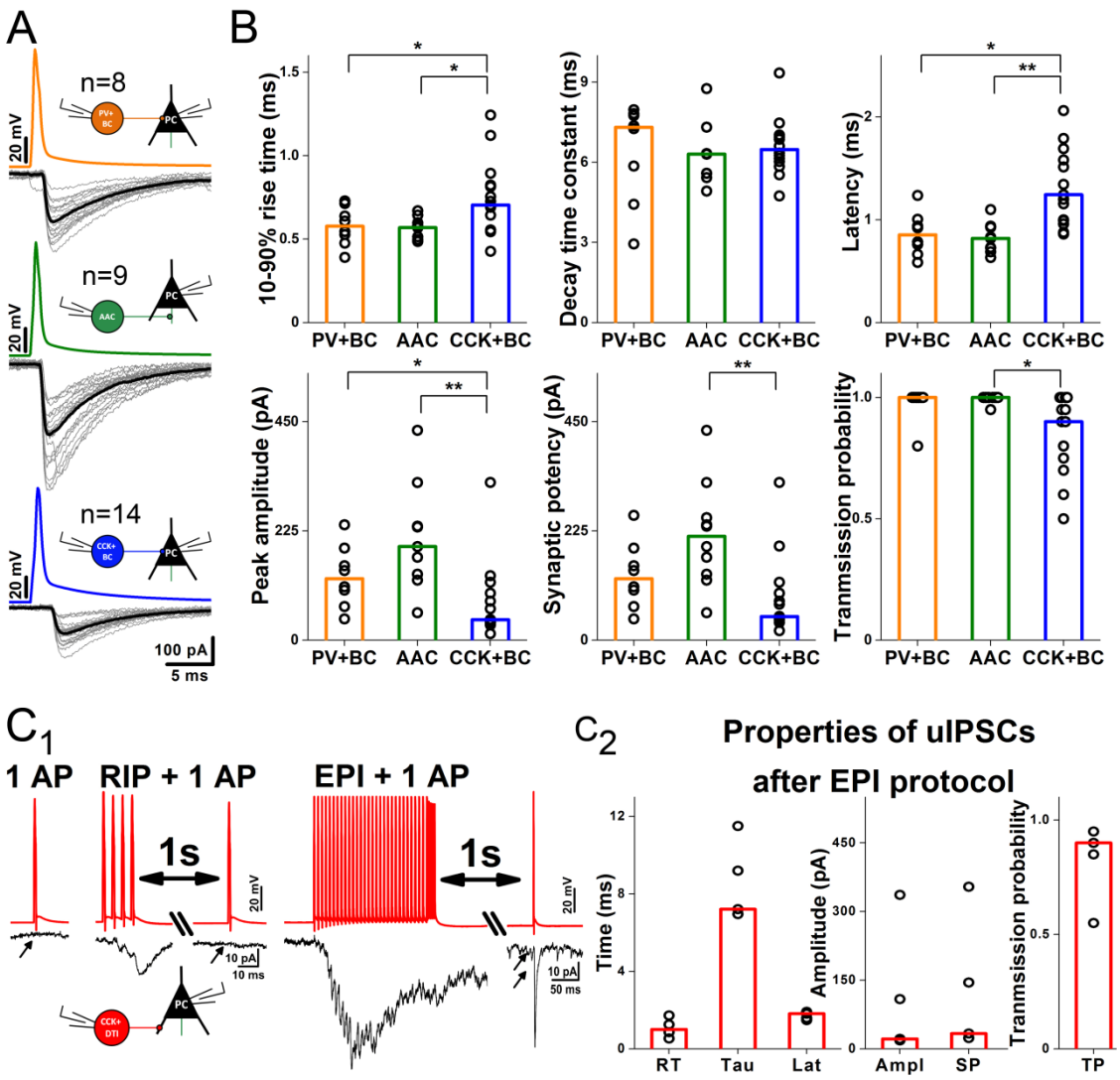

Figure 22: Properties of unitary IPSCs between interneuron-pyramidal cell pairs depend on presynaptic cell type. *A: Representative scheme of 20 superimposed uIPSCs (gray) between different classes of PTIs and PCs. The average of uIPSCs measured in PCs is shown in black. B: Summary of 10-90% rise time (ms), decay time constant (τ, defined as the time constant of the single-exponential fit to the decaying phase of averaged uIPSCs, ms), latency (ms), peak amplitude (pA), synaptic potency (amplitude of uIPSCs excluding failures, pA) and transmission probability (ratio of all action potentials and successful uIPSCs) for different connection types. Bars indicate the median of individual PTI-PC pair values (black circles). Asterisks indicate significant differences (* P < 0.05, ** P < 0.01). PV+ cells evoked larger and faster events with shorter decay and higher probability than CCK+ cells.. C_1: No uIPSCs in CCK+DTI-PC pairs for a single AP and for an AP following RIP protocol stimulation could be detected. A single AP could evoke uIPSCs only if it was preceded by EPI protocol stimulation. C_2: Summary bar graph of uIPSCs at CCK+DTI-PC pairs following EPI protocol stimulation.*

CCK+DTIs (7 of 8) did not transmit either for a single AP or for an AP following a RIP protocol AP burst (4 APs at 160 Hz). A single AP evoked transmission only if it was preceded by a longer-lasting high-frequency EPI burst (30 APs at 160 Hz followed by 4 APs at 320 Hz) (Figure 22C_1). Transmission values for this case are plotted in Figure 22C_2.

Statistical comparisons (Kruskal-Wallis ANOVA, KW) revealed that the three PTI-evoked uIPSCs were different in 10-90% rise time (P_{KW}=0.027), latency (P_{KW}=7.49x10^{-4}), amplitude (P_{KW}=0.001), synaptic potency (P_{KW}=0.004) and transmission probability (P_{KW}=0.003). Additional *post hoc* statistical investigations (Bonferroni-corrected Mann-Whitney U test, MW) revealed that uIPSCs mediated by PV+BCs (n=8) and AACs (n=9) had significantly faster 10-90% rise, shorter latency and larger peak amplitude compared to CCK+ BC-PC pairs (n=14). Moreover, AAC-PC pairs had larger synaptic potency than CCK+BC-PC pairs, and CCK+BC-PC pairs had significantly smaller transmission probability than AAC-PC pairs (Figure 22B).

VI.2.5. Cell type-specific short-term plasticity characterizes the synaptic transmission of INs onto PCs

To completely characterize the transmission of a synapse its short-term plasticity parameters also need to be measured. Therefore, we examined the dynamic properties of inhibitory transmission at IN-PC synapses using firing patterns observed during SWRs

DOI:10.14753/SE.2018.2077

(RIP protocol, 4 APs at 160 Hz) or during pathologic IIEs (EPI protocol, 30 APs at 160 Hz followed by 4 APs at 320 Hz) in the CA3 region of mouse hippocampus *in vitro* (Hájos *et al.*, 2013). The connections were also tested with 10 APs at different frequencies in the 1-320 Hz range.

We found significant differences in the short-term plasticity of IPSCs between different classes of IN-PC synapses during the stimulation trains (Figure 23-24). The average release dynamics in PV+ neurons was characterized by short-term depression (STD). The release of CCK+ cells was more complex, showed large individual differences among cells, but in general expressed short-term facilitation (STF).

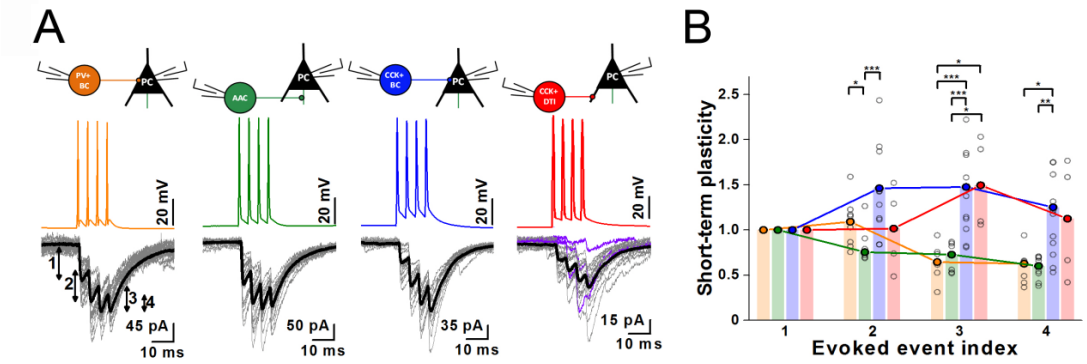

Figure 23: Short-term plasticity of inhibitory transmission for physiological activity pattern is presynaptic cell-type dependent. *A: Representative examples of 20 superimposed IPSCs (grey) recorded from PCs, evoked by RIP protocol (a train of 4 APs at frequency of 160 Hz) in PV+ BC (orange), AAC (green), CCK+ BC (blue) and CCK+ DTI (red). The steady-state average of IPSCs is shown in black; purple lines at CCK+ DTI-PC pairs represent the first three traces where the 1st AP of RIP protocol did not result in an ISPC. To analyze short-term plasticity, the amplitudes of triggered IPSCs were normalized to the amplitude of 1st IPSC. B: Summary of release dynamics recorded in PV+ BC – PC, AAC – PC, CCK+ BC – PC and CCK+ DTI – PC pairs. Bars show the median of normalized peak amplitudes to the 1st IPSC amplitude for individual cell pairs (filled black circles). Amplitude are plotted against stimulation number for each pair. Curves represent the calculated short-term plasticity of IPSCs. The transmission of PV+ BC – PC and AAC – PC pairs showed short-term depression, whereas that of CCK+ BC – PC and CCK+ DTI – PC pairs showed short-term facilitation.*

Transmission of PV+ cells is depressing and homogenous: Figure 23 demonstrates that PV+BC-PC pairs (n=8) expressed STD in response to the 3rd and 4th APs of the RIP protocol, while AAC-PC synapses (n=9) already for the 2nd AP. As it is shown in Figure 24A and Figure 24C, PV+BC-PC (n=6) and AAC-PC (n=8) pairs displayed purely STD

in response to 10 APs at frequencies between 1-320 Hz and to EPI protocol. The STD becomes more prominent with increasing frequency. The evoked IPSCs were synchronous to APs, even during the high frequency EPI stimulation pattern.

Transmission of CCK+ cells is variable with a trend of facilitation and asynchronous release: IPSCs between CCK+BC-PC (n=14) and CCK+DTI-PC pairs (n=4) were characterized by powerful STF in response to RIP protocol; however, individual cell pairs could display both short-term facilitation and short-term depression (Figure 23). The onset of asynchronous release was also observed at different stimulation frequencies for different CCK+ cells (Figure 24A, C).

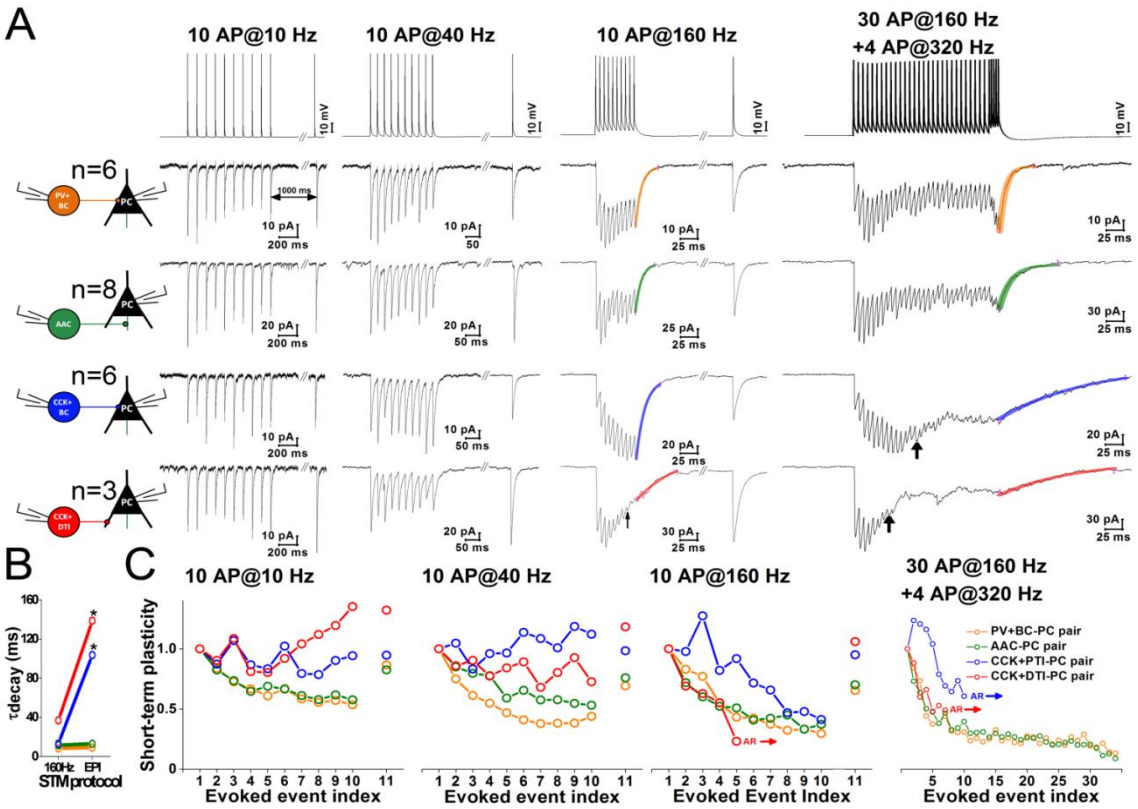

Figure 24: Short-term plasticity of inhibitory transmission depends both on frequency and the type of the presynaptic cell. *A: Representative averaged IPSCs (from 10 sweeps) of PV+ BC-, AAC-, CCK+ BC- and CCK+ DTI – PC pairs. IPSCs were evoked by a train of 10 APs at frequencies 10, 40, 160 Hz (to measure short-term depression, STD), followed by an additional 11th AP after 1 s (to measure recovery from STD), or by the EPI protocol (30 APs at 160 Hz + 4 APs at 320 Hz) mimicking the behavior of PTIs during pathological interictal events. At CCK+PTI-PC pairs, asynchronous release appeared in response to the EPI protocol after the 10th AP (black arrow), whilst at CCK+DTI-PC pairs asynchronous release was observed during the 10 AP at 160 Hz stimulation train and EPI protocol after the 5th AP (black arrow). Colored curves represent the single exponential fit function to the decay of the 10th IPSC at 160 Hz and*

EPI protocol stimulation. B: Summary data of median values of decay time constant at different patterns. Asterisks indicate that the decay time of the CCK+BC and PTI cells were significantly longer after the EPI protocol, indicating that a delayed asynchronous release follows the last AP. C: Summary of onset and recovery of short-term plasticity of IPSCs (median of averaged values normalized by the amplitude of 1st IPSC), plotted against evoked events. Note that PV+BC- and AAC-PC pairs were characterized by short-term depression at each frequency and stimulation pattern, whilst CCK+BC-PC and CCK+DTI-PC pairs displayed short-term facilitation. AR, asynchronous release.

The details of the transmission at the output synapses of CCK+BCs and DTIs were different. All CCK+BC-PC pairs (n=6) were characterized by STF at frequencies between 1-40 Hz. At higher frequencies (10 APs at 80 Hz, 160 Hz, 320 Hz and EPI protocol) the transient STF of the 1^{st}-5^{th} APs turned later into STD . We also observed asynchronous release (AR) at CCK+BC-PC pairs appearing only during the EPI protocol between the 10^{th} and 19^{th} AP (median, interquartile range, 11 (10, 14)) (Figure 24).

In the case of CCK+DTIs release for single APs was observed only following a pathological burst of APs in the EPI protocol (Figure 25). This suggests that the facilitating effect of the burst is long-lasting, since 1600 ms elapsed between the burst and the test impulse. From a total of 8 CCK+ DTI-PC pairs only 4 pairs responded to stimulation already at low frequencies (1-40 Hz) or to RIP protocol with clearly distinguishable inhibitory transmission (Figures 23A, 24A). Transmission was characterized by STF at 10 Hz (n=3), but it turned into STD at 40 Hz (n=3) and 160 Hz (n=4) stimulation. In the remaining 4 DTI-PC pairs inhibitory transmission (showing STD) was observed only for the stronger and longer lasting EPI stimulation train (Figures 24, 25).

DOI:10.14753/SE.2018.2077

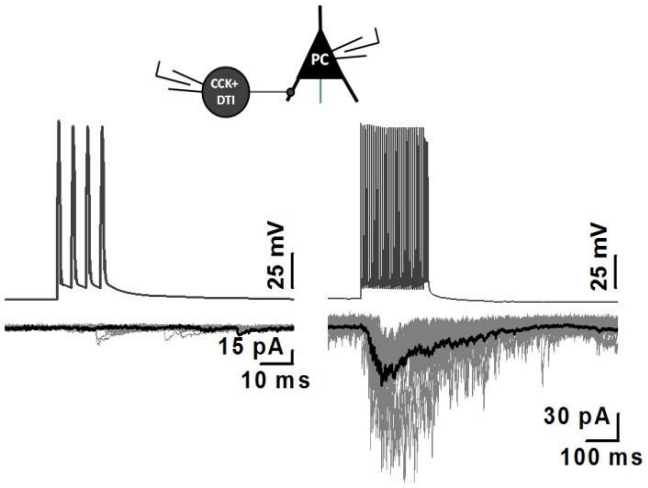

Figure 25: The inhibitory transmission at CCK+ DTI – PC pairs is stimulation pattern dependent*. The physiological RIP protocol (4 APS at 160 Hz, left) evokes no response on four CCK+ DTI – PC pairs. By increasing the presynaptic firing rate at the same pairs (pathological EPI protocol, 30 APs at 160 Hz followed by 4 APs at 320 Hz), synchronous release appears followed by asynchronous release after the 5th AP.*

In the CCK+DTI cells asynchronous release appeared earlier than for the BCs: between the 7th and 13th AP of the EPI protocol (median, interquartile range, 7 (7, 9)) and above 160 Hz stimulation (median, interquartile range, 7 (6, 8)) (Figure 24B, C).

We also quantified the pattern dependence of AR, by calculating the decay time and the charge (in a 500 ms-long window) following the last AP of the EPI protocol and the 160 Hz stimulation (Figure 24A last 2 columns). At CCK+BC-PC pairs, the EPI protocol triggered a significantly larger asynchronous charge compared to 160 Hz stimulation (P_{MW}=0.002), whilst the charge transfer at PV+BC-PC (P_{MW}=0.17) and AAC-PC pairs (P_{MW}=0.27) was unchanged between the two stimulus patterns. We did not find any significant difference in the asynchronous charge transfer at CCK+DTI-PC pairs (P_{MW}=0.9), as asynchronous release appeared at both stimulation patterns. However, the decay time (τ) of release prolonged significantly during EPI protocol compared to 160 Hz stimulation at both CCK+BC-PC (from 13.01 ms to 103.65 ms, P_{MW}=0.01) and CCK+DTI-PC pairs (from 36.82 ms to 138.71 ms, P_{MW}=0.01) (Figure 24B).

To fully understand the temporal properties of transmission not only the onset of the plasticity, but the recovery has to be measured. To this end, we also ran a protocol where uIPSCs were triggered by two RIP protocols with varying interstimulus intervals between 50 and 1200 ms (Figure 26A). The recovery ratio of evoked amplitudes was calculated and plotted against the interstimulus interval (Figure 26B). PV+BC-PC (n=7) and AAC-PC (n=9) transmission gradually recovered, whilst CCK+BC-PC transmission (n=11) showed a more complex (increasing and decreasing) behavior depending on the interstimulus interval.

DOI:10.14753/SE.2018.2077

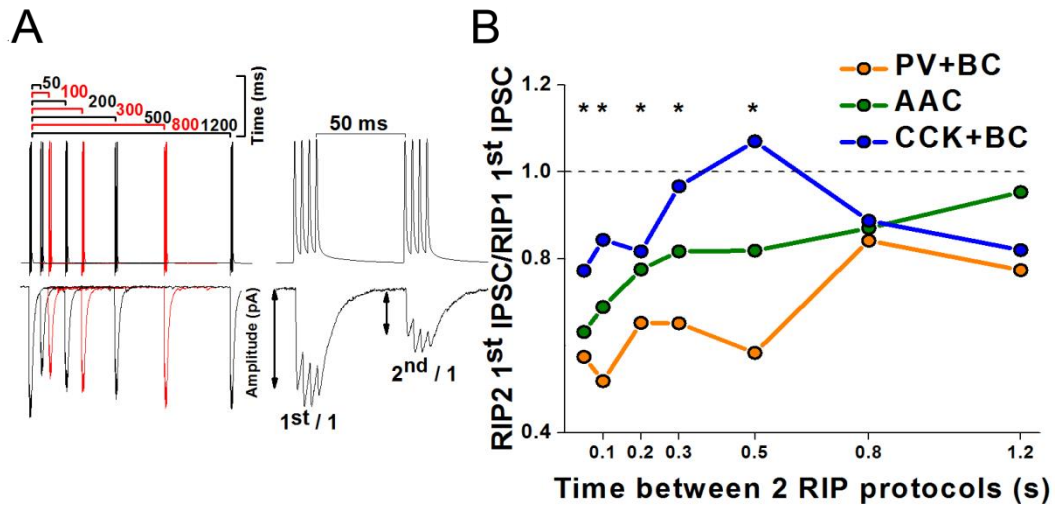

Figure 26: The recovery from inhibition is presynaptic cell-type dependent*. A: The recovery of transmission was calculated from 2 sets of RIP protocol trains, where the interstimulus interval between the final action potential of the first train and the first AP of the second train was varied between 50 and 1200 ms. B: Subsequently, the recovery ratio of evoked IPSCs was calculated (amplitude of the first IPSC of the second train divided by the amplitude of the first IPSC of the first train), and plotted against the interstimulus interval. Note, that PV+BC-PC (n=7) and AAC-PC (n=9) transmission gradually recovered, whilst CCK+BC-PC transmission (n=11) showed a more complex (increasing and decreasing) behavior depending on the interstimulus interval. Asterisks mark the significant difference between PV+BC-PC and CCK+BC-PC pairs for the given recovery time (* P < 0.05, ** P < 0.01, *** P < 0.001).*

Thus, while PV+ transmission tended to be reliable but depressing, the transmission properties of CCK+ cells are heterogeneous with a trend towards STF. As extreme forms, some CCK+ cells do not transmit at low frequencies. In contrast to PV+BCs and AACs that reliably and precisely evoke IPSCs, CCK+ cells can release GABA asynchronously in a stimulation-dependent manner.

VI.2.6. Properties of unitary IPSCs among INs are also connection type specific

Our morphological, immunocytochemical and electrophysiological analysis revealed six realized types of connection among perisomatic- and dendritic-region targeting interneurons, from which three were homogeneous: PV+ basket cell to PV+ basket cell, CCK+ basket cell to CCK+ basket cell and CCK+ dendritic-region targeting interneuron to CCK+ dendritic-region targeting interneuron (Figure 21). Because of low incidence, properties of heterogeneous cell pairs are not detailed in this study (PV+ basket

cell to AAC, n=2; PV+ to CCK+, n=2; CCK+ to PV+, n=2). We found significant differences in the properties of uIPSCs among homogeneous pairs (Figure 27). As it is shown in Figure 27B, uIPSCs at PV+ basket cell to PV+ basket cell pairs (n=16) were fast (10-90% rise time, 0.63 ms; decay time constant, 3.17 ms) with short latency (0.76 ms), large amplitude (81.18 pA) and high transmission probability (p=1). The properties of inhibitory synapses among CCK+ basket cells (n=6) were similar to PV+ basket cell to PV+ basket cell synapses in 10-90% rise time (0.63 ms) and decay time constant (3.65 ms), however, uIPSCs were evoked with significantly longer latency (1.59 ms) and lower transmission probability (p=0.7). Finally, we found that synapses between CCK+ dendritic-region targeting interneuron pairs (n=4) had the slowest time course of rise time (0.98 ms), decay time (4.47 ms) and latency (1.52 ms), with the smallest amplitude (43.71 pA) and lowest transmission probability (0.55). The decay time constant, latency, amplitude and transmission probability of uIPSCs among CCK+ basket cell and CCK+ dendritic-region targeting interneuron pairs were similar, but the 10-90% rise time of uIPSCs mediated by CCK+ basket cells was significantly faster compared to CCK+ dendritic-region targeting interneuron pairs.

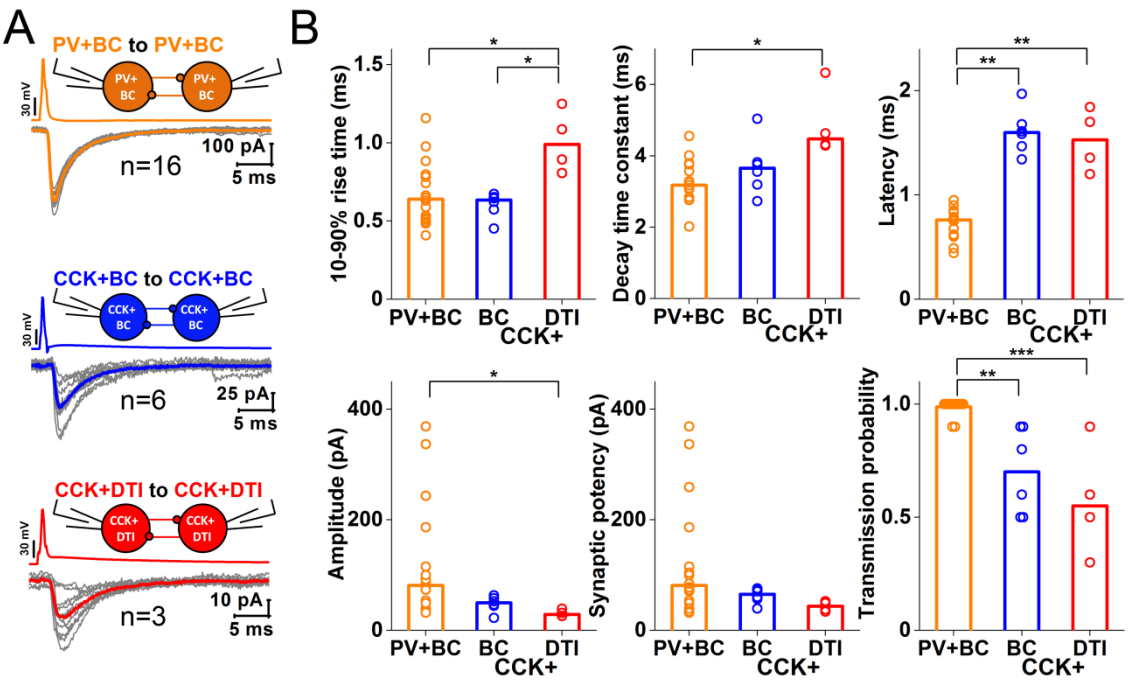

Figure 27: Differences in unitary IPSC properties in interneuron pairs. *A: Representative example of 10 superimposed single uIPSCs (gray) triggered by 10 single action potentials between homologous PTI and CCK+ DTI (red) pairs. Averages of uIPSCs are shown by the colored line. B: Representative example of*

DOI:10.14753/SE.2018.2077

10 superimposed single uIPSCs (gray) triggered by 10 single action potentials between homologous PTI and CCK+ DTI (red) pairs. Averages of uIPSCs are shown by the colored line.

VI.2.7. Short-term depression among PV+ basket cell pairs is frequency-dependent

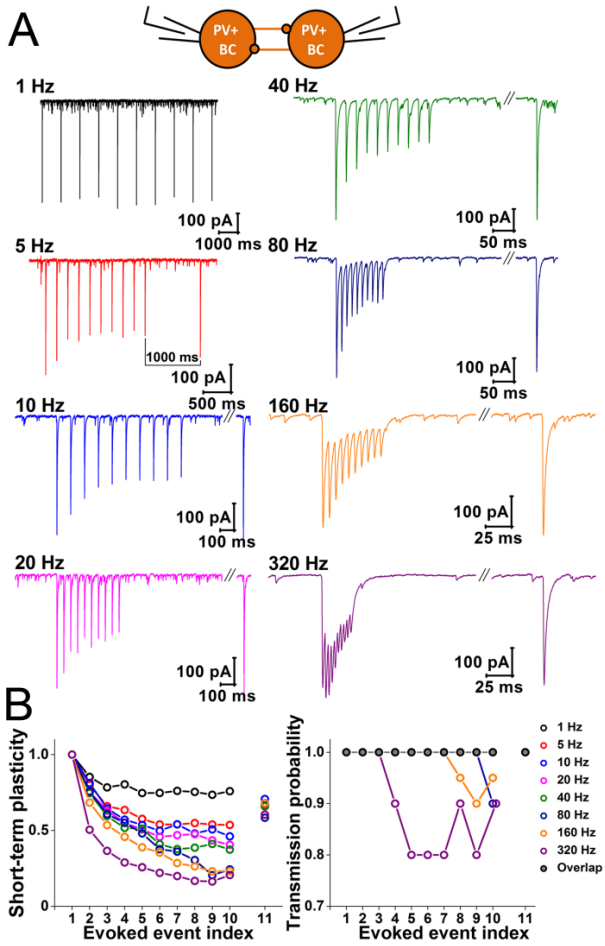

As we demonstrated above from the many possible inhibitory neuron intra- or inter-class connections only a limited subset is realized in the CA3 area. The most frequent was the reciprocal connection among PV+ basket cells.

To reveal the temporal properties of PV+ basket cell interactions, first we examined the properties of transmission by a train of 10 APs in the 1-320 Hz range (n=13), mimicking the possible range of physiological activation frequencies (Figure 28A). The transmission was characterized by STD (Figure 28B); the amplitude of triggered IPSCs decreased during the train of 10 APs at all frequencies. Moreover, the STD became more prominent as the frequency of stimulation was increased. We also found that the transmission probability started to decrease at 80 Hz stimulation (at the 10th AP to 0.9; fast gamma frequency range). Increasing the frequency of stimulation to 160 Hz (sharp wave-ripple frequency range), we observed 5-10% decrease of transmission probability at the 8th-10th AP, whilst at 320 Hz stimulation the inhibitory transmission became less effective between the 3rd and 10th AP (transmission probability between 0.8-0.9) (Figure 17B).

Figure 28: ***Properties of short-term plasticity between PV+BCs***. *A: Representative traces of averaged IPSCs from PV+BC to PV+BC pair, evoked by a train of 10 APs at frequencies 1, 5, 20, 40, 80, 160 and 320 Hz (to measure onset of short-term depression, STD), followed by an additional 11th AP after 1 s (to*

measure recovery from STD). B: Left: summary plot showing frequency-dependent STD of IPSCs (median of averaged values normalized by the amplitude of first IPSCs for each PV+BC to PV+BC pair), plotted against evoked events (APs) at each frequency.. The recovery from depression is also shown (normalized amplitude of 11th IPSC). Right: median value of transmission probability (TP) for each PV+BC to PV+BC pair, plotted against evoked events (APs) at each frequency. TP started to drop at stimulation frequencies 80 Hz and higher, and recovered by the time of the 11th stimulation.

To also measure the recovery from synaptic depression the train of 10 APs at frequencies 5-320 Hz was followed by an additional, 11th AP after 1s (Figure 28A). The amplitude of the triggered 11th IPSC was normalized to the amplitude of the first IPSC, and the result was plotted against the frequency of the preceding stimulation (Figure 28B). The 1 s interstimulus interval was not enough to completely recover synaptic depression and the level of recovery was similar, regardless of the previous train frequency (P_{KW}=0.152).

VI.2.8. Interactions among CCK+ interneurons show heterogeneous dynamics regardless of axonal location

We also tested the dynamic properties of transmission at CCK+ to CCK+ synapses, that, as shown above, were realized either between basket cell or dendritic-region targeting interneuron pairs, but were not seen among basket cells and dendritic region targeting interneurons. Similarly to PV+BC pairs, we evoked a burst of 10 APs in the presynaptic neuron at frequencies between 1-320 Hz, followed by an additional 11th AP after 1 s. Recordings were performed in the presence of 1 μM AM251 to block CB_1 receptor function to reveal the complete potential of transmission.

The transmission of CCK+ cells proved to be heterogeneous. Though STF was a common feature of all connections, 4 out of 9 cells evoked only synchronous transmitter release (Figure 29A_1), while 5 of them showed a frequency-dependent strong asynchronous release (Figure 29A_2). Both basket cells and dendritic-region targeting interneurons could show either of these patterns.

In contrast to STD of inhibitory currents between PV+ basket cells (Figure 28A-B), the amplitude of evoked IPSCs among CCK+ cells displayed STF at 10 Hz and 40 Hz

DOI:10.14753/SE.2018.2077

stimulation. On the other hand, the amplitude of individual IPSCs at 160 Hz stimulation was characterized by no consistent change, or by the mixture of STD and STF (Figure 29A_3). However, 2 cells responded to 10 Hz stimulation with delayed onset of synchronous release, appearing after the 6th and 7th AP with subsequent facilitation (data not shown). Our data indicate that the inhibitory dynamics among these CCK+ cells is variable during different stimulation trains, giving rise to frequency-dependent patterns of inhibition.

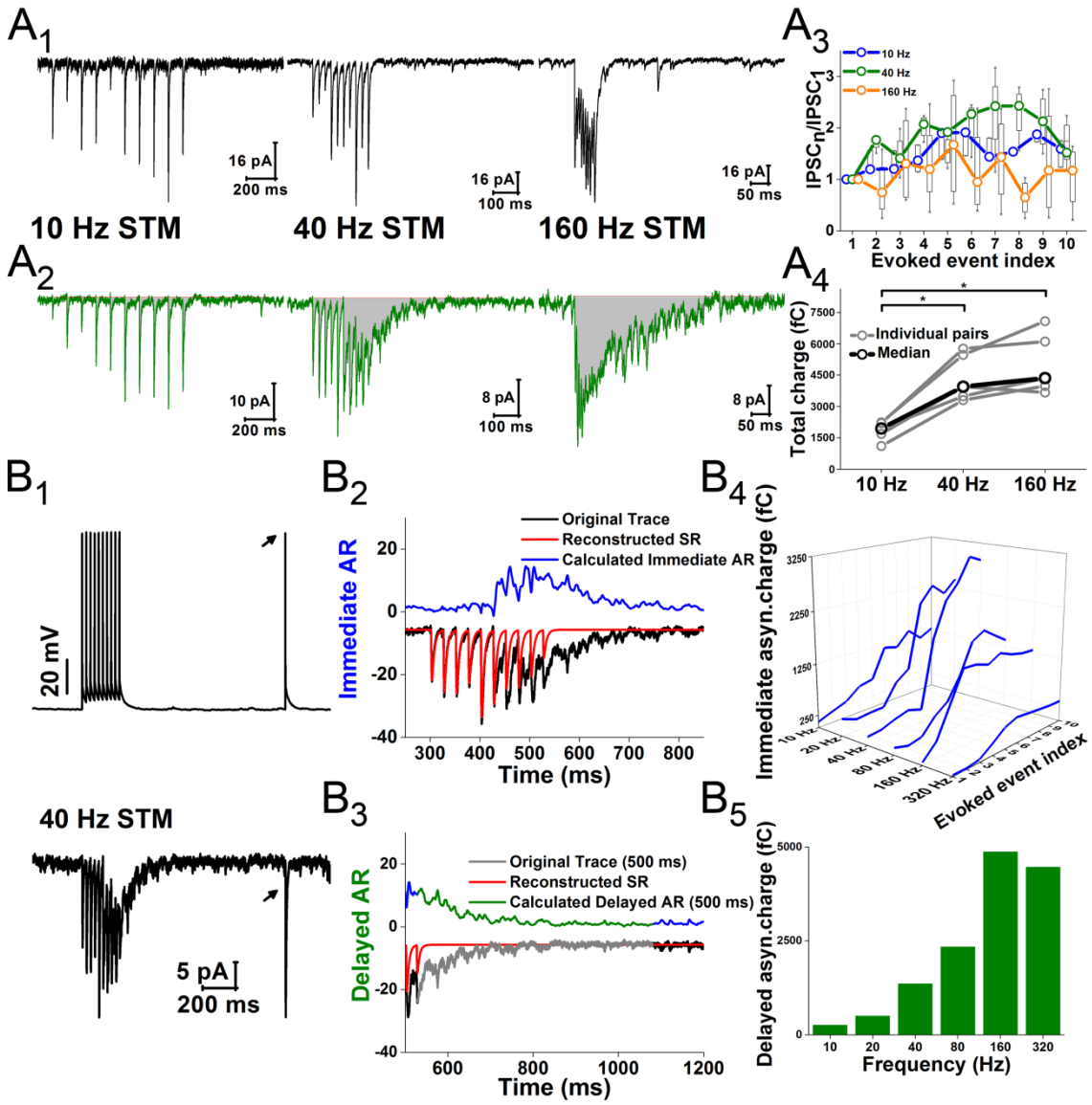

Figure 29: The CCK+ interneuron population represents a morphologically and physiologically heterogeneous group of cells*. A: CCK+ cell pairs were stimulated with a train of 10 APs at frequencies 1, 5, 20, 40, 80, 160 and 320 Hz, followed by an additional 11th AP after 1 s. Both CCK+BC and CCK+DTI pairs displayed two types of inhibitory transmission, without significant difference in the dynamics; therefore, the results from these groups are presented together. A_1: Four cell pairs (black) displayed synchronous inhibitory transmission at all frequencies, characterized by frequency-dependent short-term facilitation (A_2). A_3: In five cells (green), asynchronous release appeared at frequencies higher than 10 Hz. The total asynchronous charge (fC) was calculated from the area under the curve during the stimulation train and a 500 ms time period following the end of stimulation (grey area); A_4: Observed total charge was plotted against stimulation frequency. B_1: Some cells evoked both immediate (during the stimulation train) and delayed asynchronous release (after the end of stimulation train). To calculate immediate and delayed asynchronous charge, an artificial synchronous release was reconstructed (B_2, B_3, red line) from the rise time and exponential decay of averaged 11th uIPSC (black arrows); subsequently, the reconstructed synchronous release was subtracted from the original trace, and immediate (B_2) and delayed asynchronous charge (B_3) was calculated (displayed as mirror images for better visibility). B_4: Summary graph of immediate asynchronous charge at each AP plotted against stimulation frequencies. B_5:Summary graph of frequency-dependent delayed asynchronous charge. SR, synchronous release; AR, asynchronous release*

In 5 CCK+ to CCK+ cell pairs transmitter release was synchronous at 10 Hz stimulation, but at 40 Hz and 160 Hz stimulation asynchronous release (AR) appeared after the 5th AP (immediate asynchronous release). This asynchronous release persisted after the end of stimulation train, lasting between 69.8 and 339.6 ms for different cells (delayed asynchronous release). Its duration was independent of the frequency of stimulation train. However, the total inhibitory charge during the stimulation train (including a 500 ms window following the end of the 10th AP) was determined by the frequency of presynaptic APs (Figure 29A_4).

To quantify the contribution of immediate and delayed asynchronous release, we reconstructed synchronous release using the rise time and exponential decay of IPSCs triggered by the 11th AP (Figure 29$B_{1\text{-}3}$) (Daw *et al.*, 2009). To get immediate and delayed asynchronous charge, reconstructed synchronous release was subtracted from the original trace (Figure 29$B_{2,\,3}$). The observed immediate asynchronous charge at each AP (time window between neighboring IPSC; 10 Hz: 100 ms; 20 Hz, 50 ms; 40 Hz, 25 ms; 80 Hz, 12.5 ms; 160 Hz, 6.25 ms; 320 Hz, 3.125 ms) and delayed asynchronous charge (500 ms time window after the end of 10th AP) were plotted against frequencies (Figure 29$B_{4,5}$). As it is shown in Figure 29B_4, immediate asynchronous charge increased with increasing

frequency between 10 and 40 Hz, starting around the 5th AP. However, at higher frequencies, immediate asynchronous charge started to drop. One possible explanation of this phenomenon is the shorter time window between neighboring APs. Although the immediate asynchronous release is present at these frequencies, the temporal precision of two APs can be a limiting factor accounting for decreased immediate asynchronous charge at frequencies higher than 40 Hz. On the other hand, delayed asynchronous charge strongly potentiated in a frequency-dependent manner, and saturated at 160 Hz (Figure 29B$_5$).

These experiments showed that CCK+ cells are highly heterogeneous not only concerning their intrinsic properties (see above) but also in the temporal characteristics of their inhibitory transmission. CCK+ basket cells and dendritic-region targeting interneurons form an inseparable physiological continuum.

VI.2.9. Simple mathematical models of short-term plasticity effectively capture the temporal properties of transmission of different types of hippocampal interneurons

To obtain a compact description of our data regarding the short-term plasticity at the different types of connections characterized above, and to start revealing potential mechanisms, we considered and fitted to the data several different mathematical models of short-term synaptic plasticity. We considered only synchronous release in all cell types. The first model was the classic Tsodyks-Markram model (Tsodyks et al., 1998) of synaptic depression, which assumes that a given portion of the available synaptic resources is consumed by each presynaptic action potential, and these resources are then replenished at a certain fixed rate, while the average amplitude of the postsynaptic response is proportional to the amount of available synaptic resource when the presynaptic spike occurs. The second model was the version of the TM model which also attempted to capture synaptic facilitation by assuming that the portion of available synaptic resource used by a presynaptic action potential was variable, and increased transiently after each spike. The remaining two models were variations of the first two models (one purely depressing, and one including facilitation), and were based on a very similar formalism, except that they assumed that the rate at which synaptic resources were

replenished also depended on presynaptic activity such that the rate of replenishment was higher for larger action potential rates (Hennig, 2013).

We first fit each of these four models to the average amplitude of postsynaptic currents in response to presynaptic action potential trains at different frequencies (1-320 Hz) for four different types of connections described above (PV+ basket cell to pyramidal cell, AAC to pyramidal cell, CCK+ basket cell to pyramidal cell, PV+ basket cell to PV+ basket cell). Model parameters were optimized for each synaptic connection using data from all stimulation frequencies simultaneously. We found that PV+ basket cell to PV+ basket cell, PV+ basket cell to pyramidal cell and AAC to pyramidal cell connections showed qualitatively similar short-term plasticity. They were adequately described by the original depression model of Tsodyks and Markram without any significant facilitation; the fit could be further improved by assuming a use-dependent rate of replenishment for synaptic resources (see Figure 30A, C).

DOI:10.14753/SE.2018.2077

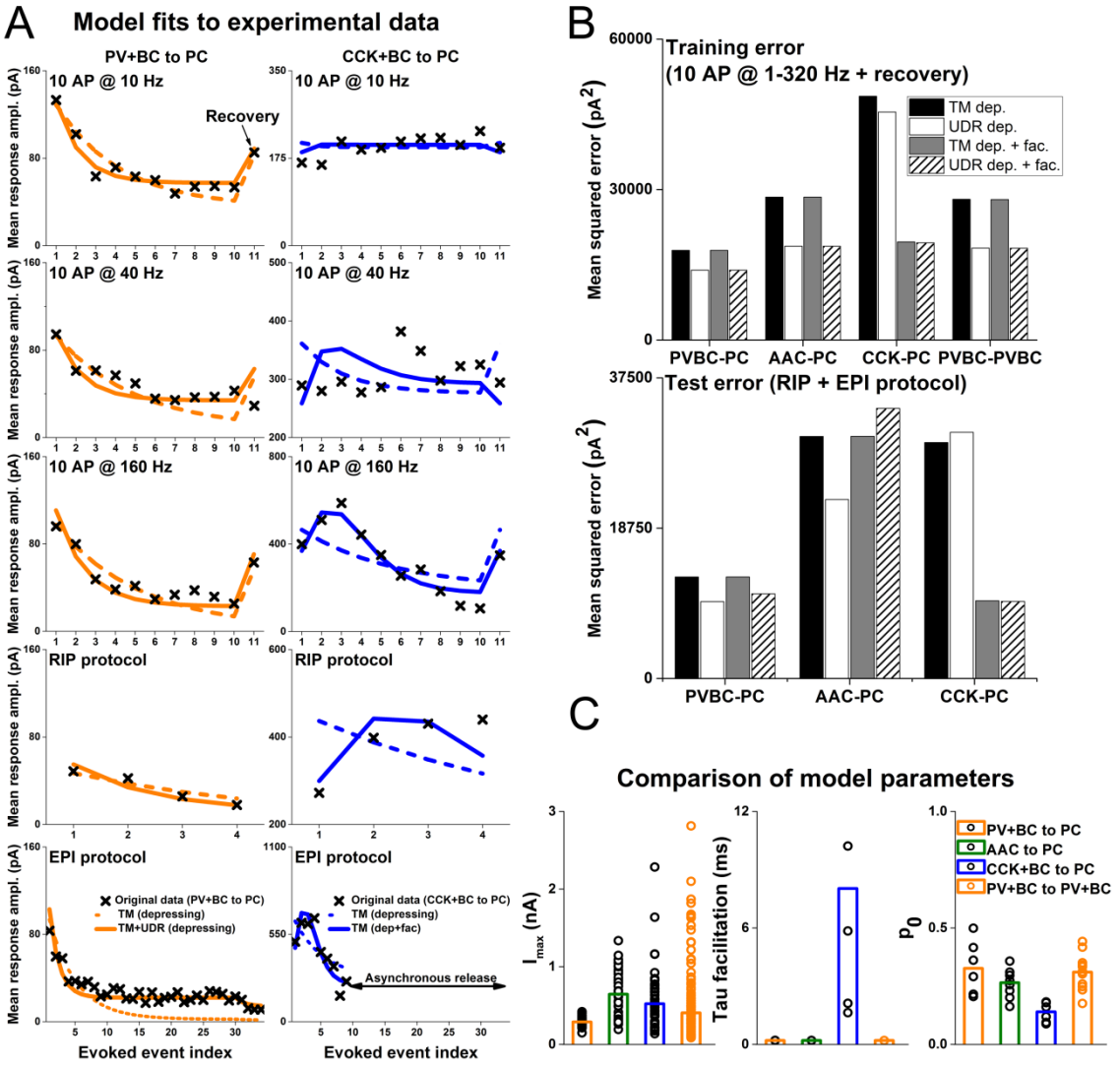

Figure 30: Phenomenological models of short-term synaptic plasticity provide good fits to the data. *A: Example fits to the mean experimental responses to trains of presynaptic action potentials in various patterns: 10 APs at different frequencies (10, 40, and 160 Hz are shown here) plus an additional spike after a fixed delay (1 s); the RIP and the EPI protocols as defined in Materials and Methods. The left column shows fits to data from a PV+BC-to-PC connection (crosses); the dashed line indicates the prediction of the best-fitting purely depressing model as defined originally by Tsodyks and Markram (TM), while the solid line shows the prediction of a (purely depressing) model which includes a use-dependent rate of replenishment of synaptic resources (UDR). In the right column of panel A, the data are from a CCK+BC-to-PC connection; the dashed line is the prediction of the purely depressing TM model, while the solid line indicates the prediction of a TM-type model which includes both depression and facilitation. Results from the 10-AP protocols (at up to eight frequencies) were used to tune the parameters of all models, while the data from the RIP and EPI protocols were used to test these models (with only the theoretical maximal response, A, treated as a free parameter). B: Comparison of the errors of four different models*

(with/without facilitation and with/without use-dependent replenishment) on the training data (10-AP protocols at various frequencies; top panel) and the test data (RIP+EPI protocols; bottom panel). C: Comparison between connection types of the best-fitting values of the three parameters (I_{max}, $\boldsymbol{\tau_f}$ and p_0) which were optimized independently for each cell. Circles indicate individual fitted values, and the bars show median values. Best-fitting values of parameters for which cell type-specific values were fit are as follows: PV+BC-PV+BC connections, $\boldsymbol{\tau_r = 1.08\ s}$, $\boldsymbol{\tau_e = 23.7\ ms}$, $\boldsymbol{a_e = 0.64}$, $\boldsymbol{\widetilde{k}_e = 13.2\ 1/s}$; *PV+BC-PC connections,* $\boldsymbol{\tau_r = 1.62\ s}$, $\boldsymbol{\tau_e = 13.5\ ms}$, $\boldsymbol{a_e = 0.72}$, $\boldsymbol{\widetilde{k}_e = 22.6\ 1/s}$; *AAC-PC connections,* $\boldsymbol{\tau_r = 1.70\ s}$, $\boldsymbol{\tau_e = 13.6\ ms}$, $\boldsymbol{a_e = 0.98}$, $\boldsymbol{\widetilde{k}_e = 24.7\ 1/s}$; *CCK+BC-PC connections,* $\boldsymbol{\tau_r = 12.9\ s}$, $\boldsymbol{\tau_e = 29.0\ s}$, $\boldsymbol{a_e = 0.57 \widetilde{k}_e = 12.5\ 1/s}$,.

Both models could capture some essential features of the data, such as the frequency-dependent gradual decrease of synaptic efficacy in the course of extended AP trains, and its recovery after a silent period. However, the model which included activity-dependent replenishment of resources captured the frequency-dependence of depression much better than the original TM model, resulting in a significantly smaller error of fit (the combined sum of squared error decreased by 35% for PV+ basket cell to PV+ basket cell connections, by 22% for PV+ basket cell to pyramidal cell connections, and by 34% for AAC to pyramidal cell connections when use-dependent replenishment was assumed). Adding synaptic facilitation to the model did not lead to any significant improvement for these three types of connection.

CCK+ basket cell to pyramidal cell pairs showed a different qualitative behavior (as CCK+ dendritic-region targeting interneuron to pyramidal cell pairs were less numerous and extremely heterogeneous, we did not analyze their behavior). The parameters of the best-fitting TM model indicated a significant degree of synaptic facilitation, and showed a better fit than the purely depressing model (Figure 30B, C). On the other hand, allowing the replenishment of resources to be use-dependent did not lead to a better fit for these connections (data not shown).

Table 6: Best-fitting parameters describing the short-term plasticity of different types of connection. *The three types of connection in the upper part of the table were best described by a model which included the use-dependent replenishment of resources but lacked facilitation (Equations 1, 3, 4, 5 in Materials and Methods). CCK+BC – PC connections (lower part of the table) were best described by a model which included short-term facilitation but not use-dependent replenishment (Equations 1, 2, and 5). Medians and*

interquartile ranges for each connection type are shown in the case of parameters for which connection-specific values were fit; the single best-fitting value is shown for connection type-specific parameters whose value was fit jointly for all connections within the given type.

Connection type	$P0$	τ_r **(ms)**	τ_e **(ms)**	a_e	$\tilde{k}_e$ **(1/s)**	I_{max} **(pA)**
PV+BC – PV+BC	0.31 (0.25, 0.34)	1080	23.7	0.64	13.2	410 (270, 710)
PV+BC – PC	0.33 (0.22, 0.42)	1620	13.5	0.72	22.6	289 (253, 333)
AAC – PC	0.26 (0.22, 0.30)	1700	13.6	0.98	24.7	646 (321, 828)
Connection type	U_0	τ_r **(ms)**	τ_f **(ms)**	I_{max} **(pA)**		
CCK+BC – PC	0.15 (0.11, 0.18)	71	10.9 (7.2, 53.5)	499 (252, 708)		

In order to verify that lower error values were not simply the result of the larger number of free parameters in the more complex models, we calculated the values of the Bayesian Information Criterion (BIC, which assigns larger penalties to models with more free parameters) for both models. The BIC clearly favored the purely depressing model which included use-dependent replenishment for PV+ basket cell to PV+ basket cell, PV+ basket cell to pyramidal cell and AAC to pyramidal cell connections, while the depressing-facilitating model (without use-dependent replenishment) provided the best fit for CCK+ basket cell to pyramidal cell connections. The parameters of the best-fitting model for each type of connections are shown in Table 6.

Statistical comparison of best-fitting short-term plasticity parameters in the most comprehensive model (including synaptic depression, facilitation, and use-dependent replenishment of resources) indicated some quantitative differences between the different types of connections (Figure 30C, Table 6). Specifically, the values of all parameters for which cell-specific or run-specific values were fitted showed connection type-specific differences (Kruskal-Wallis ANOVA; $p=0.0021$ for p_0, $p=0.0012$ for τ_f, and $p=5.8\times10^{-7}$ for I_{max}). *Post hoc* comparisons indicated that, as expected from the model comparison results above, best-fitting values of τ_f were significantly larger for CCK+ basket cell to pyramidal cell connections than for any of the connections involving PV+ interneurons ($p<0.001$ for AAC to pyramidal cell, $p<0.01$ for PV+ basket cell to pyramidal cell, and $p<0.05$ for PV+ basket cell to PV+ basket cell connections). In addition, best-fitting values of p_0 were significantly smaller for CCK+ basket cell to pyramidal cell connections than those for PV+ basket cell to PV+ basket cell and PV+ basket cell to pyramidal cell connections (both $p<0.01$), and Imax values were significantly smaller for PV+ basket

cell to pyramidal cell connections than for any of the other three types of connection (all $p<0.001$).

Finally, we verified how well the best-fitting models based on the 8-frequency protocol could predict the behavior of these same synapses in response to physiological (RIP) and pathological (EPI) presynaptic spiking patterns. We found that purely depressing models (with use-dependent replenishment) predicted the behavior of PV+ basket cell to PV+ basket cell, PV+ basket cell to pyramidal cell, and AAC to pyramidal cell synapses well also for natural activity patterns, while the behavior of CCK+ basket cell to pyramidal cell connections was best described by depressing-facilitating models of short-term plasticity (Figure 30A, B).

VI.2.10. Possible physiological significance of short-term plasticity in sharp wave-ripple generation

Our previous study (Schlingloff et al., 2014) revealed that inhibitory synaptic currents mediated by PV+ basket cells in the CA3 region of hippocampus are necessary and sufficient current and rhythm generators of physiological SWRs *in vitro*. In addition this work uncovered that spontaneous SWRs did not restart within a 200-300 ms time window, and the presence of this refractory mechanism may be an important element of SWR generation.

Here, we wanted to examine the potential importance of short-term dynamics of inhibitory transmission of PV+ basket cells in SWR initiation. To this end, in a modified submerged *in vitro* chamber (Hájos et al., 2009) we recorded SWRs in the CA3 region of hippocampal slices, and we plotted the amplitude of SWRs as a function of the time measured from the preceding SWRs (Figure 31A). Similar to that reported in Schlingloff *et al.* (2014) we found that there was a minimum time between SWRs, corresponding to an absolute refractory period (~200 ms). Plotting the relationship between the amplitude of SWRs and the time since the previous SWR revealed that the amplitude recovered with a half-time of 501.8 (374.2; 699.3) ms (Figure 13A). This recovery was close to the recovery half-time of PV+ basket cell to pyramidal cell IPSCs (495.8 (343.6; 648.0) ms) (Figure 31B) (For more details see Figure 20).

DOI:10.14753/SE.2018.2077

The phenomenon of gradual recovery was also visible in optogenetic experiments, where we used transgenic mice expressing light-activated ion channel channelrhodopsin-2 in PV+ cells (Schlingloff et al., 2014). In these experiments we found that optogenetic driving of PV+ cells evoked spontaneous-like SWRs and that the amplitude of SWRs evoked by a 10 ms-long light illumination depended on the gap since the previous spontaneous SWR (Figure 31C) (see Schlingloff *et al.*, 2014).

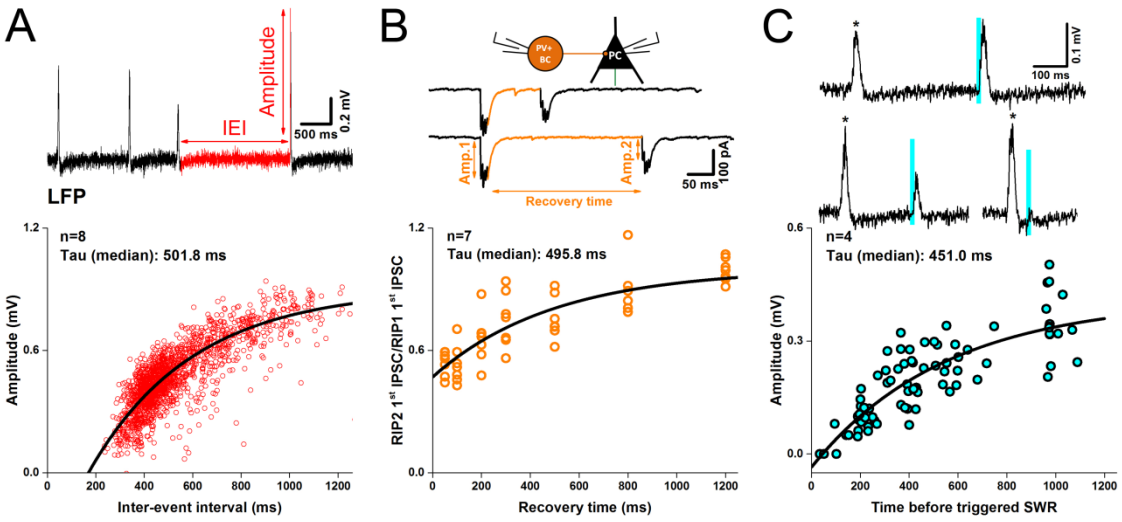

Figure 25. Recovery of transmission at PV+ basket cell synapses can be a refractory mechanism of sharp wave-ripple generation. *A: Plotting the interaction between the amplitude of spontaneous SWRs and the time since the previous SWR shows that SWR amplitude recovers with a half-time similar to the recovery half-time of transmission between PV+ basket cells and pyramidal cells (B). The recovery of transmission was calculated from 2 sets of RIP protocols (4 APs at 160 Hz with interstimulus interval between 50 and 1200 ms), and recovery ratio of evoked IPSCs was calculated by dividing the amplitude of the first IPSC of the second train by the amplitude of the first IPSC of the first train, and plotted against inter-stimulus interval. C: Top: optogenetic stimulation of PV+ cell population evoked SWRs (blue bars, 10 ms illumination) between spontaneous SWRs (asterisks). The amplitude of the evoked SWR depended on the time period between the spontaneous SWR (asterisk) and stimulation onset. Bottom: Plotting the interaction between the amplitude of evoked SWR and the time since the previous spontaneous SWR revealed that the amplitude of light-evoked SWRs depends on the gap since the previous spontaneous SWR. Note the absence of SWRs (full refractoriness) in the 200 ms window following the spontaneous SWR.*

The shorter the time, the smaller the amplitude of light-triggered SWR was, and at short intervals (less than 100 ms) no SWRs could be evoked. Moreover, the recovery half-time of light-evoked SWRs (451 (300.3; 570.6) ms) was similar to the recovery half-time of

DOI:10.14753/SE.2018.2077

spontaneous SWR amplitude and recovery half-time of IPSCs between PV+ basket cell-pyramidal cell pairs.

These results suggest that the recovery of transmission at PV+ basket cell synapses could contribute to the refractory time in the SWR initiation process.

DOI:10.14753/SE.2018.2077

VII. DISCUSSION

The studies presented in this thesis investigated the differences between *in vitro* physiological sharp wave-ripples and interictal-like events. Moreover, with the intention to provide precise data suitable to build neuronal network models and to understand the mechanisms underlying the generation of different network dynamics, we have described quantitatively and qualitatively the connectivity and temporal properties of inhibitory synaptic transmission among identified PV+ and CCK+ interneuron – pyramidal cell/interneuron pairs in the CA3 region of hippocampus. To this end, we used spike trains observed during different network states, under *in vivo*-like conditions (350-450 μm thick hippocampal slices perfused with artificial '*in vivo*-like' ACSF).

VII.1. Part I

VII.1.1. In vitro sharp wave-ripples and high extracellular potassium induced interictal-like events are different network phenomena with distinct properties.

Though the local field potential signal of sharp wave-ripples and interictal-like events may look similar in shape, they differ in several features, including their amplitude, duration, accompanying multi-unit activity and firing pattern of neurons. We proved that interictal-like events never evolve directly from sharp wave-ripples, but are separated by transitory phase. This highly active state characterized by featureless EEG activity is similar to transitory phase of other *in vitro* epilepsy models induced by decreasing GABAergic inhibition (Cohen et al., 2006), adding 4-aminopyridine (Perreault and Avoli, 1991), omitting Mg^{2+} (Whittington et al., 1995) or decreasing extracellular Ca^{2+} concentration (Bikson et al., 2003). Our results strengthen the hypothesis that SWRs and IIEs represent different types of network activity. When the population activity reached a critical level, a new type of synchrony (interictal-like events) appeared in our slices, similar to results published earlier. Our results also support the finding of Brunel & Wang (2003), that these two types of transient synchrony are mutually exclusive, and the changes of excitatory and inhibitory transmission parameters could switch the network

dynamics from one type of oscillation to a mechanistically different one with an unorganized/asynchronous state in between.

VII.1.2. The inhibitory control especially from parvalbumin-positive basket cells fails during interictal-like events

We have shown that during interictal-like events all neuron types increase their firing rate compared to sharp wave-ripples. However, the firing of PV+ basket cells and some axo-axonic cells stops as a result of depolarization block before the peak of interictal-like events. An important finding of our study is that during interictal-like events the firing of PV+ basket cells and pyramidal cells are complementary: pyramidal cells start firing when PV+ basket cells get into depolarization block.

Intracellular recordings revealed that sharp wave-ripples (Hájos et al., 2013; Schlingloff et al., 2014) and interictal-like events are preceded by a build-up of depolarizing potentials, indicating increasing excitatory neuron activity. During interictal-like events, with the increase of excitation, inhibitory population (and especially PV+ basket cells and axo-axonic cells) start to be activated. However there is a level of excitatory drive where PV+ basket cells enter into depolarization block and the build-up of excitation enters a state when pyramidal cells start to fire. Moreover, even when action potentials are generated, GABA release from PV+ basket cells is strongly decreased, the short-term depression of inhibitory postsynaptic currents on pyramidal cells is increased. Although dendritic region-targeting interneurons and CCK+ basket cells keep firing with increasing frequency and their transmission is potentiated, it seems that they cannot control the runaway firing of pyramidal cells during interictal-like events. Thus, short-term plasticity can strongly affects the neural dynamics, and the changes of transmission parameters and short-term dynamics can lead to the reorganization of the network activity.

During interictal-like events, PV+ basket cells and axo-axonic cells reach higher depolarization compared to other cell types. The conditions leading to depolarization block likely depend on the properties and densities of spike-generating currents (including the voltage-dependence and kinetics of channel activation and inactivation), and may be also influenced by slower currents. It is known that the involvement of sodium

channels and persistent sodium currents is crucial in the evolution of depolarization block (Bikson et al., 2003), and the properties of Na^+ and K^+ channels are different in PV+ basket cells and pyramidal cells. Another important factor determining whether depolarization block occurs is the net input synaptic current received by the neuron. We showed that PV+ basket cells and axo-axonic cells receive higher depolarization than other cell types. This can be explained by different density as well as the total number of excitatory and inhibitory synapses on these cell types. It has been shown by Gulyás *et al*, (1999), that PV+ cells receive high number of excitatory inputs (~15.000) balanced with weak inhibition (~6%) compared to CCK+ basket cells (~5000 excitatory inputs balanced with 35% inhibition) and dendritic region-targeting interneurons (~2900 excitatory inputs balanced with 29% inhibition) (Mátyás et al., 2004a). However, pyramidal cells also receive a large amount of excitatory inputs (~30.000) balanced with 5.3% inhibition (Megías et al., 2001), but they do not get into depolarization block during interictal-like events. One of the reasons for this is the different input organization of PV+ basket cells and pyramidal cells. Whilst PV+ basket cells receive primarily perisomatic and somatic excitatory inputs, the excitatory inputs of pyramidal cells terminate primarily on distal spiny dendrites (Gulyás et al., 1999; Megías et al., 2001). It has been shown that in neurons devoid of perisomatic excitation, the soma and the axon are electronically distant, and may not undergo the same depolarization as neurons with perisomatic excitatory input (Rancz and Häusser, 2010). In addition, PV+ basket cells have a more compact dendritic tree with thicker dendrites (on average) than pyramidal cells, making PV+ basket cells (and interneurons) more compact than pyramidal cells (Brown et al., 1981; Emri et al., 2001; Gulyás et al., 1999; Mátyás et al., 2004a, 2004b; Megías et al., 2001), and can result in a more effective integration of dendritic inputs arriving onto PV+ basket cells. Thus, a unique combination of intrinsic membrane properties, cellular and connectivity parameters in PV+ basket cells may act synergistically to explain the presence of depolarization block during interictal-like events. The enhanced excitation effectively activates pyramidal cells (without depolarization block), and without the spiking of PV+ basket cells (because of depolarization block) the network activity increases.

DOI:10.14753/SE.2018.2077

VII.1.3. The changes of cellular and network parameters underlie the transition from sharp wave-ripple generating state to high K^+ induced interictal-like event generation state

Based on the observed results (long-term changes of cellular and network parameters in high K^+, changes in firing patterns of hippocampal neurons, changes in inhibitory transmission and short-term plasticity) and studies demonstrating that interneurons become activated at different time points of interictal-like events (Spampanato and Mody, 2007; Trevelyan et al., 2006; Ziburkus et al., 2006), we suggest the following sequence of interictal-like event evolution:

1. Initiation stage: similar to sharp wave-ripples, the excitatory activity starts to build up gradually at the beginning of an interictal-like event. Because of the high K^+ application, the balance between excitation and inhibition is shifted towards excitation. Although inhibition is still present in the phase (PV+ basket cells and axo-axonic cells increase their firing rate), it cannot restrain the excitation from building-up further in the CA3.
2. Pyramidal cell firing / high frequency stage: the network activity increases beyond the physiological level, perisomatic inhibition fails through different synergistic mechanisms (the depolarization block of PV+ basket cells and some axo-axonic cells, decreased inhibitory transmission, increased short-term depression of postsynaptic inhibitory currents), pyramidal cells start to fire at high frequency, manifesting as high frequency oscillation in the local field potential. At this point, the perisomatic inhibitory transmission is collapsed, and synchronous postsynaptic potentials do not contribute to local field potential generation.
3. Termination stage: in this stage the pyramidal cell firing accommodates and starts to slow down, whereas PV+ basket cells are still in depolarization block. As pyramidal cells fire less, inhibition regains control and terminates interictal-like events. Paradoxically, the depolarization block of PV+ basket cells (evidently a refractory mechanism) can help terminate interictal-like events, as while the cells are not firing, their inhibitory transmission might recover from the strong depression, and when the cell starts to fire again, the provided

inhibition is effective. Most probably several refractory mechanisms are present at the end of the third phase.

VII.2. Part II

VII.2.1. Clustering based on single-cell electrophysiological properties can reliably separate PV + cells from CCK + cells and PV + BCs from AACs.

We showed that multidimensional analysis of physiological features can be used to separate many, but not all cell types without the need of anatomical identification. Hopefully, this can help to select marker molecules to separate PV+ basket cells from AACs that proved to be a notoriously difficult task. The differences in the membrane properties of PV+ and CCK+ cells match their transmission properties, i.e. fast and precisely firing PV+ cells evoke reliable and quick IPSCs, while the slower, accommodating CCK+ cells evoke slower, often asynchronous IPSCs (Hefft & Jonas, 2005; Glickfeld & Scanziani, 2006; Szabó *et al.*, 2010).

*VII.2.*2. Interneurons of the same class (except AACs) tend to form reciprocally connected subnetworks.

We showed that interneurons tend to form functional synapses within the same class (Chamberland & Topolnik, 2012; Pfeffer *et al.*, 2013). The strongest (often reciprocal) interaction was found between PV+ basket cells, followed by CCK+ dendritic-region targeting interneuron and CCK+ basket cell pairs. We found unidirectional connections from PV+ basket cells to AACs. This is predictable from anatomy since PV+ basket cell axons terminate near the somata of PV+ basket cells and AACs, while the axons of AACs do not terminate in the layer where PV+ basket cell axon initial segments are located (unlike PC axon initial segments that run towards str. oriens, PV+ basket cell axon initial segments mostly run towards str. radiatum) (Gulyás et al., 1993b; Miles et al., 1996b).

The reciprocal synaptic interaction between PV+ basket cells plays a crucial role in the generation of SWRs: the tonic excitatory envelop of PCs drives reciprocally

connected PV+ cells, which synchronize their firing and generate ripple-frequency oscillation (Schlingloff et al., 2014). The one-way connection from PV+BCs to AACs suggests that AACs cannot contribute to rhythm generation, but can help to phase lock PC firing.

The reciprocal connection among CCK+ cells might be important in promoting their coordinated firing (Ali, 2007; Freund and Katona, 2007). Dendritic-region targeting interneurons make multiple single synapses on second order dendrite of PCs (Gulyás et al., 1993b; Miles et al., 1996b). Therefore dendritic inhibition on a PC can be more effective if inhibitory inputs from several different dendritic cells are activated simultaneously (Miles et al., 1996b).

We also reported here for the first time the functional connectivity between PV+ basket cells and CCK+ perisomatic-region targeting interneurons. It is important to note that Karson *et al.* (2009) provided ultrastructural evidence of synapses among PV+ and CCK+ interneurons; however, anatomical connections do not necessarily mean physiological interactions.

VII.2.3. The identity of both the pre- and postsynaptic cells influences inhibitory transmission and its temporal properties

Unitary IPSC properties were both pre- and postsynaptic cell type specific (Szabó *et al.*, 2010; Savanthrapadian *et al.*, 2014). In contrast, short-term plasticity trends proved to be dependent on the presynaptic, but not on the postsynaptic cell type. A different rule has been observed in the case of PCs, where transmission properties depended on the identity of the postsynaptic neuron (Losonczy et al., 2004; Reyes et al., 1998).

IPSCs of PV+ basket cells and AACs arriving onto interneurons and PCs proved to be significantly larger, faster and more reliable than CCK+ cell IPSCs. IPSCs from the same presynaptic cell type were always faster in interneurons than in PCs. Differences in $GABA_A$ receptor number , subunit composition and kinetics (Hájos and Mody, 1997; Nyíri et al., 2001; Takács et al., 2014; Thomson et al., 2000), as well as in the propagation of signals in PC versus interneuron dendrites can be responsible for the observed difference in the speed and amplitude of events. PV+ cells and CCK+ cells have a more compact dendritic tree with thicker dendrites (on average) than PCs. The diameter of the

prevalent dendrites falls in the 0.8-2.0 um range for PV+ and CCK+ cells (Gulyás et al., 1999; Mátyás et al., 2004a, 2004b), while in case of PCs the majority of the dendrites are second order oblique spiny dendrites which have a diameter of 0.3-0.7 um. This makes interneurons electrotonically more compact than PCs (Brown et al., 1981; Emri et al., 2001; Nörenberg et al., 2010).

The rapid and effective IPSCs evoked by PV+ interneurons have matching temporal properties: they show an initial strong transmission followed by short-term depression. This enables them to be activated by quick transients and evoke a precise, accurately timed inhibition (Bartos *et al.*, 2002; Szabó *et al.*, 2010; Gulyás *et al.*, 2010). In contrast, CCK+ cells, expressing strong short-term facilitation and often asynchronous release, are imprecise, slow integrators with a wide time window. Thus as we showed inhibition from CCK+ cells is significantly weaker during a transient event such as SWRs than inhibition originated from PV+ cells. These features match the findings of Glickfeld & Scanziani (2006) and support the view of Freund & Katona (2007) that PV+ cells might be responsible for precise time keeping, while CCK+ cells more for modulation and slow integration.

To pursue the molecular mechanism behind the differences of the release patterns is beyond the scope of the discussion of our results, but differences had been shown in the Ca^{2+} metabolism and release machinery for the two cell types (Hefft and Jonas, 2005; Lee et al., 2009; Lenkey et al., 2015).

VII.2.4. Heterogeneities in the release properties of CCK+ interneurons

The transmission of CCK+ cells is not precise, but has a wide integration window. Furthermore, we observed differences in the extent and activation requirements of synchronous and asynchronous release. Some cells showed purely synchronous release, while other cells synchronous and asynchronous release (Losonczy *et al.*, 2004; Daw *et al.*, 2009; Ali & Todorova, 2010; Szabó *et al.*, 2010). Further degrees of freedom were the requirement for the activation of synchronous and asynchronous release and the timing of early and delayed asynchronous release. Different numbers of APs or critical frequencies were needed to start synchronous and/or later asynchronous release in different neurons. Some cells did not transmit even synchronous release below a given

spiking frequency or without a previous high-frequency burst (Figure 13). Even in the presence of CB_1 antagonist AM251, 50% of CCK+ dendritic-region targeting interneuron-PC pair synapses were found to be silent during physiological, low- and high-frequency stimulations and turned on only at the pathological EPI protocol. We believe that the heterogeneity was not due to arbitrary variability in slice preparation, since we observed different release properties in reciprocally connected CCK+ cell pairs. Although we found that the synchronous release of PV+ and CCK+ cells could be captured using relatively simple mathematical models, it seems that more complex models would be required to describe the cell-specific mixed synchronous and asynchronous release of CCK+ cells.

While PV+ cells separated into AACs and basket cells along both of their membrane properties and somewhat along their transmission properties (Papp et al., 2013), the properties of CCK+ cells associated arbitrarily, matching the findings of Pawelzik *et al.* (2002) and Szabó *et al.* (2014). CCK+ cells formed an undividable continuum, even if multidimensional methods were used (considering their morphologies, membrane and transmission properties). The observed heterogeneity suggests that different cells switch on (both firing and release) at different levels and pattern of activity (Lasztóczi et al., 2011). Thus the cumulative response curve of the CCK+ cell-driven inhibition upon excitation is much less a step function than in the case of PV+ cells, rather a shallow sloped sigmoid. As shown by Aradi *et al.* (2004), these types of heterogeneities can provide a subtle and robust control for PCs activity at different levels and patterns of excitation.

VII.2.5. Physiological relevance of inhibitory dynamics among interneurons and their target cells in different network states

The measurement of exact transmission parameters in different circumstances is essential to understand network behavior. For example, it has been shown by Gulyás *et al.* (2010) that the generation of somatic action potentials in a presynaptic neuron does not always mean that transmitter is released from its axon terminals. Subcortical modulation and ongoing activity influences transmission: elevated cholinergic tone (used to induce gamma oscillation *in vitro*) almost fully eliminated IPSCs of CCK+ basket cells

onto pyramidal cells (Gulyás *et al.*, 2010). Similarly, an elevated extracellular K^+ level (8.5 mM), which triggers pathological interictal-events *in vitro,* increased short-term depression to the extent that inhibitory postsynaptic currents at PV+ basket cell-pyramidal cell pairs were completely eliminated already at the beginning of a presynaptic burst.

In this study we also showed that the short-term depression observed in connections from PV+basket cells to pyramidal cells (Galarreta and Hestrin, 1998; Kraushaar and Jonas, 2000; Szabó et al., 2010) and to other PV+ basket cells (Bartos et al., 2002), might be the critical refractory mechanism participating in SWR generation (Schlingloff et al., 2014; Stark et al., 2014). Thus, the short-term dynamics of inhibitory transmission mediated by PV+ basket cells is significantly contributing to the generation of hippocampal oscillation, and the changes of ongoing activity can influence transmission (Gulyás et al., 2010)

DOI:10.14753/SE.2018.2077

VIII. CONCLUSIONS

The main goal of this thesis was to describe the differences between physiological sharp wave-ripples and pathological, high K^+ induces interictal-like events, and to reveal possible mechanisms resulting in the transition from physiological to pathological hippocampal network states. We also described quantitatively and qualitatively the connectivity and temporal properties of inhibitory transmission between monosynaptically connected perisomatic- and dendritic-region targeting interneurons and their pyramidal cell and interneuron targets, using spike trains observed during different network events and in circumstances reflecting *in vivo* conditions.

Comparing physiological sharp wave-ripples and pathological, high K^+ induced interictal-like events, we found that (1) sharp wave-ripples and interictal-like events are different transient high activity events and exclude each other. (2) During interictal-like events all neurons fire with an increased firing rate compared to sharp wave-ripples. (3) The firing of PV+ basket cells and some axo-axonic cells stops as a result of depolarization block before the peak of the event. (4) During interictal-like events the firing of PV+ basket cells and pyramidal cells is complementary, pyramidal cells start firing when PV+ basket cells get into depolarization block. Dendritic region-targeting interneurons fire strongly during all phases of the interictal-like events. (5) In the high K^+ model of epilepsy the balance of excitation to inhibition is shifted: inhibitory transmission is decreased and the short-term depression of postsynaptic inhibitory currents is increased. The integrative properties of pyramidal cells also change, resulting in higher excitability.

Investigating the connection trends and inhibitory transmission among interneurons and their pyramidal cell and interneuron targets we found the following: (1) clustering based on single-cell electrophysiological properties can reliably separate PV+ cells from CCK+ cells and PV+ basket cells from axo-axonic cells. CCK+ basket cells and CCK+ dendritic region-targeting interneurons form an inseparable continuum. (2) Interneurons of the same class (except axo-axonic cells) tend to form reciprocally connected subnetworks. PV+ basket cells innervate axo-axonic cells unidirectionally. (3) The identity of both pre- and postsynaptic cells influence inhibitory transmission and its temporal properties. IPSCs onto interneurons are quicker than onto pyramidal cells.. (4)

The transmission provided by PV+ cells is reliable, effective and precise, and its temporal features can be grabbed by a model incorporating synaptic depression. (5) The transmission of CCK+ cells is less reliable compared to PV+ basket cells and axo-axonic cells, and a model incorporating both synaptic depression and facilitation is required to grab it. (6) We present a simple mathematical description of the transmission for PV+ and CCK+ interneurons and provide the necessary parameters to calculate transmission for arbitrary action potential sequences. (7) The recovery of transmission at PV+ basket cells synapses could be an essential component of the refractory mechanism between sharp wave-ripples, influencing their initiation.

Our data indicate that (1) the collapse of perisomatic inhibition provided by PV+ cells (including altered short-term dynamics) and the altered balance between inhibition and excitation toward excitation appears to be a crucial factor in the emergence of pathological events. (2) Hippocampal interneurons in *in vivo*-like condition show target-specific transmission with distinct temporal features. As a consequence of short-term plasticity, the synaptic transmission depends on the pattern of recent network activity. However, to understand the generation of different behavioral-associated network activities, the transmission characteristics of all possible cell type combination has to be characterized, for each specific condition (taking into account the modulatory transmitter level), with the appropriate *in vivo* observed presynaptic action potential sequences.

DOI:10.14753/SE.2018.2077

IX. SUMMARY

The hippocampus exhibits a wide variety of behavior-associated rhythmic activities, determined primarily by the interaction of excitatory cells and different types of interneurons. Sharp wave-ripples and interictal-like events are physiological and pathological manifestations of hippocampal oscillations with similar feature. In order to understand the generation of activity patterns the underlying mechanisms have to be uncovered in both physiological and pathological states.

One goal of this thesis was to reveal the differences between sharp wave-ripples and interictal-like events. To this end, in *in vitro* hippocampal slices, we induced transition from sharp-wave ripple to interictal-like event generating state. We investigated the basic properties of local field potential, firing properties of hippocampal neurons, as well as the inhibitory transmission and short-term dynamics provided by perisomatic region-targeting interneurons. We found, that sharp wave-ripples and interictal-like events are different forms of high activity states. During interictal-like events neurons increased their firing, however, PV+ basket cells and pyramidal cells showed complementary firing. The excitatory transmission was enhanced whereas inhibitory transmission and dynamics was compromised. Thus, the collapse of perisomatic inhibition appears to be a crucial factor in the emergence of interictal-like events.

A second goal was to quantitatively and qualitatively capture the dynamics of inhibitory transmission at PV+ and CCK+ interneurons and their pyramidal cell and interneuron targets in *in vivo*-like condition. We found that the identity of both pre- and postsynaptic cells influences the transmission and its temporal properties. Our data also indicate that PV+ cells might be responsible for precise time keeping, whereas CCK+ cells are more responsible for modulation and slow integration. Finally, we have shown that the short-term depression observed among PV+ basket cells and pyramidal cells might be a critical refractory mechanism participating in sharp wave-ripple generation.

The findings presented in this thesis may further increase our understanding of the involvement of particular cell types in physiological and pathological oscillatory activities.

DOI:10.14753/SE.2018.2077

X. ÖSSZEFOGLALÁS

A hippokampusz számos viselkedésfüggő ritmikus aktivitásmintázatot mutat, melyek kialakításában nagy szerepet játszik a serkentő- és gátlósejtek közti egyensúly. A fiziológiás éleshullám-fodor aktivitás, valamint a kóros interiktális esemény hasonló tulajdonságokkal rendelkező oszcillációk. Hogy megértsük, hogyan jönnek létre ezek az aktivitásmintázatok, elengedhetetlen a mögöttük húzódó hálózat- és sejtszintű folyamatok feltárása mind fiziológiás, mind kóros állapotban.

Kutatásaink első felében arra kerestük a választ, miben is különbözik az éleshullám-fodor aktivitás és az interiktális esemény. Ennek érdekében *in vitro* szeletpreparátumban a spontán éleshullám-fodor aktivitást generáló állapotból interiktális aktivitást generáló állapotot váltottunk ki, és vizsgáltuk az egyes hálózati és sejtszintű változásokat. Ezen kísérletek feltárták, hogy az éleshullám-fodor aktivitás és interiktális esemény magas szinkronitást mutató, azonban egymást kölcsönösen kizáró aktivitásmintázatok. Az interiktális aktivitás alatt a sejteket megnövekedett tüzelés jellemezte, azonban a PV+ kosársejtek és piramissejtek tüzelése a kóros aktivitásmintázat más-más fázisára volt jellemző. Megfigyeltük, hogy míg a serkentő szinaptikus áramok megnövekedtek, addig a sejtekre érkező gátlás lecsökkent, valamint a gátlósejtek által közvetített szinaptikus kimenetek mind amplitúdóban, mind dinamikában változtak. Eredményeinkből megállapítható, hogy a periszomatikus gátlás gyengülése egy kritikus faktor az interiktális rohamok kialakulásában.

A tézis második felében a PV+ és CCK+ sejtek által létrehozott gátló jelátvitel dinamikájának kvantitatív és kvalitatív tulajdonságait tártuk fel *in vivo* állapotra jellemző körülmények között. Megfigyeltük, hogy a gátló jelátvitel tulajdonságait a pre- és posztszinaptikus sejttípus is befolyásolja. Eredményeink azt sugallják, hogy míg a PV+ sejtek a precíz időzítésért, addig a CCK+ sejtek a lassú integráció modulációjáért felelősek. Szintén megállapítható, hogy a PV+ kosársejtek és piramissejtek közti gátló jelátvitelben megfigyelhető rövidtávú szinaptikus depresszió hozzájárul az egymást követő éleshullám-aktivitás időzítéséhez.

A disszertációban bemutatott eredmények elősegíthetik az egyes idegsejt típusok szerepének megértését a hippokampális egészséges és kóros aktivitásmintázatok kialakításában.

XI. REFERENCES

Abbott, L.F., and Regehr, W.G. (2004). Synaptic computation. Nature *431*, 796–803.

Acsády, L., Görcs, T.J., and Freund, T.F. (1996). Different populations of vasoactive intestinal polypeptide-immunoreactive interneurons are specialized to control pyramidal cells or interneurons in the hippocampus. Neuroscience *73*, 317–334.

Ali, A.B. (2007). Presynaptic Inhibition of GABAA receptor-mediated unitary IPSPs by cannabinoid receptors at synapses between CCK-positive interneurons in rat hippocampus. J. Neurophysiol. *98*, 861–869.

Ali, A.B., and Todorova, M. (2010). Asynchronous release of GABA via tonic cannabinoid receptor activation at identified interneuron synapses in rat CA1. Eur. J. Neurosci. *31*, 1196–1207.

Amaral, D.G., and Witter, M.P. (1989). The three-dimensional organization of the hippocampal formation: a review of anatomical data. Neuroscience *31*, 571–591.

Andersen, P., Bliss, T.V., and Skrede, K.K. (1971). Lamellar organization of hippocampal pathways. Exp. Brain Res. *13*, 222–238.

Andersen P, Morris R, Amaral D, Bliss T, O'Keefe J (2007) The Hippocampus Book: Oxford University Press

Aradi, I., Santhakumar, V., Chen, K., and Soltesz, I. (2002). Postsynaptic effects of GABAergic synaptic diversity: regulation of neuronal excitability by changes in IPSC variance. Neuropharmacology *43*, 511–522.

Aradi, I., Santhakumar, V., and Soltesz, I. (2004). Impact of heterogeneous perisomatic IPSC populations on pyramidal cell firing rates. J. Neurophysiol. *91*, 2849–2858.

Armstrong, C., Szabadics, J., Tamás, G., and Soltesz, I. (2011). Neurogliaform cells in the molecular layer of the dentate gyrus as feed-forward γ-aminobutyric acidergic modulators of entorhinal-hippocampal interplay. J. Comp. Neurol. *519*, 1476–1491.

Ascoli, G.A., Brown, K.M., Calixto, E., Card, J.P., Galván, E.J., Perez-Rosello, T., and Barrionuevo, G. (2009). Quantitative morphometry of electrophysiologically identified CA3b interneurons reveals robust local geometry and distinct cell classes. J. Comp. Neurol. *515*, 677–695.

Atluri, P.P., and Regehr, W.G. (1996). Determinants of the time course of facilitation at the granule cell to Purkinje cell synapse. J. Neurosci. Off. J. Soc. Neurosci. *16*, 5661–5671.

Baimbridge, K.G., Peet, M.J., McLennan, H., and Church, J. (1991). Bursting response to current-evoked depolarization in rat CA1 pyramidal neurons is correlated with lucifer yellow dye coupling but not with the presence of calbindin-D28k. Synap. N. Y. N *7*, 269–277.

Bannister, N.J., and Larkman, A.U. (1995a). Dendritic morphology of CA1 pyramidal neurones from the rat hippocampus: I. Branching patterns. J. Comp. Neurol. *360*, 150–160.

Bannister, N.J., and Larkman, A.U. (1995b). Dendritic morphology of CA1 pyramidal neurones from the rat hippocampus: II. Spine distributions. J. Comp. Neurol. *360*, 161–171.

Bartos, M., Vida, I., Frotscher, M., Meyer, A., Monyer, H., Geiger, J.R.P., and Jonas, P. (2002). Fast synaptic inhibition promotes synchronized gamma oscillations in hippocampal interneuron networks. Proc. Natl. Acad. Sci. U. S. A. *99*, 13222–13227.

Bartos, M., Vida, I., and Jonas, P. (2007). Synaptic mechanisms of synchronized gamma oscillations in inhibitory interneuron networks. Nat. Rev. Neurosci. *8*, 45–56.

Berry, S.D., and Thompson, R.F. (1978). Prediction of learning rate from the hippocampal electroencephalogram. Science *200*, 1298–1300.

Bikson, M., Hahn, P.J., Fox, J.E., and Jefferys, J.G.R. (2003). Depolarization block of neurons during maintenance of electrographic seizures. J. Neurophysiol. *90*, 2402–2408.

Blitz, D.M., Foster, K.A., and Regehr, W.G. (2004). Short-term synaptic plasticity: a comparison of two synapses. Nat. Rev. Neurosci. *5*, 630–640.

Bragin, A., Jandó, G., Nádasdy, Z., Hetke, J., Wise, K., and Buzsáki, G. (1995). Gamma (40-100 Hz) oscillation in the hippocampus of the behaving rat. J. Neurosci. Off. J. Soc. Neurosci. *15*, 47–60.

Bragin, A., Engel, J., Wilson, C.L., Fried, I., and Mathern, G.W. (1999a). Hippocampal and entorhinal cortex high-frequency oscillations (100--500 Hz) in human epileptic brain and in kainic acid--treated rats with chronic seizures. Epilepsia *40*, 127–137.

Bragin, A., Engel, J., Wilson, C.L., Vizentin, E., and Mathern, G.W. (1999b). Electrophysiologic analysis of a chronic seizure model after unilateral hippocampal KA injection. Epilepsia *40*, 1210–1221.

Bragin, A., Wilson, C.L., and Engel, J. (2000). Chronic epileptogenesis requires development of a network of pathologically interconnected neuron clusters: a hypothesis. Epilepsia *41 Suppl 6*, S144-152.

Brown, T.H., Fricke, R.A., and Perkel, D.H. (1981). Passive electrical constants in three classes of hippocampal neurons. J. Neurophysiol. *46*, 812–827.

Brunel, N., and Wang, X.-J. (2003). What determines the frequency of fast network oscillations with irregular neural discharges? I. Synaptic dynamics and excitation-inhibition balance. J. Neurophysiol. *90*, 415–430.

Buhl, E.H., Han, Z.S., Lörinczi, Z., Stezhka, V.V., Karnup, S.V., and Somogyi, P. (1994). Physiological properties of anatomically identified axo-axonic cells in the rat hippocampus. J. Neurophysiol. *71*, 1289–1307.

Bullock, T.H., Buzsáki, G., and McClune, M.C. (1990). Coherence of compound field potentials reveals discontinuities in the CA1-subiculum of the hippocampus in freely-moving rats. Neuroscience *38*, 609–619.

Buzsáki, G. (1986). Hippocampal sharp waves: their origin and significance. Brain Res. *398*, 242–252.

Buzsáki, G. (1989). Two-stage model of memory trace formation: a role for "noisy" brain states. Neuroscience *31*, 551–570.

Buzsáki, G. (2002). Theta oscillations in the hippocampus. Neuron *33*, 325–340.

Buzsáki, G. (2015). Hippocampal sharp wave-ripple: A cognitive biomarker for episodic memory and planning. Hippocampus *25*, 1073–1188.

Buzsáki, G., and Draguhn, A. (2004). Neuronal oscillations in cortical networks. Science *304*, 1926–1929.

Buzsàki, G., and Eidelberg, E. (1983). Phase relations of hippocampal projection cells and interneurons to theta activity in the anesthetized rat. Brain Res. *266*, 334–339.

Buzsáki, G., and Moser, E.I. (2013). Memory, navigation and theta rhythm in the hippocampal-entorhinal system. Nat. Neurosci. *16*, 130–138.

Buzsáki, G., Horváth, Z., Urioste, R., Hetke, J., and Wise, K. (1992). High-frequency network oscillation in the hippocampus. Science *256*, 1025–1027.

Calixto, E., Galván, E.J., Card, J.P., and Barrionuevo, G. (2008). Coincidence detection of convergent perforant path and mossy fibre inputs by CA3 interneurons. J. Physiol. *586*, 2695–2712.

Capogna, M. (2011). Neurogliaform cells and other interneurons of stratum lacunosum-moleculare gate entorhinal-hippocampal dialogue. J. Physiol. *589*, 1875–1883.

Cardin, J.A., Carlén, M., Meletis, K., Knoblich, U., Zhang, F., Deisseroth, K., Tsai, L.-H., and Moore, C.I. (2009). Driving fast-spiking cells induces gamma rhythm and controls sensory responses. Nature *459*, 663–667.

Carr, M.F., Jadhav, S.P., and Frank, L.M. (2011). Hippocampal replay in the awake state: a potential substrate for memory consolidation and retrieval. Nat. Neurosci. *14*, 147–153.

Cenquizca, L.A., and Swanson, L.W. (2007). Spatial organization of direct hippocampal field CA1 axonal projections to the rest of the cerebral cortex. Brain Res. Rev. *56*, 1–26.

Chamberland, S., and Topolnik, L. (2012). Inhibitory control of hippocampal inhibitory neurons. Front. Neurosci. *6*, 165.

Chamberland, S., Salesse, C., Topolnik, D., and Topolnik, L. (2010). Synapse-specific inhibitory control of hippocampal feedback inhibitory circuit. Front. Cell. Neurosci. *4*, 130.

Chen, C., Blitz, D.M., and Regehr, W.G. (2002). Contributions of receptor desensitization and saturation to plasticity at the retinogeniculate synapse. Neuron *33*, 779–788.

Cobb, S.R., Buhl, E.H., Halasy, K., Paulsen, O., and Somogyi, P. (1995). Synchronization of neuronal activity in hippocampus by individual GABAergic interneurons. Nature *378*, 75–78.

Cohen, I., Huberfeld, G., and Miles, R. (2006). Emergence of disinhibition-induced synchrony in the CA3 region of the guinea pig hippocampus *in vitro*: Emergence of synchronous hippocampal activity. J. Physiol. *570*, 583–594.

Cole, A.E., and Nicoll, R.A. (1984). The pharmacology of cholinergic excitatory responses in hippocampal pyramidal cells. Brain Res. *305*, 283–290.

Colgin, L.L. (2013). Mechanisms and functions of theta rhythms. Annu. Rev. Neurosci. *36*, 295–312.

Colgin, L.L. (2016). Rhythms of the hippocampal network. Nat. Rev. Neurosci. *17*, 239–249.

Colgin, L.L., and Moser, E.I. (2010). Gamma oscillations in the hippocampus. Physiol. Bethesda Md *25*, 319–329.

Colgin, L.L., Denninger, T., Fyhn, M., Hafting, T., Bonnevie, T., Jensen, O., Moser, M.-B., and Moser, E.I. (2009). Frequency of gamma oscillations routes flow of information in the hippocampus. Nature *462*, 353–357.

Csicsvari, J., and Dupret, D. (2014). Sharp wave/ripple network oscillations and learning-associated hippocampal maps. Philos. Trans. R. Soc. Lond. B. Biol. Sci. *369*, 20120528.

Csicsvari, J., Hirase, H., Czurkó, A., Mamiya, A., and Buzsáki, G. (1999b). Fast network oscillations in the hippocampal CA1 region of the behaving rat. J. Neurosci. Off. J. Soc. Neurosci. *19*, RC20.

Csicsvari, J., Hirase, H., Czurkó, A., Mamiya, A., and Buzsáki, G. (1999a). Oscillatory coupling of hippocampal pyramidal cells and interneurons in the behaving Rat. J. Neurosci. Off. J. Soc. Neurosci. *19*, 274–287.

Csicsvari, J., Hirase, H., Mamiya, A., and Buzsáki, G. (2000). Ensemble patterns of hippocampal CA3-CA1 neurons during sharp wave-associated population events. Neuron *28*, 585–594.

Csicsvari, J., Jamieson, B., Wise, K.D., and Buzsáki, G. (2003). Mechanisms of gamma oscillations in the hippocampus of the behaving rat. Neuron *37*, 311–322.

Daw, M.I., Tricoire, L., Erdelyi, F., Szabo, G., and McBain, C.J. (2009a). Asynchronous transmitter release from cholecystokinin-containing inhibitory interneurons is widespread and target-cell independent. J. Neurosci. Off. J. Soc. Neurosci. *29*, 11112–11122.

DeCoteau, W.E., Thorn, C., Gibson, D.J., Courtemanche, R., Mitra, P., Kubota, Y., and Graybiel, A.M. (2007). Learning-related coordination of striatal and hippocampal theta rhythms during acquisition of a procedural maze task. Proc. Natl. Acad. Sci. U. S. A. *104*, 5644–5649.

Deuchars, J., and Thomson, A.M. (1996). CA1 pyramid-pyramid connections in rat hippocampus in vitro: dual intracellular recordings with biocytin filling. Neuroscience *74*, 1009–1018.

Dittman, J.S., and Regehr, W.G. (1998). Calcium dependence and recovery kinetics of presynaptic depression at the climbing fiber to Purkinje cell synapse. J. Neurosci. Off. J. Soc. Neurosci. *18*, 6147–6162.

Dittman, J.S., Kreitzer, A.C., and Regehr, W.G. (2000). Interplay between facilitation, depression, and residual calcium at three presynaptic terminals. J. Neurosci. Off. J. Soc. Neurosci. *20*, 1374–1385.

Dudek, S.M., Alexander, G.M., and Farris, S. (2016). Rediscovering area CA2: unique properties and functions. Nat. Rev. Neurosci. *17*, 89–102.

Dupret, D., O'Neill, J., Pleydell-Bouverie, B., and Csicsvari, J. (2010). The reorganization and reactivation of hippocampal maps predict spatial memory performance. Nat. Neurosci. *13*, 995–1002.

Ellender, T.J., Nissen, W., Colgin, L.L., Mann, E.O., and Paulsen, O. (2010). Priming of hippocampal population bursts by individual perisomatic-targeting interneurons. J. Neurosci. Off. J. Soc. Neurosci. *30*, 5979–5991.

Emri, Z., Antal, K., Gulyás, A.I., Megías, M., and Freund, T.F. (2001). Electrotonic profile and passive propagation of synaptic potentials in three subpopulations of hippocampal CA1 interneurons. Neuroscience *104*, 1013–1026.

Engel, J., Bragin, A., Staba, R., and Mody, I. (2009). High-frequency oscillations: what is normal and what is not? Epilepsia *50*, 598–604.

Ferraguti, F., Klausberger, T., Cobden, P., Baude, A., Roberts, J.D.B., Szucs, P., Kinoshita, A., Shigemoto, R., Somogyi, P., and Dalezios, Y. (2005). Metabotropic glutamate receptor 8-expressing nerve terminals target subsets of GABAergic neurons in the hippocampus. J. Neurosci. Off. J. Soc. Neurosci. *25*, 10520–10536.

Fioravante, D., and Regehr, W.G. (2011). Short-term forms of presynaptic plasticity. Curr. Opin. Neurobiol. *21*, 269–274.

Florence, G., Dahlem, M.A., Almeida, A.-C.G., Bassani, J.W.M., and Kurths, J. (2009). The role of extracellular potassium dynamics in the different stages of ictal bursting and spreading depression: a computational study. J. Theor. Biol. *258*, 219–228.

Földy, C., Aradi, I., Howard, A., and Soltesz, I. (2004). Diversity beyond variance: modulation of firing rates and network coherence by GABAergic subpopulations. Eur. J. Neurosci. *19*, 119–130.

Földy, C., Neu, A., Jones, M.V., and Soltesz, I. (2006). Presynaptic, activity-dependent modulation of cannabinoid type 1 receptor-mediated inhibition of GABA release. J. Neurosci. Off. J. Soc. Neurosci. *26*, 1465–1469.

Fortune, E.S., and Rose, G.J. (2001). Short-term synaptic plasticity as a temporal filter. Trends Neurosci. *24*, 381–385.

Freund, T.F., and Antal, M. (1988). GABA-containing neurons in the septum control inhibitory interneurons in the hippocampus. Nature *336*, 170–173.

Freund, T.F., and Buzsáki, G. (1996). Interneurons of the hippocampus. Hippocampus *6*, 347–470.

Freund, T.F., and Katona, I. (2007). Perisomatic inhibition. Neuron *56*, 33–42.

Frohlich, F., Bazhenov, M., Iragui-Madoz, V., and Sejnowski, T.J. (2007). Potassium Dynamics in the Epileptic Cortex: New Insights on an Old Topic. The Neuroscientist *14*, 422–433.

Fuentealba, P., Begum, R., Capogna, M., Jinno, S., Márton, L.F., Csicsvari, J., Thomson, A., Somogyi, P., and Klausberger, T. (2008). Ivy cells: a population of nitric-oxide-producing, slow-spiking GABAergic neurons and their involvement in hippocampal network activity. Neuron *57*, 917–929.

Galarreta, M., and Hestrin, S. (1998). Frequency-dependent synaptic depression and the balance of excitation and inhibition in the neocortex. Nat. Neurosci. *1*, 587–594.

Girardeau, G., Benchenane, K., Wiener, S.I., Buzsáki, G., and Zugaro, M.B. (2009). Selective suppression of hippocampal ripples impairs spatial memory. Nat. Neurosci. *12*, 1222–1223.

Givens, B.S., and Olton, D.S. (1990). Cholinergic and GABAergic modulation of medial septal area: effect on working memory. Behav. Neurosci. *104*, 849–855.

Glickfeld, L.L., and Scanziani, M. (2006). Distinct timing in the activity of cannabinoid-sensitive and cannabinoid-insensitive basket cells. Nat. Neurosci. *9*, 807–815.

Gloveli, T., Dugladze, T., Saha, S., Monyer, H., Heinemann, U., Traub, R.D., Whittington, M.A., and Buhl, E.H. (2005). Differential involvement of oriens/pyramidale interneurones in hippocampal network oscillations in vitro. J. Physiol. *562*, 131–147.

Gonzales, R.B., DeLeon Galvan, C.J., Rangel, Y.M., and Claiborne, B.J. (2001). Distribution of thorny excrescences on CA3 pyramidal neurons in the rat hippocampus. J. Comp. Neurol. *430*, 357–368.

Gonzalez-Burgos, G., and Lewis, D.A. (2008). GABA neurons and the mechanisms of network oscillations: implications for understanding cortical dysfunction in schizophrenia. Schizophr. Bull. *34*, 944–961.

Gonzalez-Burgos, G., Fish, K.N., and Lewis, D.A. (2011). GABA neuron alterations, cortical circuit dysfunction and cognitive deficits in schizophrenia. Neural Plast. *2011*, 723184.

Gulyás, A.I., Miles, R., Sík, A., Tóth, K., Tamamaki, N., and Freund, T.F. (1993a). Hippocampal pyramidal cells excite inhibitory neurons through a single release site. Nature *366*, 683–687.

Gulyás, A.I., Miles, R., Hájos, N., and Freund, T.F. (1993b). Precision and variability in postsynaptic target selection of inhibitory cells in the hippocampal CA3 region. Eur. J. Neurosci. *5*, 1729–1751.

Gulyás, A.I., Hájos, N., and Freund, T.F. (1996). Interneurons containing calretinin are specialized to control other interneurons in the rat hippocampus. J. Neurosci. Off. J. Soc. Neurosci. *16*, 3397–3411.

Gulyás, A.I., Megías, M., Emri, Z., and Freund, T.F. (1999). Total number and ratio of excitatory and inhibitory synapses converging onto single interneurons of different types in the CA1 area of the rat hippocampus. J. Neurosci. Off. J. Soc. Neurosci. *19*, 10082–10097.

Gulyás, A.I., Hájos, N., Katona, I., and Freund, T.F. (2003). Interneurons are the local targets of hippocampal inhibitory cells which project to the medial septum. Eur. J. Neurosci. *17*, 1861–1872.

Gulyás, A.I., Szabó, G.G., Ulbert, I., Holderith, N., Monyer, H., Erdélyi, F., Szabó, G., Freund, T.F., and Hájos, N. (2010a). Parvalbumin-containing fast-spiking basket cells generate the field potential oscillations induced by cholinergic receptor activation in the hippocampus. J. Neurosci. Off. J. Soc. Neurosci. *30*, 15134–15145.

Hájos, N., and Mody, I. (1997). Synaptic communication among hippocampal interneurons: properties of spontaneous IPSCs in morphologically identified cells. J. Neurosci. Off. J. Soc. Neurosci. *17*, 8427–8442.

Hájos, N., and Paulsen, O. (2009). Network mechanisms of gamma oscillations in the CA3 region of the hippocampus. Neural Netw. Off. J. Int. Neural Netw. Soc. *22*, 1113–1119.

Hájos, N., Pálhalmi, J., Mann, E.O., Németh, B., Paulsen, O., and Freund, T.F. (2004). Spike timing of distinct types of GABAergic interneuron during hippocampal gamma oscillations in vitro. J. Neurosci. Off. J. Soc. Neurosci. *24*, 9127–9137.

Hájos, N., Ellender, T.J., Zemankovics, R., Mann, E.O., Exley, R., Cragg, S.J., Freund, T.F., and Paulsen, O. (2009). Maintaining network activity in submerged hippocampal slices: importance of oxygen supply. Eur. J. Neurosci. *29*, 319–327.

Hájos, N., Karlócai, M.R., Németh, B., Ulbert, I., Monyer, H., Szabó, G., Erdélyi, F., Freund, T.F., and Gulyás, A.I. (2013). Input-output features of anatomically identified CA3 neurons during hippocampal sharp wave/ripple oscillation in vitro. J. Neurosci. Off. J. Soc. Neurosci. *33*, 11677–11691.

Hangya, B., Borhegyi, Z., Szilágyi, N., Freund, T.F., and Varga, V. (2009). GABAergic neurons of the medial septum lead the hippocampal network during theta activity. J. Neurosci. Off. J. Soc. Neurosci. *29*, 8094–8102.

Hasselmo, M.E., Wyble, B.P., and Wallenstein, G.V. (1996). Encoding and retrieval of episodic memories: role of cholinergic and GABAergic modulation in the hippocampus. Hippocampus *6*, 693–708.

Hefft, S., and Jonas, P. (2005). Asynchronous GABA release generates long-lasting inhibition at a hippocampal interneuron-principal neuron synapse. Nat. Neurosci. *8*, 1319–1328.

Hennig, M.H. (2013). Theoretical models of synaptic short term plasticity. Front. Comput. Neurosci. *7*, 45.

Hitti, F.L., and Siegelbaum, S.A. (2014). The hippocampal CA2 region is essential for social memory. Nature *508*, 88–92.

Ishizuka, N., Weber, J., and Amaral, D.G. (1990). Organization of intrahippocampal projections originating from CA3 pyramidal cells in the rat. J. Comp. Neurol. *295*, 580–623.

Ishizuka, N., Cowan, W.M., and Amaral, D.G. (1995). A quantitative analysis of the dendritic organization of pyramidal cells in the rat hippocampus. J. Comp. Neurol. *362*, 17–45.

Jackman, S.L., Turecek, J., Belinsky, J.E., and Regehr, W.G. (2016). The calcium sensor synaptotagmin 7 is required for synaptic facilitation. Nature *529*, 88–91.

Jadhav, S.P., Kemere, C., German, P.W., and Frank, L.M. (2012). Awake hippocampal sharp-wave ripples support spatial memory. Science *336*, 1454–1458.

Jefferys, J.G.R., Menendez de la Prida, L., Wendling, F., Bragin, A., Avoli, M., Timofeev, I., and Lopes da Silva, F.H. (2012). Mechanisms of physiological and epileptic HFO generation. Prog. Neurobiol. *98*, 250–264.

Jinno, S., Klausberger, T., Marton, L.F., Dalezios, Y., Roberts, J.D.B., Fuentealba, P., Bushong, E.A., Henze, D., Buzsáki, G., and Somogyi, P. (2007). Neuronal diversity in GABAergic long-range projections from the hippocampus. J. Neurosci. Off. J. Soc. Neurosci. *27*, 8790–8804.

Jirsch, J.D., Urrestarazu, E., LeVan, P., Olivier, A., Dubeau, F., and Gotman, J. (2006). High-frequency oscillations during human focal seizures. Brain J. Neurol. *129*, 1593–1608.

Jonas, P., Bischofberger, J., Fricker, D., and Miles, R. (2004). Interneuron Diversity series: Fast in, fast out--temporal and spatial signal processing in hippocampal interneurons. Trends Neurosci. *27*, 30–40.

Jones, M.V., and Westbrook, G.L. (1996). The impact of receptor desensitization on fast synaptic transmission. Trends Neurosci. *19*, 96–101.

Jouvet, M. (1969). Biogenic amines and the states of sleep. Science *163*, 32–41.

Kahana, M.J., Seelig, D., and Madsen, J.R. (2001). Theta returns. Curr. Opin. Neurobiol. *11*, 739–744.

Kamondi, A., Acsády, L., Wang, X.J., and Buzsáki, G. (1998). Theta oscillations in somata and dendrites of hippocampal pyramidal cells in vivo: activity-dependent phase-precession of action potentials. Hippocampus *8*, 244–261.

Kandaswamy, U., Deng, P.-Y., Stevens, C.F., and Klyachko, V.A. (2010). The role of presynaptic dynamics in processing of natural spike trains in hippocampal synapses. J. Neurosci. Off. J. Soc. Neurosci. *30*, 15904–15914.

Karson, M.A., Tang, A.-H., Milner, T.A., and Alger, B.E. (2009). Synaptic cross talk between perisomatic-targeting interneuron classes expressing cholecystokinin and parvalbumin in hippocampus. J. Neurosci. Off. J. Soc. Neurosci. *29*, 4140–4154.

Katona, I., Sperlágh, B., Sík, A., Käfalvi, A., Vizi, E.S., Mackie, K., and Freund, T.F. (1999). Presynaptically located CB1 cannabinoid receptors regulate GABA release from axon terminals of specific hippocampal interneurons. J. Neurosci. Off. J. Soc. Neurosci. *19*, 4544–4558.

Katz, B., and Miledi, R. (1968). The role of calcium in neuromuscular facilitation. J. Physiol. *195*, 481–492.

Khosravani, H., Mehrotra, N., Rigby, M., Hader, W.J., Pinnegar, C.R., Pillay, N., Wiebe, S., and Federico, P. (2009). Spatial localization and time-dependant changes of electrographic high frequency oscillations in human temporal lobe epilepsy. Epilepsia *50*, 605–616.

Klausberger, T. (2009). GABAergic interneurons targeting dendrites of pyramidal cells in the CA1 area of the hippocampus. Eur. J. Neurosci. *30*, 947–957.

Klausberger, T., and Somogyi, P. (2008). Neuronal diversity and temporal dynamics: the unity of hippocampal circuit operations. Science *321*, 53–57.

Klausberger, T., Marton, L.F., O'Neill, J., Huck, J.H.J., Dalezios, Y., Fuentealba, P., Suen, W.Y., Papp, E., Kaneko, T., Watanabe, M., et al. (2005). Complementary roles of

cholecystokinin- and parvalbumin-expressing GABAergic neurons in hippocampal network oscillations. J. Neurosci. Off. J. Soc. Neurosci. *25*, 9782–9793.

Klyachko, V.A., and Stevens, C.F. (2006). Excitatory and feed-forward inhibitory hippocampal synapses work synergistically as an adaptive filter of natural spike trains. PLoS Biol. *4*, e207.

Kocsis, B., and Vertes, R.P. (1997). Phase relations of rhythmic neuronal firing in the supramammillary nucleus and mammillary body to the hippocampal theta activity in urethane anesthetized rats. Hippocampus *7*, 204–214.

Kohara, K., Pignatelli, M., Rivest, A.J., Jung, H.-Y., Kitamura, T., Suh, J., Frank, D., Kajikawa, K., Mise, N., Obata, Y., et al. (2014). Cell type-specific genetic and optogenetic tools reveal hippocampal CA2 circuits. Nat. Neurosci. *17*, 269–279.

Kraushaar, U., and Jonas, P. (2000). Efficacy and stability of quantal GABA release at a hippocampal interneuron-principal neuron synapse. J. Neurosci. Off. J. Soc. Neurosci. *20*, 5594–5607.

Lasztóczi, B., and Klausberger, T. (2014). Layer-specific GABAergic control of distinct gamma oscillations in the CA1 hippocampus. Neuron *81*, 1126–1139.

Lasztóczi, B., Tukker, J.J., Somogyi, P., and Klausberger, T. (2011). Terminal field and firing selectivity of cholecystokinin-expressing interneurons in the hippocampal CA3 area. J. Neurosci. Off. J. Soc. Neurosci. *31*, 18073–18093.

Lee, C.-C.J., Anton, M., Poon, C.-S., and McRae, G.J. (2009). A kinetic model unifying presynaptic short-term facilitation and depression. J. Comput. Neurosci. *26*, 459–473.

Lee, S.-H., Marchionni, I., Bezaire, M., Varga, C., Danielson, N., Lovett-Barron, M., Losonczy, A., and Soltesz, I. (2014). Parvalbumin-positive basket cells differentiate among hippocampal pyramidal cells. Neuron *82*, 1129–1144.

Lenkey, N., Kirizs, T., Holderith, N., Máté, Z., Szabó, G., Vizi, E.S., Hájos, N., and Nusser, Z. (2015). Tonic endocannabinoid-mediated modulation of GABA release is independent of the CB1 content of axon terminals. Nat. Commun. *6*, 6557.

Li, X.G., Somogyi, P., Ylinen, A., and Buzsáki, G. (1994). The hippocampal CA3 network: an in vivo intracellular labeling study. J. Comp. Neurol. *339*, 181–208.

Losonczy, A., Zhang, L., Shigemoto, R., Somogyi, P., and Nusser, Z. (2002). Cell type dependence and variability in the short-term plasticity of EPSCs in identified mouse hippocampal interneurones. J. Physiol. *542*, 193–210.

Losonczy, A., Biró, A.A., and Nusser, Z. (2004). Persistently active cannabinoid receptors mute a subpopulation of hippocampal interneurons. Proc. Natl. Acad. Sci. U. S. A. *101*, 1362–1367.

Mann, E.O., Suckling, J.M., Hajos, N., Greenfield, S.A., and Paulsen, O. (2005). Perisomatic feedback inhibition underlies cholinergically induced fast network oscillations in the rat hippocampus in vitro. Neuron *45*, 105–117.

Markowska, A.L., Olton, D.S., Murray, E.A., and Gaffan, D. (1989). A comparative analysis of the role of fornix and cingulate cortex in memory: rats. Exp. Brain Res. *74*, 187–201.

Markram, H., Pikus, D., Gupta, A., and Tsodyks, M. (1998). Potential for multiple mechanisms, phenomena and algorithms for synaptic plasticity at single synapses. Neuropharmacology *37*, 489–500.

Máté, Z., Poles, M.Z., Szabó, G., Bagyánszki, M., Talapka, P., Fekete, E., and Bódi, N. (2013a). Spatiotemporal expression pattern of DsRedT3/CCK gene construct during postnatal development of myenteric plexus in transgenic mice. Cell Tissue Res. *352*, 199–206.

Mátyás, F., Freund, T.F., and Gulyás, A.I. (2004a). Convergence of excitatory and inhibitory inputs onto CCK-containing basket cells in the CA1 area of the rat hippocampus. Eur. J. Neurosci. *19*, 1243–1256.

Mátyás, F., Freund, T.F., and Gulyás, A.I. (2004b). Immunocytochemically defined interneuron populations in the hippocampus of mouse strains used in transgenic technology. Hippocampus *14*, 460–481.

Megías, M., Emri, Z., Freund, T.F., and Gulyás, A.I. (2001). Total number and distribution of inhibitory and excitatory synapses on hippocampal CA1 pyramidal cells. Neuroscience *102*, 527–540.

Menendez de la Prida, L., Staba, R.J., and Dian, J.A. (2015). Conundrums of high-frequency oscillations (80-800 Hz) in the epileptic brain. J. Clin. Neurophysiol. Off. Publ. Am. Electroencephalogr. Soc. *32*, 207–219.

Mercer, A., Trigg, H.L., and Thomson, A.M. (2007). Characterization of neurons in the CA2 subfield of the adult rat hippocampus. J. Neurosci. Off. J. Soc. Neurosci. *27*, 7329–7338.

Meyer, A.H., Katona, I., Blatow, M., Rozov, A., and Monyer, H. (2002a). In vivo labeling of parvalbumin-positive interneurons and analysis of electrical coupling in identified neurons. J. Neurosci. Off. J. Soc. Neurosci. *22*, 7055–7064.

M'Harzi, M., Palacios, A., Monmaur, P., Willig, F., Houcine, O., and Delacour, J. (1987). Effects of selective lesions of fimbria-fornix on learning set in the rat. Physiol. Behav. *40*, 181–188.

Miles, R. (1990). Synaptic excitation of inhibitory cells by single CA3 hippocampal pyramidal cells of the guinea-pig in vitro. J. Physiol. *428*, 61–77.

Miles, R., Tóth, K., Gulyás, A.I., Hájos, N., and Freund, T.F. (1996a). Differences between somatic and dendritic inhibition in the hippocampus. Neuron *16*, 815–823.

Moser, E.I., Roudi, Y., Witter, M.P., Kentros, C., Bonhoeffer, T., and Moser, M.-B. (2014). Grid cells and cortical representation. Nat. Rev. Neurosci. *15*, 466–481.

Nádasdy, Z., Hirase, H., Czurkó, A., Csicsvari, J., and Buzsáki, G. (1999). Replay and time compression of recurring spike sequences in the hippocampus. J. Neurosci. Off. J. Soc. Neurosci. *19*, 9497–9507.

Nörenberg, A., Hu, H., Vida, I., Bartos, M., and Jonas, P. (2010). Distinct nonuniform cable properties optimize rapid and efficient activation of fast-spiking GABAergic interneurons. Proc. Natl. Acad. Sci. U. S. A. *107*, 894–899.

Nyíri, G., Freund, T.F., and Somogyi, P. (2001). Input-dependent synaptic targeting of alpha(2)-subunit-containing GABA(A) receptors in synapses of hippocampal pyramidal cells of the rat. Eur. J. Neurosci. *13*, 428–442.

O'Keefe, J., and Recce, M.L. (1993). Phase relationship between hippocampal place units and the EEG theta rhythm. Hippocampus *3*, 317–330.

Oliva, A., Fernández-Ruiz, A., Buzsáki, G., and Berényi, A. (2016). Role of Hippocampal CA2 Region in Triggering Sharp-Wave Ripples. Neuron *91*, 1342–1355.

O'Neill, J., Senior, T., and Csicsvari, J. (2006). Place-selective firing of CA1 pyramidal cells during sharp wave/ripple network patterns in exploratory behavior. Neuron *49*, 143–155.

O'Neill, J., Pleydell-Bouverie, B., Dupret, D., and Csicsvari, J. (2010). Play it again: reactivation of waking experience and memory. Trends Neurosci. *33*, 220–229.

Papp, O.I., Karlócai, M.R., Tóth, I.E., Freund, T.F., and Hájos, N. (2013). Different input and output properties characterize parvalbumin-positive basket and Axo-axonic cells in the hippocampal CA3 subfield. Hippocampus *23*, 903–918.

Paré, D., Collins, D.R., and Pelletier, J.G. (2002). Amygdala oscillations and the consolidation of emotional memories. Trends Cogn. Sci. *6*, 306–314.

Pawelzik, H., Hughes, D.I., and Thomson, A.M. (2002). Physiological and morphological diversity of immunocytochemically defined parvalbumin- and cholecystokinin-positive interneurones in CA1 of the adult rat hippocampus. J. Comp. Neurol. *443*, 346–367.

Penttonen, M., Kamondi, A., Acsády, L., and Buzsáki, G. (1998). Gamma frequency oscillation in the hippocampus of the rat: intracellular analysis in vivo. Eur. J. Neurosci. *10*, 718–728.

Perreault, P., and Avoli, M. (1991). Physiology and pharmacology of epileptiform activity induced by 4-aminopyridine in rat hippocampal slices. J. Neurophysiol. *65*, 771–785.

Pfeffer, C.K., Xue, M., He, M., Huang, Z.J., and Scanziani, M. (2013). Inhibition of inhibition in visual cortex: the logic of connections between molecularly distinct interneurons. Nat. Neurosci. *16*, 1068–1076.

Price, C.J., Cauli, B., Kovacs, E.R., Kulik, A., Lambolez, B., Shigemoto, R., and Capogna, M. (2005). Neurogliaform neurons form a novel inhibitory network in the hippocampal CA1 area. J. Neurosci. Off. J. Soc. Neurosci. *25*, 6775–6786.

Raisman, G., Cowan, W.M., and Powell, T.P. (1966). An experimental analysis of the efferent projection of the hippocampus. Brain J. Neurol. *89*, 83–108.

Rancz, E.A., and Häusser, M. (2010). Dendritic spikes mediate negative synaptic gain control in cerebellar Purkinje cells. Proc. Natl. Acad. Sci. U. S. A. *107*, 22284–22289.

Rawlins, J.N., Feldon, J., and Gray, J.A. (1979). Septo-hippocampal connections and the hippocampal theta rhythm. Exp. Brain Res. *37*, 49–63.

Regehr, W.G. (2012). Short-term presynaptic plasticity. Cold Spring Harb. Perspect. Biol. *4*, a005702.

Reig, R., and Sanchez-Vives, M.V. (2007). Synaptic transmission and plasticity in an active cortical network. PloS One *2*, e670.

Reyes, A., Lujan, R., Rozov, A., Burnashev, N., Somogyi, P., and Sakmann, B. (1998). Target-cell-specific facilitation and depression in neocortical circuits. Nat. Neurosci. *1*, 279–285.

Savanthrapadian, S., Meyer, T., Elgueta, C., Booker, S.A., Vida, I., and Bartos, M. (2014). Synaptic properties of SOM- and CCK-expressing cells in dentate gyrus interneuron networks. J. Neurosci. Off. J. Soc. Neurosci. *34*, 8197–8209.

Schlingloff, D., Káli, S., Freund, T.F., Hájos, N., and Gulyás, A.I. (2014). Mechanisms of sharp wave initiation and ripple generation. J. Neurosci. Off. J. Soc. Neurosci. *34*, 11385–11398.

Schnitzler, A., and Gross, J. (2005). Normal and pathological oscillatory communication in the brain. Nat. Rev. Neurosci. *6*, 285–296.

Schomburg, E.W., Anastassiou, C.A., Buzsáki, G., and Koch, C. (2012). The spiking component of oscillatory extracellular potentials in the rat hippocampus. J. Neurosci. Off. J. Soc. Neurosci. *32*, 11798–11811.

Sik, A., Tamamaki, N., and Freund, T.F. (1993). Complete axon arborization of a single CA3 pyramidal cell in the rat hippocampus, and its relationship with postsynaptic parvalbumin-containing interneurons. Eur. J. Neurosci. *5*, 1719–1728.

Singer, W. (1999). Neuronal synchrony: a versatile code for the definition of relations? Neuron *24*, 49–65, 111–125.

Slomianka, L., Amrein, I., Knuesel, I., Sørensen, J.C., and Wolfer, D.P. (2011). Hippocampal pyramidal cells: the reemergence of cortical lamination. Brain Struct. Funct. *216*, 301–317.

Somogyi, P., and Klausberger, T. (2005). Defined types of cortical interneurone structure space and spike timing in the hippocampus. J. Physiol. *562*, 9–26.

Spampanato, J., and Mody, I. (2007). Spike timing of lacunosom-moleculare targeting interneurons and CA3 pyramidal cells during high-frequency network oscillations in vitro. J. Neurophysiol. *98*, 96–104.

Spruston, N. (2008). Pyramidal neurons: dendritic structure and synaptic integration. Nat. Rev. Neurosci. *9*, 206–221.

Stark, E., Roux, L., Eichler, R., Senzai, Y., Royer, S., and Buzsáki, G. (2014). Pyramidal cell-interneuron interactions underlie hippocampal ripple oscillations. Neuron *83*, 467–480.

van Strien, N.M., Cappaert, N.L.M., and Witter, M.P. (2009). The anatomy of memory: an interactive overview of the parahippocampal-hippocampal network. Nat. Rev. Neurosci. *10*, 272–282.

Sullivan, D., Csicsvari, J., Mizuseki, K., Montgomery, S., Diba, K., and Buzsáki, G. (2011). Relationships between hippocampal sharp waves, ripples, and fast gamma oscillation: influence of dentate and entorhinal cortical activity. J. Neurosci. Off. J. Soc. Neurosci. *31*, 8605–8616.

Sun, J.-Y., Wu, X.-S., and Wu, L.-G. (2002). Single and multiple vesicle fusion induce different rates of endocytosis at a central synapse. Nature *417*, 555–559.

Szabó, G.G., Holderith, N., Gulyás, A.I., Freund, T.F., and Hájos, N. (2010a). Distinct synaptic properties of perisomatic inhibitory cell types and their different modulation by cholinergic receptor activation in the CA3 region of the mouse hippocampus. Eur. J. Neurosci. *31*, 2234–2246.

Szabó, G.G., Papp, O.I., Máté, Z., Szabó, G., and Hájos, N. (2014). Anatomically heterogeneous populations of CB1 cannabinoid receptor-expressing interneurons in the CA3 region of the hippocampus show homogeneous input-output characteristics. Hippocampus *24*, 1506–1523.

Takács, V.T., Freund, T.F., and Gulyás, A.I. (2008). Types and synaptic connections of hippocampal inhibitory neurons reciprocally connected with the medial septum. Eur. J. Neurosci. *28*, 148–164.

Takács, V.T., Szőnyi, A., Freund, T.F., Nyiri, G., and Gulyás, A.I. (2014). Quantitative ultrastructural analysis of basket and axo-axonic cell terminals in the mouse hippocampus. Brain Struct. Funct.

Tamamaki, N., Abe, K., and Nojyo, Y. (1988). Three-dimensional analysis of the whole axonal arbors originating from single CA2 pyramidal neurons in the rat hippocampus with the aid of a computer graphic technique. Brain Res. *452*, 255–272.

Thomson, A.M., Bannister, A.P., Hughes, D.I., and Pawelzik, H. (2000). Differential sensitivity to Zolpidem of IPSPs activated by morphologically identified CA1 interneurons in slices of rat hippocampus. Eur. J. Neurosci. *12*, 425–436.

Tóth, K., Borhegyi, Z., and Freund, T.F. (1993). Postsynaptic targets of GABAergic hippocampal neurons in the medial septum-diagonal band of broca complex. J. Neurosci. Off. J. Soc. Neurosci. *13*, 3712–3724.

Traub, R.D., and Wong, R.K. (1982). Cellular mechanism of neuronal synchronization in epilepsy. Science *216*, 745–747.

Trevelyan, A.J., Sussillo, D., Watson, B.O., and Yuste, R. (2006). Modular propagation of epileptiform activity: evidence for an inhibitory veto in neocortex. J. Neurosci. Off. J. Soc. Neurosci. *26*, 12447–12455.

Tsodyks, M., Pawelzik, K., and Markram, H. (1998). Neural networks with dynamic synapses. Neural Comput. *10*, 821–835.

Tyan, L., Chamberland, S., Magnin, E., Camiré, O., Francavilla, R., David, L.S., Deisseroth, K., and Topolnik, L. (2014). Dendritic inhibition provided by interneuron-specific cells controls the firing rate and timing of the hippocampal feedback inhibitory circuitry. J. Neurosci. Off. J. Soc. Neurosci. *34*, 4534–4547.

Ulbert, I., Halgren, E., Heit, G., and Karmos, G. (2001). Multiple microelectrode-recording system for human intracortical applications. J. Neurosci. Methods *106*, 69–79.

Ulbert, I., Heit, G., Madsen, J., Karmos, G., and Halgren, E. (2004). Laminar analysis of human neocortical interictal spike generation and propagation: current source density and multiunit analysis in vivo. Epilepsia *45 Suppl 4*, 48–56.

Valero, M., Cid, E., Averkin, R.G., Aguilar, J., Sanchez-Aguilera, A., Viney, T.J., Gomez-Dominguez, D., Bellistri, E., and de la Prida, L.M. (2015). Determinants of different deep and superficial CA1 pyramidal cell dynamics during sharp-wave ripples. Nat. Neurosci. *18*, 1281–1290.

Vida, I., and Frotscher, M. (2000). A hippocampal interneuron associated with the mossy fiber system. Proc. Natl. Acad. Sci. U. S. A. *97*, 1275–1280.

Vida, I., Halasy, K., Szinyei, C., Somogyi, P., and Buhl, E.H. (1998). Unitary IPSPs evoked by interneurons at the stratum radiatum-stratum lacunosum-moleculare border in the CA1 area of the rat hippocampus in vitro. J. Physiol. *506 (Pt 3)*, 755–773.

Viney, T.J., Lasztoczi, B., Katona, L., Crump, M.G., Tukker, J.J., Klausberger, T., and Somogyi, P. (2013). Network state-dependent inhibition of identified hippocampal CA3 axo-axonic cells in vivo. Nat. Neurosci. *16*, 1802–1811.

Vinogradova, O.S., Brazhnik, E.S., Stafekhina, V.S., and Kichigina, V.F. (1995). Modulation of septal influences on hippocampal neurons by cholinergic substances. Neurosci. Behav. Physiol. *25*, 453–461.

Wang, L.Y., and Kaczmarek, L.K. (1998). High-frequency firing helps replenish the readily releasable pool of synaptic vesicles. Nature *394*, 384–388.

Whittington, M.A., Traub, R.D., and Jefferys, J.G. (1995). Erosion of inhibition contributes to the progression of low magnesium bursts in rat hippocampal slices. J. Physiol. *486 (Pt 3)*, 723–734.

Wilson, M.A., and McNaughton, B.L. (1994). Reactivation of hippocampal ensemble memories during sleep. Science *265*, 676–679.

Winson, J. (1978). Loss of hippocampal theta rhythm results in spatial memory deficit in the rat. Science *201*, 160–163.

Wu, C., Asl, M.N., Gillis, J., Skinner, F.K., and Zhang, L. (2005). An in vitro model of hippocampal sharp waves: regional initiation and intracellular correlates. J. Neurophysiol. *94*, 741–753.

Ylinen, A., Soltész, I., Bragin, A., Penttonen, M., Sik, A., and Buzsáki, G. (1995). Intracellular correlates of hippocampal theta rhythm in identified pyramidal cells, granule cells, and basket cells. Hippocampus *5*, 78–90.

Ziburkus, J., Cressman, J.R., Barreto, E., and Schiff, S.J. (2006). Interneuron and pyramidal cell interplay during in vitro seizure-like events. J. Neurophysiol. *95*, 3948–3954.

Zucker, R.S., and Regehr, W.G. (2002). Short-term synaptic plasticity. Annu. Rev. Physiol. *64*, 355–405.

DOI:10.14753/SE.2018.2077

XII. LIST OF PUBLICATIONS

Publications related to the dissertation

Kohus Z, Káli S, Rovira-Esteban L, Schlingloff D, Papp O, Freund TF, Hájos N, Gulyás AI. 2016. Properties and dynamics of inhibitory synaptic communication within the CA3 microcircuits of pyramidal cells and interneurons expressing parvalbumin or cholecystokinin. Journal of Physiology 597(13): 3745-74

Karlócai MR, **Kohus Z**, Káli S, Ulbert I, Szabó G, Máté Z, Freund TF, Gulyás AI. 2014. Physiological sharp wave-ripples and interictal events in vitro: what's the difference? Brain. 137(Pt 2): 463-85

DOI:10.14753/SE.2018.2077

XIII. ACKNOWLEDGEMENTS

I would like to thank many people who directly or indirectly contributed to this thesis and underlying experiments. First, I express my special thanks to my advisor Dr. Attila I Gulyás, for the guidance, encouragement and advices throughout the time I spent as a research assistant and subsequently as a PhD student.

I would like to thank to Prof. Tamás Freund for the possibility to work and study in the Institute of Experimental Medicine, Hungarian Academy of Sciences.

I am grateful to Dr. Noémi Holderith who spent her time to read the thesis and provided advices to improve the quality of my artwork.

I owe my deepest gratitude to Dr. Norbert Hájos who gave me the possibility to conduct first electrophysiologial experiments, and for his encouragement and inspiring conversations.

I would also like to thank to Dr. Szabolcs Káli, who performed the computational modeling and clustering analysis part presented in this thesis.

I wish to express my gratitude to Dr. Rita Karlócai, Dániel Schlingloff and Nándor Kricky for performing experiments, help and for all the joyful moments we shared in the lab.

I am grateful to all former and present members of the Laboratory of Cerebral Cortex Research and 'Lendület' Laboratory of Network Neurophysiology.

Finally, I would like to express my deepest gratitude to my family, especially my wife, Kohus-Nagy Viktória in supporting me. Without their help, this thesis would not exist at all.